Efficient adaptive equalization for PMD mitigation in next-generation optical access networks

Peter Nwakamma

INSTITUT POLYTECHNIQUE DE PARIS

NNT : 2024IPPAT042

Thèse de doctorat

Efficient adaptive equalization for PMD mitigation in next-generation optical access networks

Thèse de doctorat de l'Institut Polytechnique de Paris
préparée à Télécom Paris

École doctorale n°626 École doctorale de l'Institut Polytechnique de Paris (ED IP Paris)
Spécialité de doctorat : Réseaux, Informations et Communications

Thèse présentée et soutenue à Palaiseau, le 27 Novembre 2024, par

PETER AKACHI NWAKAMMA

Composition du Jury :

Ghaya REKAYA Professeure, Télécom Paris, Palaiseau (LTCI)	Présidente/Examinatrice
Mourad MENIF Professeur, SupCom, Tunis (GRESCOM)	Rapporteur
Vahid MEGHDADI Professeur, Université de Limoges, Limoges (XLIM)	Rapporteur
Stéphane AZOU Professeur, ENIB, Brest (Lab-STICC)	Examinateur
Cédric WARE Professeur, Télécom Paris, Palaiseau (LTCI)	Directeur de thèse
Yves JAOUËN Professeur, Télécom Paris, Palaiseau (LTCI)	Co-directeur de thèse
Gwillerm FROC Senior Researcher, Mistubishi Electric, Rennes (INS)	Invité/ Co-encadrant

To All who consistently show up, no matter what.

Acknowledgements

It would not have been possible to complete this thesis without the support and contributions from a number of people.

I would like to thank my thesis supervisors — Cédric, Yves, and Gwillerm — for their joint and individual roles in consistently providing me with guidance, resources, and feedback which helped me develop new skills and become more comfortable with exploring uncharted territories. I also thank the members of the jury for thoroughly reviewing my manuscript and for the insightful discussions.

I am grateful for the CIFRE industrial grant, between Mitsubishi Electric Research & Development Centre Europe (MERCE) and Télécom Paris (Institut Polytechnique de Paris), that permitted this thesis. It presented me the opportunity to have both industrial and academic research experience.

At MERCE I had the opportunity to work closely with Gwillerm, my industrial supervisor, David my research manager, and Loïc the head of division. I also had the opportunity to interact and have fruitful discussions with Denis, Benoit, Florian, Eric, Christophe, Ryo, Romain, François, Kaëlig, Magali, Marie, Sophie, Beatrice, Edem, Nicolas, Cristina, Adel, Laurent, Augustin, Yaya, Axel, and Thomas. These discussions helped me with different aspects of my work, answering some questions that I had, and with adapting and integrating into the company.

At Télécom Paris my colleagues Julien, Abdelaziz, Ibrahim, Raziyeh, Hyunah, Thomas C., Virajit, Isaia, Joana, Perrine, Zülâl, Jamal, Akram A., Sara, Louis, Aymen, Pierre, Guillaume, Yue, Yi, Xiaoyan, Xiaolin, Di, Raphaël, Mohanad, Jingtian, Shiyuan, Thibaut, Shihao, Natasha, Thomas P., Sylvain N., Mustapha, Mehrasa, Nilesh, Francesco, Albert, Ghiles, Mehdi, and Olivier S. were there to discuss a wide variety of interesting topics — both work and non-work related —, to help with troubleshooting experiments in the lab, to have lunch, and some calm and relaxing evenings together. Hamidou, Yvonne, Florence L., Marine, Florence B., Julia, and Vincent greatly and promptly assisted me with administrative issues and information system issues.

I am also grateful to the following faculty members — Ghaya, Michel M., Philippe, Elie, Heming, Mansoor, Frédéric, Chadi, Antoine, Karim, Tarik, Reda, Peter B., Michèle, Mireille, Robert, and Aslan for their support and timely assistance whenever I needed it.

I am profoundly grateful for gift of dear friends — Uche (FUN), Valentine, Regina, Patrick, Ikhtiyor, Ibraheem, Ghazal, Abdel, Elvis, Phoebe, Léa, Nihal, Raquel, Hanane, Khaoula, Aïssa, Taofik, Amine, Kamel, Akuorkor, Ana, ... There are no limits to your consistent emotional support and encouragement. I also thank Sylvain A., Alix, Juliana, Alexis, Nelson, Killian, Christian, Sterenn, Aymeric, Hamza, and Augustine for their professional and friendly support.

Finally I would like to appreciate my family — Nwakamma, Magdalene, twin brother Paul, Honeybelle, Maryann, Okechukwu, and Emeka for always being there for me in more ways than can be described — and God almighty for the gift of life without which none

of this would have been possible.

Abstract

Optical fiber cables are the backbone facilitating more than 95 percent of worldwide telecommunications. The deployment of these fiber cables could either be under the oceans (submarine cables) for transatlantic communications or on land (terrestrial cables), and they permit high-speed data transmission leading to ubiquitous communication irrespective of the distance between the communicating entities. As the world transitions fully into the fourth industrial revolution (Industry 4.0), the demand for connectivity will continue to increase exponentially with billions of people and machines connected in unprecedented ways as technology becomes deeply rooted within societies. This increase in demand will originate mostly from users located in a segment of the terrestrial networks known as the optical access network (OAN). The OAN must therefore adapt to accommodate these demands in a flexible and cost-effective way since the connections in the OAN are proportional to the number of users. Passive optical networks (PONs) are currently the most deployed OAN because of their cost-effectiveness thanks to the passive splitting network architecture and use of intensity modulation and direct detection (IM-DD) technology that requires relatively cheap optics. Several evolutions of the IM-DD PON have been standardized with the goal of flexibly meeting the single channel capacity requirements of up to 10 Gigabits/second (Gbps or G)-, 25G-, and recently 50G-PON. However, this increase in capacity comes with a tradeoff – sacrificing cost-effectiveness and performance since the IM-DD PON would need to employ expensive digital signal processing (DSP) for channel equalization and also face the IM-DD-inherent line rate limitation respectively – such that coherent detection (CohD) is being considered for PON (CPON). CohD is the technology used in the core networks. It is costlier than IM-DD and utilizes continuous DSP. Scaling up IM-DD PON to support single channel capacities of 100G and beyond brings it closer in cost to CohD, which motivates the counter strategy of scaling down the cost of a potential CPON that will easily permit 100G and beyond. The future OAN will therefore be DSP-enabled. However, considering the asymmetrical architecture of the PON that requires burst-mode operation, the DSP operations must also be burst-mode compatible to meet the service requirements in CPON. This translates to a strict requirement on the latency. Also considering that the polarization mode dispersion (PMD) impairment, in the case of ageing and aerial fibers in OAN, can be high and that the DSP equalization algorithms can be impacted by it, careful analysis of the convergence properties of equalization DSP is necessary. In this thesis, we address the issue of latency from the DSP point of view focusing on the adaptive equalization. Firstly, we propose an adaptive equalizer that can overcome the limitations induced by the potentially wide PMD environmental conditions of the OAN. Secondly, we enhance the proposed adaptive equalizer to self-reconfigure depending on the PMD level sensed. Finally, in the context of overall DSP complexity reduction, we investigate the potential of the proposed algorithm to mitigate chromatic dispersion (CD) thereby reducing the requirement on a separate CD equalization DSP block. The proposed algorithm achieves convergence speed, in all cases,

well under the expected latency threshold for 50G-PON and beyond.

Résumé

Les câbles à fibre optique constituent l'épine dorsale de plus de 95 % des télécommunications mondiales. Le déploiement de ces câbles à fibre optique peut se faire soit sous les océans (câbles sous-marins) pour les communications transatlantiques, soit sur terre (câbles terrestres), et ils permettent une transmission de données à haut débit conduisant à une communication omniprésente quelle que soit la distance entre les entités communicantes. Alors que le monde entre pleinement dans la quatrième révolution industrielle (Industrie 4.0), la demande de connectivité va continuer à augmenter de manière exponentielle avec des milliards de personnes et de machines connectées de manière inédite à mesure que la technologie s'enracine profondément dans les sociétés. Cette augmentation de la demande proviendra principalement des utilisateurs situés dans un segment des réseaux terrestres connu sous le nom de réseau d'accès optique (OAN). L'OAN doit donc s'adapter pour répondre à ces demandes de manière flexible et rentable puisque les connexions dans l'OAN sont proportionnelles au nombre d'utilisateurs. Les réseaux optiques passifs (PON) sont actuellement les OAN les plus déployés en raison de leur rentabilité grâce à l'architecture de réseau à division passive et à l'utilisation de la technologie de modulation d'intensité et de détection directe (IM-DD) qui nécessite une optique relativement bon marché. Plusieurs évolutions du PON IM-DD ont été standardisées dans le but de répondre de manière flexible aux exigences de capacité monocanal jusqu'à 10 Gigabits/seconde (Gbps ou G), 25G et récemment 50G-PON. Cependant, cette augmentation de capacité s'accompagne d'un compromis : la rentabilité et les performances sont sacrifiées puisque le PON IM-DD devrait utiliser un traitement de signal numérique (DSP) coûteux pour l'égalisation des canaux et également faire face à la limitation de débit de ligne inhérente au PON IM-DD, de sorte que la détection cohérente (CohD) est envisagée pour le PON (CPON). CohD est la technologie utilisée dans les réseaux centraux. Elle est plus coûteuse que le PON IM-DD et utilise un DSP continu. L'extension du PON IM-DD pour prendre en charge des capacités monocanal de 100G et plus le rapproche en termes de coût du CohD, ce qui motive la contre-stratégie de réduction du coût d'un éventuel CPON qui permettra facilement 100G et plus. Le futur OAN sera donc compatible DSP. Cependant, compte tenu de l'architecture PON asymétrique qui nécessite un fonctionnement en mode rafale, les opérations DSP doivent également être activées en mode rafale pour répondre aux exigences du service CPON. Cela se traduit par une exigence stricte en matière de latence. Considérant également que la dégradation de la dispersion du mode de polarisation (PMD), dans le cas du vieillissement et des fibres aériennes dans l'OAN, peut être élevée et que les algorithmes d'égalisation DSP peuvent être affectés, une analyse minutieuse des propriétés de convergence de l'égalisation DSP est nécessaire. Dans cette thèse, nous abordons le problème de la latence du point de vue DSP en nous concentrant sur l'égalisation adaptative. Tout d'abord, nous proposons un égaliseur adaptatif qui peut surmonter les limitations induites par les conditions environnementales PMD potentiellement larges de l'OAN. Deuxièmement, nous améliorons l'égaliseur adaptatif proposé pour

qu'il s'auto-reconfigure en fonction du niveau de PMD détecté. Enfin, dans le contexte de la réduction globale de la complexité du DSP, nous étudions le potentiel de l'algorithme proposé pour atténuer la dispersion chromatique (CD), réduisant ainsi le besoin d'un bloc DSP d'égalisation CD séparé. L'algorithme proposé atteint une vitesse de convergence, dans tous les cas, bien inférieure au seuil de latence attendu pour 50G-PON et au-delà.

Introduction (Français)

Contexte

Plus de 95 acheminés par des câbles sous-marins en fibre optique [1, 2, 3]. Lorsque le premier câble sous-marin a été installé en 1858, il fallait près de 18 heures pour envoyer un message à travers l'Atlantique. Aujourd'hui, les câbles sous-marins les plus rapides peuvent transférer des données à des vitesses supérieures à 25 téraoctets par seconde (Tbps)- soit plus de deux fois la quantité de données générées par le télescope spatial Hubble chaque année. [4]. Plus de 1,2 million de kilomètres de câbles sous-marins sillonnent les océans du monde entier [4]. En 2023, ces câbles permettront à environ 5,4 milliards de personnes (soit 67% de la population mondiale) d'accéder à l'internet. Ce chiffre représente une augmentation de 45% du nombre d'abonnés à l'internet depuis 2018 [5]. Les utilisateurs/abonnés à l'internet accèdent à l'internet au moyen d'appareils compatibles avec l'internet, les appareils et les connexions augmentant plus rapidement que la population et les utilisateurs de l'internet. utilisateurs de l'internet. En 2023, le nombre mondial d'appareils et de connexions s'élevait à un peu moins de 30 milliards, les applications de machine à machine connaissant la croissance la plus rapide [6]. L'augmentation du nombre d'appareils connectés devrait se poursuivre, en particulier lorsque le monde entrera pleinement dans la quatrième révolution industrielle (Industrie 4.0), qui devrait voir des milliards de personnes et de machines connectées de manière sans précédent, à mesure que la technologie s'intégrera profondément dans les sociétés et que les systèmes cyber-physiques prolifèreront [7].

Si les câbles sous-marins constituent l'épine dorsale de l'internet, reliant des abonnés situés à des milliers de kilomètres les uns des autres, il existe également des câbles terrestres en fibre optique qui relient des abonnés situés dans un rayon géographique plus court. Ces câbles terrestres fournissent des services internet fixes à large bande aux locaux des abonnés et constituent le réseau d'accès optique fixe (OAN). Le réseau d'accès compte le plus grand nombre d'appareils et est à l'origine de la plupart des communications. Par conséquent, comme le nombre d'appareils et les capacités de ces appareils continuent d'évoluer pour répondre aux demandes de services sans cesse croissantes et variables des abonnés/de la société, le réseau doit également évoluer pour prendre en charge les services émergents. C'est cette tendance qui a conduit à la nécessité de passer des câbles coaxiaux aux câbles à fibres optiques dans le réseau d'accès fixe, les câbles à fibres optiques étant supérieurs aux câbles coaxiaux. Par « supérieur », nous entendons que le câble à fibres optiques a une perte plus faible, ne subit pas d'interférences électromagnétiques, est plus léger et a une largeur de bande plus élevée que le câble coaxial. C'est pour cette raison que l'on parle de fibre optique jusqu'au x (FTTx), le 'x' pouvant être remplacé par 'B' pour bâtiment; 'C' pour armoire; 'H' pour maison; 'P' pour local; 'R' pour pièce et, aujourd'hui, 'E' pour tout.

Les qualités supérieures du câble à fibres optiques, qui en font le support le plus appro-

prié pour la transmission d'informations, n'ont pas été obtenues facilement. De nombreuses recherches ont été nécessaires pour réduire la perte à environ 0,2 dB/km, voire moins. Cette capacité de faibles pertes a été optimisée par l'invention d'émetteurs-récepteurs capables d'émettre et de détecter la lumière dans la fenêtre de transmission où les pertes de la fibre sont les plus faibles. Outre l'avantage de pouvoir moduler l'information en fonction de l'amplitude, de la phase ou de la polarisation, l'utilisation de la lumière pour la transmission offre également une plus grande largeur de bande pour la transmission de l'information par rapport à d'autres ondes à basse fréquence du spectre électromagnétique.

Lorsque seule l'amplitude de la lumière est utilisée pour la transmission d'informations, le schéma de transmission est appelé modulation d'intensité et le schéma de détection est appelé détection directe (IM-DD). Lorsque l'amplitude et la phase sont toutes deux utilisées pour la transmission d'informations, il s'agit d'une transmission cohérente qui nécessite un récepteur à détection cohérente (CohD). Les systèmes IM-DD typiques ne peuvent pas récupérer les informations modulées en phase ; ils sont donc plus simples et plus rentables que les systèmes CohD qui sont conçus pour récupérer tous les types d'informations modulées par des ondes lumineuses.

Enjeux

L'OAN évoluera certainement au cours des deux prochaines années pour répondre aux besoins actuels et futurs de services différenciés dans l'industrie 4.0, tels que les transports (systèmes de transport intelligents/contrôle des trains, par exemple), les réseaux mobiles frontaux ou dorsaux, les réseaux intra- et inter-usines, la réalité virtuelle (VR) dans le nuage, la réalité augmentée (AR), l'apprentissage en ligne, la santé en ligne (téléchirurgie, assistance médicale de terrain AR, par exemple), les jeux en ligne (communication holographique, réalité étendue immersive, par exemple), l'internet des sens, etc. [7, 8, 9, 10].

Pour suivre la révolution technologique et l'augmentation de la connectivité mondiale, le futur OAN doit s'adapter à une demande croissante de capacité (largeur de bande) et de nouveaux services [11], l'objectif global étant d'optimiser la bande passante tout en intégrant de manière flexible les nouvelles exigences en matière de services.

Ces services nécessiteront des débits de données très élevés ($>$ 50 Gbps par longueur d'onde), une faible latence ($<$ 2 ms), une faible gigue (2×10^{-9} pour la liaison frontale sans fil) et une faible perte de paquets [12].

Le système devrait également permettre une très forte densification ainsi que différents degrés de consolidation des nœuds, permettre l'intégration des réseaux fixes et sans fil, assurer l'interopérabilité, la rétrocompatibilité et l'évolutivité [13, 14, 15, 16].

Pour répondre à ces exigences, l'OAN doit également rester efficace sur le plan énergétique et économique, avoir une empreinte aussi faible que possible, être modulable et réutiliser la même infrastructure physique [17]. La nécessité de réutiliser la même infrastructure physique existante s'explique par le fait qu'environ 90% du coût de l'OAN est dû à l'infrastructure déployée, qui nécessitera un grand nombre de travaux de génie civil et de procédures administratives pour toute modification.

Actuellement, l'OAN le plus déployé est le réseau optique passif (PON) et il utilise la technologie IM-DD car il bénéficie d'une conception d'émetteur-récepteur/architecture de système simple et rentable - par exemple en ce qui concerne le fait qu'il ne nécessite pas de traitement numérique du signal (DSP) et qu'il utilise des optiques relativement bon marché.

Cependant, ils ne sont pas en mesure de faire face à l'augmentation envisagée de la capacité, à la flexibilité de l'accès multiple et à la réduction de la latence dans le contexte d'une gamme plus large de contraintes de qualité de service des applications futures de

la 6G et de la 6G. En ce qui concerne la capacité, les systèmes IM-DD fonctionnent à des débits binaires d'environ 10 gigabits par seconde (Gbps) par longueur d'onde (λ) seulement, en raison des limitations inhérentes à leur simplicité [18].

Ce débit est bien inférieur aux attentes de la demande future, qui est d'environ 50, 100, 200, voire 400 Gbps/λ. L'une des orientations de la recherche a été d'étendre les performances des systèmes IM-DD [19], bien qu'au détriment de leur faible complexité intrinsèque et de leur architecture simple, vers des débits binaires plus élevés par longueur d'onde grâce à l'utilisation de formats de modulation d'ordre supérieur tels que la modulation d'amplitude d'impulsion quadripartite (PAM-4) et à l'introduction de la DSP [20]. L'utilisation du DSP avec l'IM-DD permet d'atténuer la limitation inhérente au processus de détection de la loi carrée de l'IM-DD, d'améliorer l'efficacité spectrale en récupérant des informations de phase à partir de signaux modulés en intensité et/ou en phase, et de compenser l'utilisation de composants analogiques à bande passante limitée qui sont moins coûteux [21].

Une autre orientation perturbatrice a consisté à changer de technologie pour adopter celle du CohD avec DSP, qui, ensemble, offrent les avantages d'un gain d'efficacité spectrale, d'une sélectivité de fréquence, d'une linéarité et d'une amplification potentielle plus importants, tels qu'ils sont utilisés dans les réseaux centraux et métropolitains. [22].

L'objectif principal de l'utilisation de la CohD est que les quatre degrés de liberté de l'onde lumineuse — l'amplitude et la phase le long de deux affluents de polarisation orthogonaux — sont accessibles grâce à la nature intrinsèque de la transmission cohérente. Cependant, la transmission cohérente est plus coûteuse et plus gourmande en énergie (en termes d'architecture et de DSP). Cela motive donc grandement la recherche de techniques et de conceptions de systèmes qui favorisent une technologie cohérente plus efficace et moins coûteuse [23, 24, 25] — Systèmes OAN coherent lite.

La recherche sur ces systèmes 'cohérents lite' s'accompagne de nombreux défis en raison des spécificités de l'OAN, qui comprennent, entre autres, le fonctionnement en mode rafale (en particulier en amont) [26, 16], la plage de température de fonctionnement (qui doit être large), l'atténuation plus élevée, en particulier dans le PON à séparation passive, la coexistence de nouveaux systèmes et de systèmes existants sur le même réseau de distribution optique, et le partage de l'infrastructure avec une connectivité industrielle critique [16, 27].

Le fonctionnement en mode rafale découle du fait que le PON a une architecture asymétrique dans laquelle un certain nombre de terminaux d'abonnés partagent une unité d'agrégation commune. Chaque terminal d'abonné a besoin de communiquer à des moments différents et envoie des paquets d'informations à des moments différents. L'équipement de réseau sur le site d'agrégation doit être en mesure de traiter chaque salve d'informations provenant de l'abonné. Lorsque le DSP est utilisé dans le système pour corriger les dégradations du canal, tous les algorithmes DSP employés doivent terminer leur opération dans un laps de temps beaucoup plus court que la durée de la salve, afin d'éviter la perte d'informations. L'un des principaux problèmes est donc la latence du traitement numérique du signal. Les systèmes actuellement déployés n'ont pas besoin d'une telle opération DSP puisqu'ils n'utilisent pas de DSP pour compenser les dégradations du canal.

Toutefois, étant donné que le futur système OAN envisagé devra à un moment donné utiliser le DSP, qui n'est pas utilisé dans les systèmes actuellement déployés, nous avons décidé d'axer nos recherches sur le défi que représente le fonctionnement en mode rafale du DSP.

Structure du manuscrit

La contribution et la structure du manuscrit sont les suivantes :

Chapitre 1 : Dans le premier chapitre, nous présentons l'état de l'art des systèmes de communication optique en commençant par un aperçu des concepts de base des systèmes de communication en général et en introduisant ensuite le système de communication par fibre optique (FOC). Nous décrivons ensuite les principes des systèmes FOC en examinant les trois principaux composants d'un système FOC : l'émetteur, le canal de fibre optique et le récepteur. Nous nous concentrons ensuite sur l'OAN - un segment du système FOC qui est géographiquement le plus proche des utilisateurs finaux (c'est-à-dire des abonnés) - et nous décrivons les tendances, les évolutions et les orientations futures envisagées pour l'OAN. Nous présentons ensuite l'état de l'art du traitement numérique du signal (DSP) pour les FOC, en décrivant l'importance du DSP dans les FOC et les algorithmes DSP typiques utilisés. Cela ouvre la voie à la compréhension de l'impact potentiel du DSP en vue de son utilisation dans l'OAN. Nous nous concentrons ensuite sur une classe importante d'algorithmes DSP pour l'égalisation adaptative, car ils semblent être les plus critiques compte tenu de l'architecture asymétrique inhérente à l'OAN, qui nécessitera des algorithmes adaptatifs efficaces et rapides pour le fonctionnement en mode rafale. Nous étudions en particulier la propriété de convergence de l'égaliseur adaptatif de l'algorithme à module constant (CMA) en abordant son problème de convergence appelé *singularité*.

Chapitre 2 : Dans le deuxième chapitre, nous nous appuyons sur l'exigence, établie dans le chapitre précédent, d'un algorithme adaptatif efficace et rapide dans l'OAN en examinant diverses propositions pour résoudre le problème de singularité du CMA. Nous étudions ensuite une approche basée sur la corrélation proposée pour l'atténuation de la singularité et obtenons des informations qui conduisent au développement d'un nouvel algorithme à module constant d'évitement de la corrélation (CA-CMA) pour l'évitement de la singularité. Ensuite, nous analysons la capacité d'évitement des singularités de l'algorithme CA-CMA en le soumettant à une large gamme de conditions extrêmes de dispersion des modes de polarisation (PMD) — un test robuste typique des conditions extrêmes de canal auxquelles l'OAN serait exposé — et nous présentons les résultats. Nous présentons également une discussion sur la performance de singularité du CA-CMA, ses inconvénients et les stratégies potentielles pour améliorer sa performance de singularité et ses capacités de convergence. Tout en considérant une réduction globale de la complexité du DSP, nous étudions également le potentiel du CA-CMA à fonctionner dans un scénario de dispersion chromatique (CD) non compensée et montrons que le CA-CMA est capable de mieux éviter les singularités que le CMA standard et le schéma existant basé sur la corrélation. Par conséquent, une réduction globale de la complexité du DSP peut être obtenue en laissant le CA-CMA gérer la majeure partie de la CD.

Chapitre 3 : Dans le troisième chapitre, nous tentons de trouver des solutions aux inconvénients du CA-CMA présentés dans le chapitre précédent en réglant correctement le CA-CMA pour qu'il corresponde à l'effet de l'altération du canal. Cela améliore la sensibilité de l'algorithme à suivre et à prévenir les singularités dans une gamme donnée de PMD. Les résultats permettent de mieux comprendre la relation entre l'étendue de la PMD et les paramètres du CA-CMA. Nous utilisons ensuite ces informations pour développer un CA-CMA adaptatif avancé capable d'ajuster ses paramètres en fonction de l'étendue de la PMD rencontrée. Nous étudions également le potentiel de ce CA-CMA avancé pour traiter les CD et nous montrons qu'il offre de meilleures performances en

matière de singularité que le CMA standard et le schéma existant basé sur la corrélation.

Cette thèse a été réalisée grâce à une bourse industrielle CIFRE N° 2021/ 0475 entre Mitsubishi Electric Research & Development Center Europe (MERCE) et Télécom Paris (Institut Polytechnique de Paris).

Acronyms

AAU active antenna unit
ADC analog-to-digital converter
AEQ adaptive equalization
AON active optical network
APD avalanche photodiode
AR augmented reality
ASE amplified spontaneous emission
ASIC application-specific integrated circuit
AWGN additive white Gaussian noise
BBU baseband unit
BCH Bose-Chaudhuri-Hocquenghem
BER bit error ratio
BIF bend-insensitive fiber
BPD balanced photodiode
BPON broadband passive optical network
BPS blind phase search
BPSK binary phase-shift-keying
BRF bend-resistant fiber
CA-CMA correlation-avoidance constant modulus algorithm
CD chromatic dispersion
CFO carrier frequency offset
CMA constant modulus algorithm
CMOS complementary metal-oxide semiconductor
CohD coherent detection
CPE carrier phase estimation
CPON coherent passive optical network
CU central unit
CW continuous wave
DAC digital-to-analog converter
DB duobinary
DCO digital coherent optics/ optical
DD direct detection
DFB distributed feedback
DGD differential group delay
DMT discrete multitone
DP dual-polarization
DS downstream
DSP digital signal processing
DU distributed unit

E2E end-to-end
EDFA erbium-doped fiber amplifier
EPON ethernet passive optical network
FEC forward error correction
FFE feedforward equalizer
FFT fast Fourier transform
FIR finite impulse response
FOC fiber optic communication
FS fractionally-spaced
FSE fractionally-spaced equalizer
FTTx fiber-to-the-x (x = B:building, C:cabinet, H:home, P:premise, R:room, E:everything)
FWM four-wave mixing
G giga
GaAs gallium arsenide
Gbps gigabits per second
GPON gigabit-capable passive optical network
GVD group velocity dispersion
HS-PON Higher speed passive optical network
I/Q in-phase/ quadrature
IEC international electrotechnical commission
IEEE institute of electrical and electronic engineers
IFFT inverse fast Fourier transform
IM-DD intensity modulation and direct detection
InGaAsP indium gallium arsenide phosphide
ISI inter-symbol interference
ISO international organization for standards
ITU international telecommunication union
ITU-T international telecommunication union – telecommunications
KK Kramers-Kronig
LASER light amplification by stimulated emission of radiation
LDPC low-density parity check
LED light-emitting diode
LMS least mean square
LO local oscillator
MAC medium access control
Mbps megabits per second
MIMO multiple-input multiple-output
MMF multimode fiber
MSA multisource agreement
MU-CMA multi-user constant modulus algorithm
MZM Mach-Zehnder modulator
NG-EPON Next generation Ethernet passive optical network
NG-PON (Next generation) 40-gigabit-capable passive optical network
NLSE nonlinear Schrodinger equation
NRZ non-return-to-zero
OAN optical access network
ODN optical distribution network
OECD organization for economic cooperation and development
OLT optical line termination
ONU optical network unit

OOK on-off-keying
OVS overlap-and-save
P2MP point-to-multipoint
P2P point-to-point
PAM pulse amplitude modulation
PBC polarization beam combiner
PBS polarization beam splitter
PD photodiode
PDL polarization dependent loss
PDM polarization division multiplexing/ multiplexed
PIN positive-intrinsic-negative
PMD polarization mode dispersion
PON passive optical network
PSK phase-shift-keying
PSP principal state of polarization
QAM quadrature amplitude modulation
QPSK quadrature phase-shift-keying
RHS right-hand side
RN remote node
RRC root raised cosine
RRU remote radio unit
RS Reed-Solomon
SBS stimulated Brillouin scattering
SMF single mode fiber
SNI service node interface
SNR signal-to-noise ratio
SPM self-phase modulation
SRS stimulated Raman scattering
SSMF standard single mode fiber
Tbps terabits per second
TDM time division multiplexing/ multiplexed
TIA telecommunication industry association
TIA transimpedance amplifier
TWDM time and wavelength division multiplexing/ multiplexed
UNI user network interface
US upstream
VR virtual reality
WDM wavelength division multiplexing/ multiplexed
XG-PON 10-gigabit-capable passive optical network
XGS-PON 10-gigabit-capable symmetric passive optical network
XPM cross-phase modulation

Contents

List of Figures

List of Tables

Introduction

If I have seen further, it is by standing on the shoulders of giants.

— Isaac Newton

Context

More than 95 percent of international data and voice transfers are currently routed through submarine fiber optic cables [1, 2, 3]. When the first submarine cable was installed in 1858, it took nearly 18 hours to send a message across the Atlantic. Today, the fastest undersea cables can transfer data at speeds exceeding 25 terabytes per second (Tbps) - more than twice the amount of data generated by the Hubble Space Telescope each year [4]. There are more than 1.2 million km of undersea cables that crisscross the world's oceans [4]. As of 2023, these cables were responsible for granting approximately 5.4 billion people (i.e. 67% of the world's population) internet access. This number represents a 45% increase in the amount of internet subscribers since 2018 [5].

Internet users/ subscribers access the internet by means of internet-enabled devices with the devices and connections growing faster than both the population and the internet users. In 2023 the global number of devices and connections stood just under 30 billion with machine-to-machine applications experiencing the fastest growth [6]. The increase in number of connected devices is expected to continue especially as the world transitions fully into the fourth industrial revolution (Industry 4.0) which is expected to see billions of people and machines connected in unprecedented ways as technology becomes deeply embedded within societies alongside the proliferation of cyber-physical systems [7].

While submarine cables form the backbone of the internet, connecting subscribers located thousands of kilometers apart, there are also terrestrial fiber optic cables that connect subscribers located within a shorter reach geographical location. Such terrestrial cables provide broadband fixed internet services to the subscribers' premises and make up the fixed optical access network (OAN). The access network has the greatest device count and is the origin of most communications. Hence as the number of devices and the capabilities of these devices continue to evolve to meet the ever growing and varying service demands of the subscribers/ society, the network must also evolve to support the emerging services. This has been the trend that led to a global need for transitioning from coaxial cables to fiber optic cables in the fixed access network since fiber optic cables are superior to coaxial cables. By superior we mean that the fiber optic cable has lower loss, no electromagnetic interference, lighter size and weight, and higher bandwidth when compared to the coaxial cable. It is for this reason that we have the terminology fiber-to-the-x (FTTx) where 'x' could be replaced with 'B' for building; 'C' for cabinet; 'H' for home; 'P' for premise; 'R' for room; and nowadays 'E' for everything.

The superior qualities of the fiber optic cable that make it the most suitable medium for information transmission did not come easily. A lot of research had to be done to bring down the loss to about 0.2 dB/km and even lower. This low loss capability was maximized by the invention of transceivers that could emit and detect light in the transmission window where the fiber losses are lowest. Apart from having the advantage that information can be modulated on either its amplitude, phase, or polarization, the use of light for transmission also avails greater bandwidth for information transmission compared to other lower frequency waves of the electromagnetic spectrum.

When only the amplitude of the light is utilized for information transmission the transmission scheme is referred to as intensity modulation and the detection scheme is referred to as direct detection (IM-DD). When the both the amplitude and the phase are utilized for information transmission then we have a coherent transmission which requires a coherent detection (CohD) receiver. Typical IM-DD systems cannot retrieve phase-modulated information; hence they are simpler and more cost-effective than CohD systems which are designed to retrieve all kinds of light wave-modulated information.

Challenges

The OAN will definitely evolve in the next couple of years to support current and evolving needs for differentiated services in industry 4.0 such as transportation (e.g. intelligent transport systems/ train control), mobile front-haul or back-haul, intra- and inter-plant networks, cloud virtual reality (VR), augmented reality (AR), e-learning, e-health (e.g. telesurgery, AR field medical support), online gaming (e.g. holographic communication, immersive extended reality), internet of senses, etc. [7, 8, 9, 10].

To keep up with the technological revolution and increase in global connectivity, the future OAN must adapt to and accommodate an increasing demand for capacity (bandwidth) and new services [11] with an overall goal to optimize bandwidth while flexibly integrating new service requirements.

These services will require very high data rates ($>$ 50 Gbps per wavelength), low latency ($<$ 2 ms), low jitter (2×10^{-9} for wireless fronthaul), and low packet loss [12]. The system would also need to support very high densification as well as different degrees of node consolidation, enable integrated fixed and wireless networks, achieve interoperability, backward compatibility, and scalability [13, 14, 15, 16].

In fulfilling these requirements, it is also required that the OAN remains energy efficient, cost-efficient, have as small foot-print as possible, be scalable, and reuse the same physical infrastructure [17]. The need for reuse of the same existing physical infrastructure arises because about 90% of the cost of the OAN is due to the deployed infrastructure which will require a great amount of civil work and administrative processes for any modification.

Currently, the most deployed OAN is the passive optical network (PON) and it utilizes the IM-DD technology since they benefit from a simple and cost-effective transceiver design/ system architecture — e.g. with respect to their not requiring digital signal processing (DSP) and their use of relatively cheap optics. However, they are not able to cope with the envisioned increase in capacity, multiple access flexibility, and reduced latency in a context of wider range of quality of service constraints of 6G and 6G future applications. Concerning the capacity, IM-DD systems operate at bit rates of only about 10 gigabits per second (Gbps) per wavelength (λ) due to inherent limitations brought about by their simplicity [18]. This line rate is much lower than future demand expectations of about 50-, 100-, 200-, and even 400 Gbps/λ. One research direction has been to extend the performance of IM-DD systems [19], though at the expense of their intrinsic low complexity and simple architecture, towards higher bit rates per wavelength by the use of higher order modulation formats such as 4-ary pulse-amplitude-modulation (PAM-4) and introducing DSP [20]. The use of DSP with IM-DD is to mitigate the inherent limitation of the square law detection process of IM-DD, to improve the spectral efficiency by retrieving phase information from intensity and/ phase modulated signals, and to compensate for the use of bandwidth-limited analog components that are less expensive [21].

Some other disruptive direction has been to change the technology to that of CohD with DSP, which acting together, have the benefits of greater spectral efficiency gain, frequency selectivity, linearity, and potential amplification as used in the core- and metro-networks [22]. The main purpose of using CohD is that all four degrees of freedom of the light wave — amplitude and phase along two orthogonal polarization tributaries — are accessible by the intrinsic nature of coherent transmission. However, coherent is more expensive and power-hungry (in terms of architecture and DSP). This therefore, greatly motivates research for techniques and system designs that favor a more efficient and less expensive coherent technology OAN [23, 24, 25] — coherent lite OAN systems.

The research on such 'coherent lite' systems comes with lots of challenges due to

the specifics of the OAN which include, but are not limited to, burst-mode operation (especially in the upstream) [26, 16], operating temperature range (that needs to be wide), higher attenuation especially in the passive splitting PON, coexistence of new systems and legacy systems on the same optical distribution network, and infrastructure sharing with mission-critical industrial connectivity [16, 27].

Burst-mode operation arises from the fact that the PON has an asymmetric architecture where a number of subscriber terminals share a common aggregation unit. Each subscriber terminal will have a need to communicate at different times and sends bursts of information at different times. The network equipment at the aggregation site should be able to serve each burst of information from the subscriber. When DSP is utilized in the system to correct for channel impairments, then all the DSP algorithms employed would have to complete their operation in a time frame much shorter than the burst duration, in order to prevent information loss. Hence a key issue here is the latency of the DSP . There has been no need for such DSP operation in the currently deployed systems since they do not use DSP to compensate for the channel impairments.

However, as the envisioned future OAN will at some point have to employ DSP, which is not used in currently deployed systems, we decide to focus our research on the challenge of burst-mode operation for the DSP.

Thesis contribution and structure of manuscript

The contribution and structure of the manuscript are as follows:

Chapter 1 : In the first chapter we present the state-of-the-art of optical communication systems starting with an overview on basic concepts of communication systems in general and then introducing the fiber optic communication system (FOC). We then describe the principles of FOC systems by discussing the three main components of an FOC system — the transmitter, the optical fiber channel, and the receiver. Next we narrow our focus to the OAN — a segment of the FOC system that is geographically closest to the end-users (i.e. subscribers) — and describe the trends, evolutions, and future directions envisioned for the OAN. We then introduce the state-of-the-art of digital signal processing (DSP) for FOC, describing the importance of DSP in FOC and the typical DSP algorithms utilized. This paves the way for understanding the potential impact of DSP in consideration of its use in the OAN. Then we finally focus on an important class of DSP algorithms for adaptive equalization since they seem to be the most critical considering the inherent asymmetric architecture of the OAN which will require efficient and fast adaptive algorithms for burst mode operation. We particularly study the convergence property of the constant modulus algorithm (CMA) adaptive equalizer addressing its convergence issue referred to as *singularity*.

Chapter 2 : In the second chapter we build on the requirement, established in the previous chapter, for an efficient and fast adaptive algorithm in the OAN by examining various proposals for solving the singularity issue of the CMA. We then investigate a correlation-based approach proposed for singularity mitigation and obtain insights leading to the development of a novel correlation-avoidance constant modulus algorithm (CA-CMA) for singularity avoidance. Next, we analyze the singularity avoidance capability of the CA-CMA subjecting it to a wide range of extreme channel conditions of polarization mode dispersion (PMD) — a robust test typical of the extreme channel conditions that the OAN would be exposed to — and present the results. We also provide a discussion on the

singularity performance of the CA-CMA, its drawbacks, and potential strategies for further improving its singularity performance and convergence capabilities. While considering an overall reduction in the DSP complexity, we also investigate the potential of the CA-CMA to operate in an uncompensated chromatic dispersion (CD) scenario and show that the CA-CMA is able to achieve better singularity avoidance than the standard CMA and the existing correlation-based scheme. Hence an overall reduction in DSP complexity can come from letting the CA-CMA handle most of the CD.

Chapter 3 : In the third chapter we attempt to provide solutions to the highlighted drawbacks of the CA-CMA introduced in the previous chapter by properly tuning the CA-CMA to match the effect of the channel impairment. This improves the sensitivity of the algorithm to track and prevent singularities over a given range of PMD. The results provide insight to the relationship between the extent of the PMD and the parameters of the CA-CMA. We then use this insight to develop an advanced adaptive CA-CMA that is able to tune its parameters depending on the extent of the PMD encountered. We also investigate the potential of this advanced CA-CMA to handle CD and we show that it has better singularity performance compared to the standard CMA and the existing correlation-based scheme.

This thesis was carried out through an industrial grant CIFRE N° 2021/ 0475 between Mitsubishi Electric Research & Development Center Europe (MERCE) and Télécom Paris (Institut Polytechnique de Paris).

CHAPTER 1

State-of-the-art of optical communications systems

Whatever you vividly imagine, ardently desire,
sincerely believe, and enthusiastically work upon,
will inevitably come to pass.
— Paul J. Meyer

Contents

1.1 Overview of communication systems

The purpose of a communication system is to transmit information from one location to another location in a reliable manner — meaning that we would like to receive exactly the information that was transmitted. One measure to quantify the reliability of the communication is the bit error ratio (BER) which we shall see later on.

The basic architecture of a communication system includes a transmitter, the communication channel, and a receiver. The information signal is usually modulated onto a carrier signal for transmission along the communication channel. The transmitter generates the carrier signal and performs the modulation to give a modulated signal that is suitable for transmission over the communication channel. The channel is the medium through which the modulated/ transmitted signal is conveyed from the transmitter to the receiver. It is usually not perfect and so suffers from impairments e.g. noise, attenuation (or loss), and interference that alter the transmitted signal. The receiver decodes the impaired received signal, which has been distorted by the channel, to recover the originally transmitted information signal.

The communication channel could either be wired (guided) or wireless (unguided) and the choice of the type of channel depends on the objectives or requirements of the communication since different kinds of channels impact the transmitted signal in a different way leading to pros and cons for the channel types. Hence, there are various performance metrics for various types of channels. With a wired channel we have more control of the communication medium than in a wireless channel as we can design specific wired channels to suit the communication need. This has led to several evolutions of the wired channel all the way to the fiber optic channel as seen in Table 1.1.

Table 1.1: Development of wired communication channels up to optical fibers

Channel type	**Bandwidth**
Twisted-pair wireline	Several hundred kHz
Coaxial cable	Several MHz
Waveguide	Several GHz
Optical fiber	Several THz

The first three wired communication channels are copper-based and are limited in achievable bandwidth because of the skin effect which increases with frequency. Optical fiber channels on the other hand do not suffer from this effect and can reach several THz in bandwidth. The major advantages of optical fiber channels are as follows [34]:

- Low loss — as low as 0.144 dB/km [35] compared to 44 dB/km for coaxial cable at 600 MHz.
- Wide bandwidth — up to 10^6 times the bandwidth of coaxial cable.
- Small size and weight — outer diameter (245 μm) [36] more than 4 times smaller than outer diameter (1 mm) of coaxial cable [37].
- Immunity to electromagnetic interference

1.2 Optical fiber communication system

The fiber optic communication (FOC) system is a communication system in which the communication channel is the fiber optic cable.

The aforementioned advantages of the fiber optic channel indicate the capability of fiber optic communications to meet increasing demands for bandwidth and long reach which can be jointly quantified by a bandwidth-distance product metric. Such requirements alongside the technological advancements in the design of FOC system components (e.g. narrow linewidth lasers, high-speed modulators, low loss fibers, etc.) are responsible for the preponderance of fiber optic communication systems. This has led to evolutions of the FOC system across a number of generations as summarized in Table 1.2 below:

Table 1.2: Generations of fiber optic communications. GaAs: Gallium Arsenide, InGaAsP: Indium Gallium Arsenide Phosphide, IM-DD: Intensity modulation direct detection, Mbps: Megabits per second, DFB: Distributed feedback, CD: Chromatic dispersion, EDFA: Erbium-doped fiber amplifier, WDM: Wavelength division multiplexing, ADC: Analog-to-digital converter, DAC: Digital-to-analog converter, DSP: Digital signal processing, FEC: Forward error correction.

Generations	**Key enabler**	**Typical characteristics**
1^{st} generation (1960 – 1980)	Invention of laser GaAs @ 850 nm Multimode fiber	IM-DD 45 Mbps, repeaters every 10 km
2^{nd} generation (1980 – 1987)	DFB laser InGaAsP @ 1330 nm Single mode fiber	IM-DD $<$ 100 Mbps 1.7 Gbps, repeaters every 50 km
3^{rd} generation (1990)	DFB laser @ 1550 nm, 0.2 dB/km CD compensation	IM-DD 10 Gbps, repeaters every 80 km
4^{th} generation (1992)	Invention of EDFA WDM adoption	IM-DD Boost in bandwidth-distance metric 1-2 Tbps, repeaters every 80 km
5^{th} generation (2000s)	Coherent detection Polarization multiplexing DACs, ADCs, DSP, FEC	Coherent detection

Each new generation presents a solution to the problems of the previous generation but also creates new challenges.

In Table 1.1 we note that the bandwidth of the optical fiber is in the order of several THz. It corresponds to the infrared region of of the electromagnetic spectrum. Depending on the particular frequency (or wavelength) of the electromagnetic signal, the optical fiber channel exhibits different characteristics which we shall soon see.

For the purpose of telecommunications using the optical fiber, the electromagnetic spectrum is divided into the following wavelength bands:

- O-band (1260 nm – 1360 nm): Original band
- E-band (1360 nm – 1460 nm): Extended band
- S-band (1460 nm – 1530 nm): Short wavelength band
- C-band (1530 nm – 1565 nm): Conventional band
- L-band (1565 nm – 1625 nm): Long wavelength band

A group of connected communication systems form the physical layer of a communication network. The span/ reach (i.e. distance between a transmitter and a receiver) of a communication network may vary. Hence communication networks may be categorized by reach as core networks, metro/ transport/ aggregation networks, and access networks.

The access network is that part of the network that connects the subscribers to the central office and may span a few meters to tens of kilometers. The metro/ transport network aggregates traffic from a number of central offices towards a main or core central office and may span hundreds of kilometers. The core network connects the core central offices and may span several thousands of kilometers.

Depending on the reach, wired communication networks may also be informally classified as short-reach or long-reach networks. Typical examples of short-reach networks are intra-datacenter networks while the metro and core networks are long-reach. Access networks are somewhere between short-reach and long-reach, but closer to the short-reach portion. Fig. 1.1a shows the world-wide connectivity fiber optic map consisting of both inter-continental and intra-continental fiber optic cables.

A constant demand for better quality of service, quality of experience, and increased bandwidth/ capacity by the end-users/ subscribers of the network has led to constant innovation in the access network. Due to the large number of end-users in the access network, it is a delicate section of the communication network because of its potential cost which scales as the number of subscribers if, for instance, point-to-point links are used. This requires special care on the identification of network topologies/ architectures that circumvent this cost constraint.

The cost constraint therefore makes the access network asymmetrical, in that we would like to have cheaper network nodes for the subscribers who can share a more expensive aggregation node.

The ever-increasing capacity demand in the access network has seen the wired access network evolve from the use of coaxial cables to the use of optical fiber cables due to the inherent advantages of the optical fiber as earlier outlined. This lead to the concept of the wired optical access network with terminologies such as fiber-to-the-x (FTTx), where 'x' could be replaced with 'B' for building; 'C' for cabinet; 'H' for home; 'P' for premise; 'R' for room; and nowadays 'E' for everything. Fig. 1.1b shows the density of FTTH subscribers, for example, in France. More than 66% of the country is currently covered with FTTH. This is shown in Fig. 1.2 which presents the evolution of fiber optic connections as a percentage of the total fixed broadband connections from the year 2019 to 2023 for the member countries of the organization for economic cooperation and development (OECD).

The fiber deployment in the optical access could either be aerial (in the air) or, the most common deployment, as underground cables. For cost and application considerations, the architecture of the optical access could either be point-to-point (P2P) or point-to-multipoint (P2MP). In P2P, a dedicated fiber cable is required between two end points for upstream (i.e. communication from the subscriber towards a central office) and for downstream (i.e. communication from a central office down to the subscriber). In P2MP, two architectures are possible: the active optical network (AON) with active devices (i.e. transmitters) in a fan out node, or the passive optical network (PON) with only passive devices (i.e. passive splitters) in a fan out node.

The PON architecture is the cheapest configuration of the optical access network for scalability consideration and it dominates the optical access due to its cost effectiveness. To meet the increasing demand for capacity, the PON has also been evolving, with various generations of the PON standardized and deployed, and newer generations undergoing standardization by the international telecommunication union - telecommunications (ITU-T) and the institute of electrical and electronic engineers (IEEE).

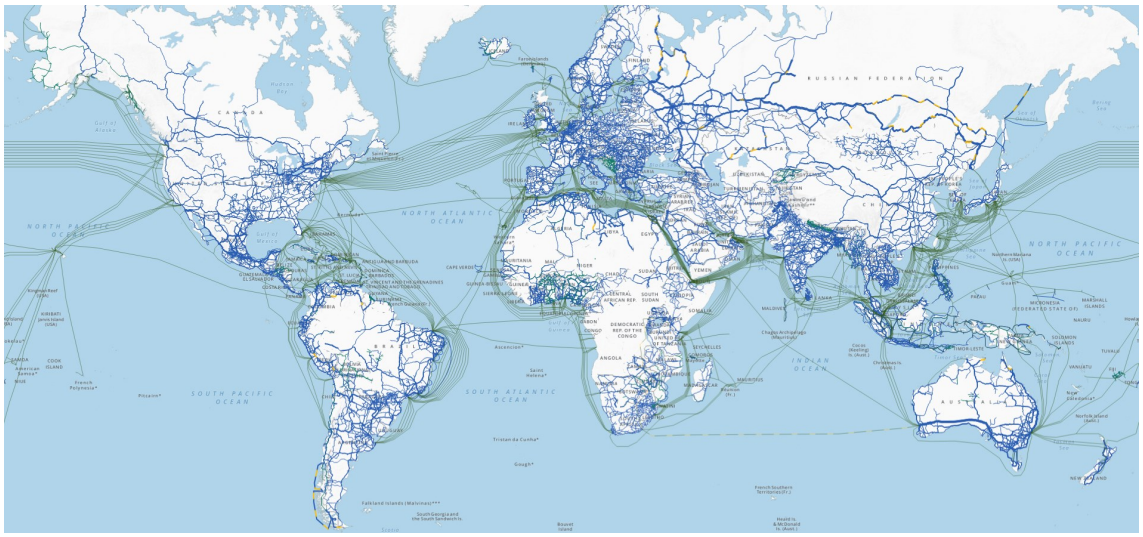

(a)

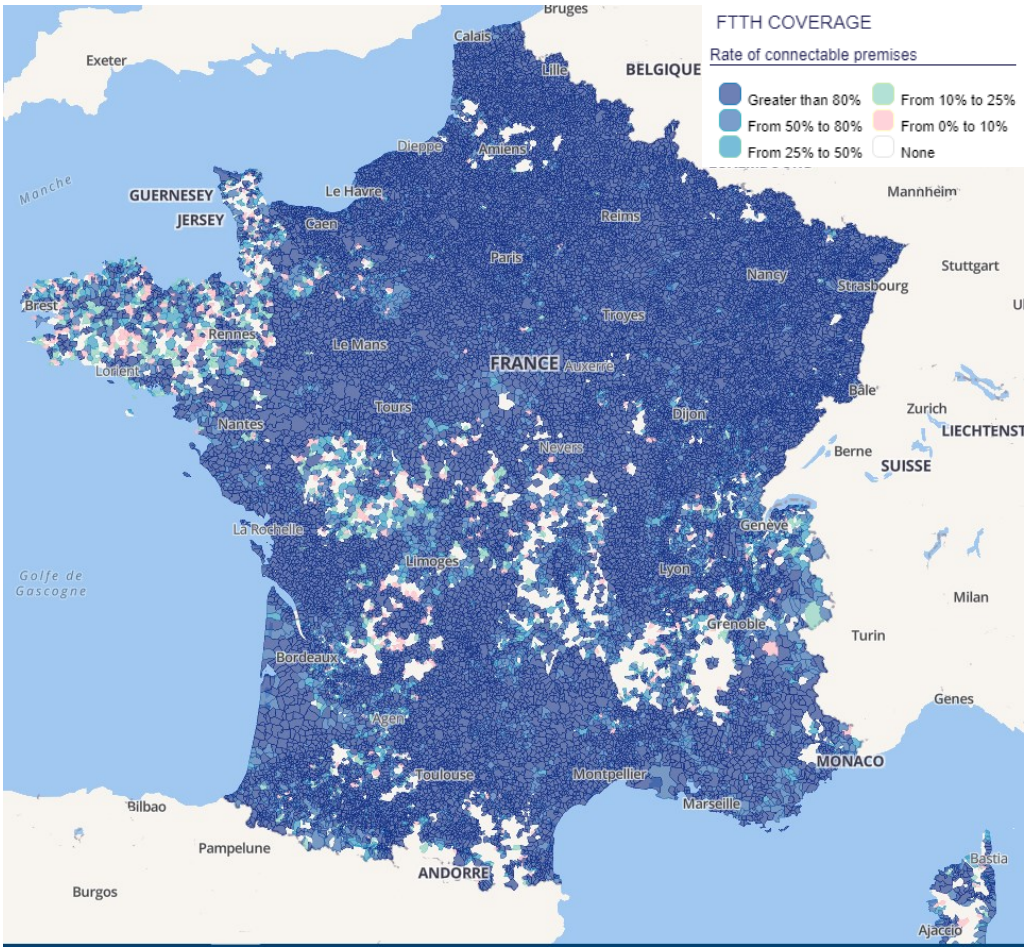

(b)

Figure 1.1: Fiber deployment map (a) World-wide connectivity map, adapted from [28] (b) FTTH coverage in France adapted from [29].

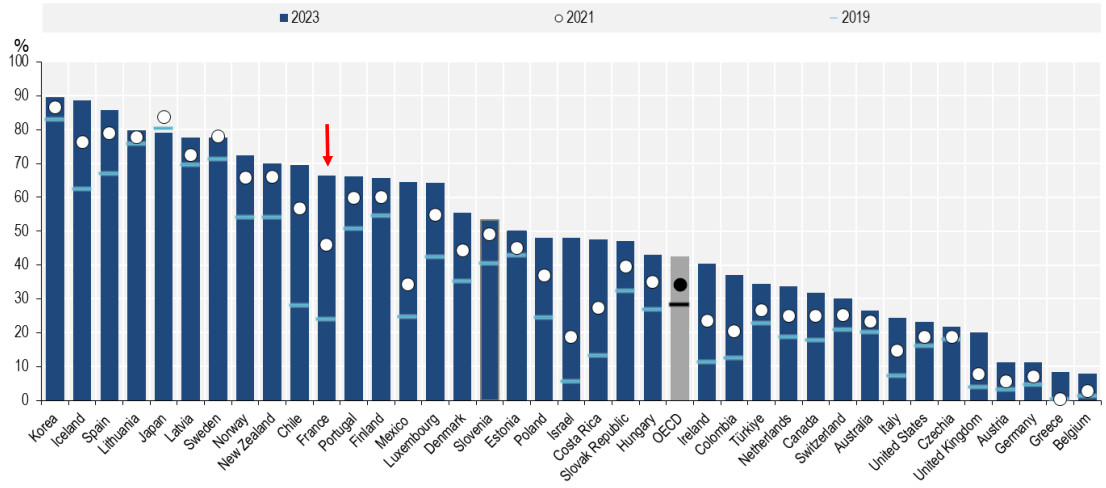

Figure 1.2: Percentage of fiber connections in total fixed broadband, from [30].

We would get to look at the evolutions of the PON in section 1.3 but before doing that, it is important to have a lower level view of the optical fiber communication system as some concepts would be needed to better understand the peculiarities of specific PON generations.

The optical fiber communication system is made up of three broad systems — an optical transmitter, the fiber optic channel (optical fiber), and an optical receiver. The optical fiber can be utilized in either of the wavelength bands earlier presented even though it has very different characteristics in each wavelength band. On the other hand, the optical transmitters and receivers need to be specially designed to suit the particular wavelength band.

Usually the information to be transmitted is generated by an information source in digital form and then, by means of complementary metal-oxide semiconductor (CMOS)-based digital-to-analog converters (DACs), the digitized information is converted to analog and used to modulate an analog optical carrier. The modulated analog signal is then transmitted over the fiber channel and converted back into digital form via CMOS-based analog-to-digital converters (ADCs) at the receiver. The reliability of the transmission can then be determined by counting the number of bits that arrived with errors and dividing this number by the total number of bits transmitted, to give the bit error ratio (BER).

A lot of progress in high-speed optical fiber communication is thanks to the advancement in CMOS application-specific integrated circuits (ASICs) that enabled the development of high-speed ADCs and DACs with sampling rates commensurate with the optical line rate. This was beneficial for digital demodulation utilizing a type of receiver referred to as intradyne coherent receiver [38, 39]. The CMOS technology also enabled the implementation of digital signal processing (DSP) algorithms in the ASIC.

We will proceed to briefly describe the components of the fiber optic communication system and their characteristics, after which, in section 1.4 we will briefly describe the typical DSP processes that are utilized for fiber optic communications. In both cases, we will focus on the important points that will be useful for understanding concepts that will come up in later sections and chapters.

1.2.1 The optical transmitter

The optical transmitter is the source of the light wave (infrared wave for the optical channel described in section 1.2.2) which is the carrier signal for information transmission in an optical network. This light is generated by the use of a semiconductor (diode) which could either be a light-emitting diode (LED) or a laser (light amplification by stimulated emission of radiation) diode that emits the light at an appropriate wavelength when sufficiently pumped with electric current. For telecommunication applications laser diodes are utilized because they can produce a more coherent light beam than LEDs, and at a higher power (> 10 mW).

The most important laser parameters are its threshold current and its slope efficiency which measures the current-to-light-conversion efficiency. These parameters are affected by temperature and age, hence with increasing temperature and as time passes, the laser threshold current increases exponentially and its slope efficiency decreases linearly [40].

Various types of lasers exist depending on the emitted light wave spectrum. They could be e.g. Fabry-Perot laser, distributed feedback (DFB) laser, etc. The Fabry-Perot laser spectrum is broad and is not suitable for telecommunication. The DFB lasers are able to achieve a single mode operation and are suitable for telecommunication. There could also be tunable lasers which can be operated to emit at specific wavelengths, making them interesting for wavelength division multiplexed (WDM) transmission systems.

Depending on how the carrier wave emitted from the laser is modulated by the information signal, the transmitter can be categorized as either directly modulated or externally modulated.

For direct modulation, the laser pump/ drive current varies as the intensity of the information signal. For example, in the simplest kind of direct modulation referred to as On-off-keying (OOK), the laser emits light when the digitized information signal has a non-zero value, and does not emit light when the information signal value is zero.

It is a simple scheme but it has the draw-back of laser chirp. This means that the intensity modulation causes a change in the optical carrier density which leads to a modification of the refractive index of the lasing medium and hence a drift in the output frequency [41, 42].

For externally modulated lasers or continuous wave (CW) lasers, the laser pump current remains continuously on while the emitted light is modulated by means of an external modulator, and the modulated light is almost chirp-free.

The electric field of the light wave can be mathematically represented by Eq. (1.1) [43] below as

$$\mathbf{E}(z,t) = \Re\{\mathbf{x}E_x e^{j(\omega t - \beta z + \Phi_x)} + \mathbf{y}E_y e^{j(\omega t - \beta z + \Phi_y)}\} \tag{1.1}$$

where ω is the optical angular frequency; E_x and E_y are the field amplitudes along the $\mathbf{x}$ and $\mathbf{y}$ directions; $\beta = \overline{n}k_0 = \overline{n}2\pi/\lambda$ is the propagation constant with $\overline{n}$ the effective refractive index; λ the wavelength; Φ_x, Φ_y are the absolute phases; $j = \sqrt{-1}$. The $\mathbf{x}$ and $\mathbf{y}$ directions are the orthogonal polarization directions of the light wave. In a vacuum the polarization of a light wave is determined by the direction of oscillation of the electric field and $\overline{n} = 1$.

There are random fluctuations in the absolute phases Φ_x, Φ_y of the light wave referred to as phase noise and it arises from two main sources which have different statistical properties: laser phase noise and nonlinear phase noise. Laser phase noise is an intrinsic property of semiconductor laser due to the spontaneous emission process which causes a random walk of the optical phase. This in turn results in a finite laser linewidth (i.e. the width of the frequency spectrum of the emitted light wave). Laser phase noise is similar for both orthogonal polarizations. Nonlinear phase noise will be defined in the

next subsection.

A close look at Eq. (1.1) shows that there are three degrees of freedom for modulation of the light wave — intensity, phase, and polarization. When only the intensity of the light wave is modulated by the information signal, the signal can be recovered at the receiver by ***direct detection***. This scheme is referred to as intensity modulation and direct detection (IM-DD). When both the intensity and phase of the light wave are modulated by the information signal we can have a complex representation of the electric field yielding in-phase and quadrature field components. The signal can then be recovered at the receiver by a ***phase diverse coherent detection*** scheme. When the intensity, phase, and polarization of the light wave are modulated by the information signal, the signal can be recovered at the receiver by a ***polarization and phase diverse coherent detection*** scheme. The more the degrees of freedom of the light wave that are modulated, the greater is the information transmission capacity of the modulation i.e. the spectral efficiency of the modulation scheme.

Optical modulators The optical modulator modulates the optical carrier with the information signal. It could either be an acousto-optic, electro-absorption, or electro-optic modulator.

Acousto-optic modulators work on the principle of the acousto-optic effect where sound waves alter the refractive index of the modulator medium thereby modulating the light wave passing through it.

Electro-absorption modulators operate on the principle of the Franz-Keldysh effect where an electric voltage changes the absorption spectrum of the modulator medium thereby modulating the intensity of the light wave passing through it.

Electro-optic modulators work on the principle of the Pockels effect where the refractive index of a material (e.g. lithium niobate crystal) changes on application of an electric voltage [44].

The Mach-Zehnder modulator (MZM) is an interferometric modulator that depends on the Pockels effect. It can be used to generate different kinds of modulation formats. The electric voltage applied on one arm causes the refractive index to change thereby causing a change in the velocity of the light in that arm. This could lead to destructive or constructive interference of the light wave in both arms of the MZM. An important parameter of the MZM is the value of the voltage, V_π required to cause a phase shift of π radians between both arms of the MZM [45]. Modulators with low V_π values are preferable for energy efficiency reasons.

Modulators are capable of producing various kinds of modulation formats depending on the property of the light wave that is modulated. They can generate pulse amplitude modulation (PAM), phase-shift-keying (PSK), quadrature amplitude modulation (QAM), and the dual polarization versions of PAM, PSK, and QAM. The choice of the modulation format depends on the spectral efficiency required and the cost of achieving it.

1.2.2 The optical fiber channel

The optical fiber channel is made up of the fiber optic cable (which includes the inner core, the outer cladding — for guiding light —, and other outer non-optical protective coverings that provide mechanical strength to the cable), inline optical components and devices such as connectors, splitters, optical amplifiers, etc. There are different kinds of fiber optic cables depending on the design of the light guiding portion (i.e. the core and the cladding) of the cable. These could either be single mode-, multimode-, multicore-, or hollow core fibers. The standard single mode fiber optic cable is made up of silica glass and is composed

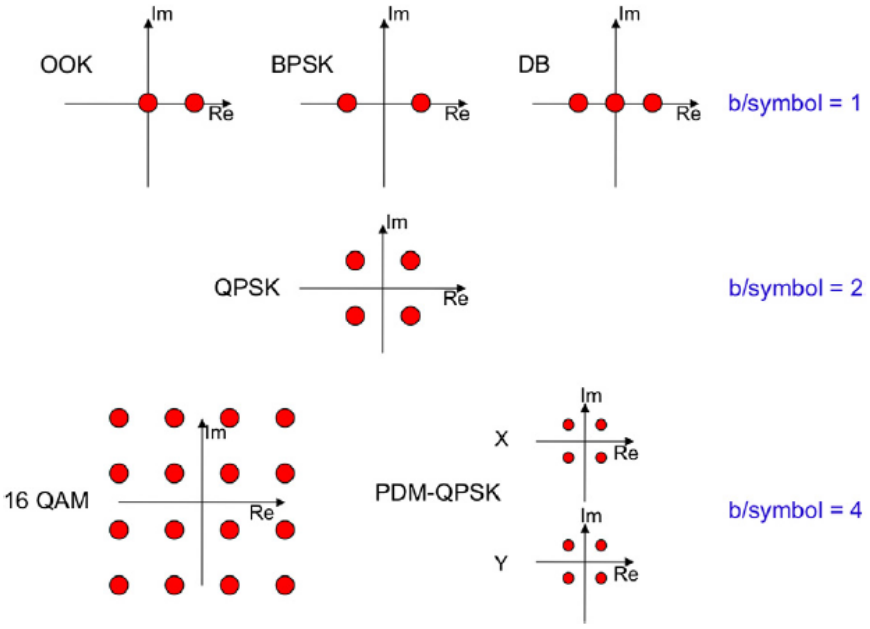

Figure 1.3: Constellation of typical modulation formats. OOK: On-Off keying, BPSK: Binary phase-shift keying, DB: Duobinary, QPSK: Quadrature phase-shift keying, QAM: Quadrature amplitude modulation, PDM: Polarization division multiplexed, from [31].

of a circular core and an annular cladding surrounding the core, with the refractive index of the core being higher than the refractive index of the cladding. This permits the guided transmission of the light wave in the fiber by total internal reflection following a geometrical optics description. Geometrical optics can be used to help understand the the propagation of a light wave in the fiber when the core radius is much larger than the light wavelength, λ. It gives only an approximation to the light propagation process. When the core radius and λ are comparable, it becomes necessary to use the wave-propagation theory for a more accurate description.

In the wave theory light wave transmission in the cable can be described by solving the Maxwell's Equations for electromagnetic waves [46, 47, 34]. A specific solution to the wave equation which satisfies the appropriate boundary conditions of the medium is referred to as an optical mode, and it has the property that its spatial distribution does not change with propagation [46]. In a standard fiber, in the absence of stress which can cause a deviation of the cross-section from circular to elliptical, any mode can exist in two distinct mutually orthogonal polarization states, hence they are referred to as degenerate modes. The number of modes that a fiber can support at a given wavelength is determined by the normalized frequency (V) value which relates to the fiber core radius and refractive index [46, 47, 34].

Fibers with $V < 2.405$ permit a single mode within the wavelength range 1.3–1.6 μm, and are called single mode fibers. They do not suffer from the effect of modal dispersion experienced in multi-mode fibers, and this makes them the most popularly deployed fibers [45].

Dispersion is the broadening of optical pulses that are injected into the fiber. Multi-mode fibers suffer from intermodal dispersion because each mode sees a different refractive index which results in different group velocities for each mode and translates to a broadening of the pulses at the output. This effect is absent in the single mode fiber, however

there are other dispersion effects of the single mode fiber.

1.2.2.1 Chromatic Dispersion

Chromatic dispersion (CD) is an impairment that impacts high data rate transmission in single mode fibers. CD is a static phenomenon because it changes very slowly [48]. It is also wavelength-dependent. CD arises because an optical pulse is made up of different spectral components that travel at slightly different group velocities v_g and do not arrive simultaneously at the fiber output. This leads to pulse spreading at the output referred to as group velocity dispersion (GVD). Hence CD and GVD are synonyms.

A given spectral component of the optical pulse at angular frequency ω traveling in a single mode fiber of length L will arrive at the fiber output after a time delay $\tau_{CD} = L/v_g$. With v_g defined as Eq. (1.2) below [46]

$$v_g = \left(\frac{\mathrm{d}\beta}{\mathrm{d}\omega}\right)^{-1} \tag{1.2}$$

Using $\beta = \overline{n}k_0 = \overline{n}\omega/c$ in Eq. (1.2), we can arrive at $v_g = c/\overline{n}_g$, with $\overline{n}_g$ the group index given by Eq. (1.3)

$$\overline{n}_g = \overline{n} + \omega(\mathrm{d}\overline{n}/\mathrm{d}\omega) \tag{1.3}$$

If the spectral width of the pulse is $\Delta\omega$, the extent of pulse spreading can be given by Eq. (1.4) [46]

$$\Delta\tau_{CD} = \frac{\mathrm{d}\tau_{CD}}{\mathrm{d}\omega}\Delta\omega = \frac{\mathrm{d}}{\mathrm{d}\omega}\left(\frac{L}{v_g}\right)\Delta\omega = L\frac{\mathrm{d}^2\beta}{\mathrm{d}\omega^2}\Delta\omega = L\beta_2\Delta\omega \tag{1.4}$$

The parameter $\beta_2 = \mathrm{d}^2\beta/\mathrm{d}\omega^2$ is referred to as the GVD parameter, and it determines how much an optical pulse would spread during propagation in the fiber [46]. A dispersion parameter, D in units of ps/nm/km can be worked out by considering wavelength instead of the frequency to give Eq. (1.5)

$$D = \frac{\mathrm{d}}{\mathrm{d}\lambda}\left(\frac{1}{v_g}\right) = \frac{-2\pi c}{\lambda^2}\beta_2 \tag{1.5}$$

It can also be written as the sum of two contributions namely material dispersion and waveguide dispersion [46, 40]. Material dispersion arises when different wavelengths in the pulse spectrum travel at different speeds because of the refractive index dependence with wavelength. Waveguide dispersion is caused by the difference in speed between light traveling (faster) in the cladding of lower refractive index than in the core (slower).

The dispersion parameter D varies with wavelength and the wavelength dependence can be seen in Fig. 1.4 for the single mode fiber. Near $\lambda = 1310$ nm we see that $D \approx 0$ ps/nm/km, and near $\lambda = 1550$ nm we see that $D = 17$ ps/nm/km. The wavelength, λ_0 at which $D = 0$ is called the zero-dispersion wavelength. For values of λ below λ_0, $D < 0$ and we have normal dispersion, whereas for values of λ above λ_0, $D > 0$ and we have anomalous dispersion [49, 47]. Careful consideration is required in choosing what wavelength region we wish to transmit in depending on how much dispersion we can either tolerate or compensate.

Optical transmission systems offer some tolerance to dispersion by permitting the spreading to be within some proportion of the symbol period (i.e. the inverse of the baud rate), so long as the BER does not exceed a defined threshold. For example transmission is said to be CD-limited when pulse broadening by CD exceeds 40% of the symbol period. This tolerance can be increased with compensation schemes that equalize or undo the effect of CD.

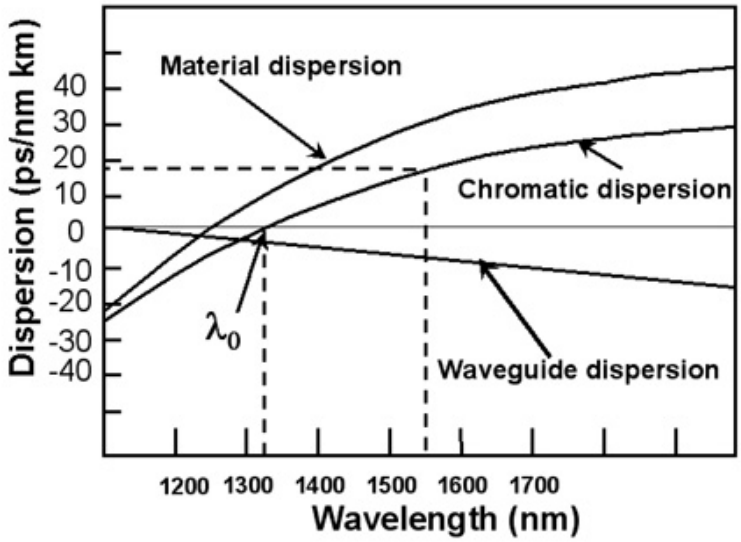

Figure 1.4: Dispersion map of standard single-mode fiber, from [32].

1.2.2.2 Polarization Mode Dispersion

Polarization mode dispersion (PMD) is another impairment that severely impacts high data rate transmission over the optical fiber channel. Unlike CD, it is a stochastic phenomenon or a dynamic impairment that will always be an issue in optical fiber communications due to the inherent imperfections in the fiber manufacturing process and the varying environmental factors at fiber deployment sites [50].

The optical fiber, if perfectly circular cross-section is assumed, as noted earlier permits two degenerate modes, hence has two principal states of polarization (PSP) that are orthogonal to each other. For each of these PSPs there is a corresponding propagation constant say β_x and β_y — assuming the two PSP axes are x and y respectively. Such an ideal fiber will have a uniform refractive index profile all through the cross-section and hence the propagation constant along both PSPs will be the same. In practice, this is not the case as there are small variations in the refractive index profile due to manufacturing imperfections, and also when the fiber is bent or impacted by external stress. The result is that the propagation constant along the orthogonal PSPs will no longer be equal and a pulse that is injected into the fiber, after splitting between both PSPs, will travel at different speeds in each PSP one being faster than the other. The pulse splits between the PSPs because it is not necessarily launched into the fiber at one of the PSPs. From the definition of v_g, it is clear to see that this leads to a fast PSP axis where the refractive index is lower hence the pulse speed is higher, and a slow PSP axis where the refractive index is higher hence the pulse speed is slower. The difference in the refractive indices Δn of the PSPs is referred to as birefringence.

Therefore a pulse injected into the fiber will arrive at the output at slightly different times along the PSPs and will lead to pulse spreading. The difference in the refractive indices, which translates to a difference in the propagation constants $\Delta\beta$, leads to a time difference $\Delta\tau$ between the pulses on either PSPs. This manifests itself as pulse spreading, $\Delta\tau$ referred to as the differential group delay (DGD). Therefore, at the output of the fiber, the final pulse will be spread by an amount equal to $\Delta\tau$ and will arrive with intersymbol interference (ISI) if $\Delta\tau$ is comparable to the pulse width/ symbol period T_s. ISI means that part of a pulse spreads into another pulse leading to an overlapping interfering region. In a polarization division multiplexed (PDM) transmission system the PMD manifests itself

as cross-talk between orthogonal polarization axes [51].

PMD could be referred to as first-order PMD when its consideration does not depend on the frequency of the wave. Second- and higher order PMD are frequency dependent. We will consider first order PMD in this manuscript as we focus on a narrowband signal.

1.2.2.3 Fiber losses

The light wave that propagates in the fiber experiences some loss or attenuation and so the power at the fiber output is reduced compared to the power at the fiber input. This happens due to absorption property of the fiber, defects in the glass, and backscattering among others. [46, 34]. The fiber loss can be quantified by an attenuation coefficient, α in units of km^{-1}. Given the launch power as P_{in} at the input of a fiber of length L, the output power P_{out} is given as:

$$P_{\text{out}} = P_{\text{in}} \exp(-\alpha L) \tag{1.6}$$

The attenuation coefficient is usually expressed in dB/km instead of km^{-1} and the relationship between the two is given as

$$\alpha(\text{dB/km}) = -\frac{10}{L} \log_{10}\left(\frac{P_{\text{out}}}{P_{\text{in}}}\right) = 4.343\alpha \tag{1.7}$$

The attenuation of the fiber can limit the maximum transmission distance without repeaters or amplifiers. Low loss fibers are preferred whenever possible. Fig. 1.5 shows the variation of attenuation coefficient with wavelength. Advancements in fiber design have been able to bring the attenuation down from several dB/km to as low as about 0.15 dB/km for pure silica core fibers. For the single mode fiber, the attenuation is between 0.2 and 0.8 dB/km.

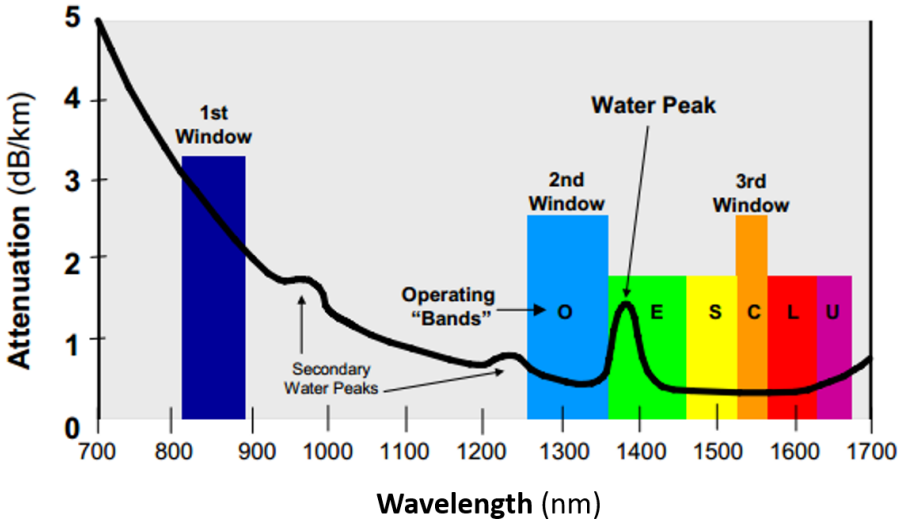

Figure 1.5: Attenuation spectrum of standard single-mode fiber, from [33].

Other sources of loss would involve considering the whole fiber optic communication channel together with lossy components in the transmitter, along the fiber connections, and in the receiver. Hence there is an optical/ power budget for fiber optic communication. The optical budget is the difference between the minimum optical transmitted (launch) power and minimum received optical power (receiver sensitivity), in dB. Fibre

optic communication systems are designed to operate within a specified optical budget. There is also a loss budget which is defined as the difference between the minimum launch power minus an optical path penalty margin and the minimum receiver sensitivity, in dB [52].

1.2.2.4 Fiber nonlinearities

We previously mentioned that fiber optic communication systems are designed to operate within a specified optical budget. One way to improve transmission distance is to increase the optical budget by increasing the launch power. However, the launch power cannot be infinitely increased due to the onset of fiber nonlinearities. The nonlinear effect is a phenomenon where the refractive index of optical fibers change in proportion to the intensity of the electromagnetic field [46, 49, 47].

The nonlinear effects (impairments) lead to interference (intra-channel), for a single channel, and crosstalk (inter-channel), for different WDM channels, when the launch power exceeds a certain threshold. Inter-channel effects affect WDM systems most strongly at low per-channel bit rates of 10 Gbps and below, while intra-channel nonlinearities affect systems most strongly at bit rates above 10 Gbps. This is because signal waveforms evolve very fast along the fiber length and averages out the nonlinearities between bits from the same channel as well as nonlinearities between different channels [53].

The most common nonlinear effects are stimulated Brillouin scattering (SBS), stimulated Raman scattering (SRS), and third-order susceptibility $\chi^{(3)}$ — which is responsible for phenomena such as self-phase modulation (SPM), cross-phase modulation (XPM) and four-wave mixing (FWM). [41, 45].

Stimulated Brillouin Scattering — SBS is an inelastic scattering meaning that the fiber molecules scatter photons in such a way that the frequency after scattering is lower than the frequency before scattering. It occurs in the backward direction only and leads to a frequency shift of about 11 GHz. Hence SBS will not have inter-channel effects in WDM systems with channel spacing larger than 11 GHz. The threshold power at which the effects of SBS become significant is about 5 mW near 1500 nm [41].

Stimulated Raman Scattering — SRS is also an inelastic scattering but unlike SBS it occurs in both the forward and backward directions. It leads to a frequency shift of about 13 THz. The threshold power at which the effects of SRS become significant is about 570 mW near 1550 nm. Since channel powers in optical communication systems are usually below 10 mW, SRS is not a limiting factor for single channel light wave systems. It is however, significant for WDM systems. The amplification gains of SRS could be advantageously manipulated in WDM systems for compensation of fiber losses [41]. Notably, the Raman gain is exploited in Raman amplifiers [45].

Four-wave mixing — Four-wave mixing (FWM) in multi-channel WDM systems is the generation of new frequencies from a combination of the other frequencies present in the system. It is present at all wavelengths at high input powers. However, it is more likely to happen near the zero-dispersion wavelength due to a phase matching condition. At the zero-dispersion wavelength third-order dispersion is present.

Nonlinear Phase Modulation — This could either be self-phase modulation (SPM) which is a phase shift induced by the intensity variations of the transmitted signal itself; or

cross-phase modulation (XPM) which is a phase shift induced by the intensity variations of neighboring channels in a WDM system [40, 45].

Depending on the application requirement fiber nonlinearities can be ignored if the optical transmission system configuration does not augur well for their occurrence. For example, increased launch power not only poses problems of nonlinearity but also problems of eye safety in environments where this could be risky. Also the effects of SRS which start to become significant around +20 dBm launch power and SBS around +17 dBm launch power can be neglected in scenarios where the launch powers do not reach as high as these values.

1.2.2.5 Propagation equation of the fiber optic channel

It is possible to encompasses the relevant effects of the fiber channel in a wave equation. Assuming a single polarization scenario, and by leaving out the absolute phase, we can rewrite Eq. (1.1) as

$$\mathbf{E}(z,t) = \mathbf{x}A(z,t)e^{j(\omega_0 t - \beta_0 z)} \tag{1.8}$$

where $\beta_0 = \omega_o n/c$, and A(z,t) is the amplitude.

If $A(z,t)$ is assumed to be slowly varying in time t and distance z with respect to the exponential term, we can express the wave propagation along the fiber with the nonlinear Schrödinger equation (NLSE) [41]:

$$\frac{\partial A}{\partial z} = -\frac{\alpha}{2}A + j\frac{\beta_2}{2}\frac{\partial^2 A}{\partial t^2} - j\gamma\left|A\right|^2 A \tag{1.9}$$

Considering the right-hand side (RHS) of Eq. (1.9), the first term models the fiber losses; the second term models the GVD; and the third term models the fiber nonlinearity with γ being the Kerr nonlinear coefficient. Eq. (1.9) offers the possibility to numerically investigate the impact of the impairments on an optical pulse in the fiber. It also offers insights to digitally invert the channel to equalize or mitigate the impairments within the confines of some assumptions as we shall see later on.

1.2.2.6 Optical fiber standards in the access network

A majority of deployed optical fiber cables ($> 90\%$) for telecommunications are single mode fibers (SMF) [45]. This is because single mode fibers do not suffer from the intermodal dispersion issue of multimode fibers (MMF). There are various classifications of the SMF as described by industry standardization according to the use case for the SMF. Generally, deployed optical fibers follow the ITU-T recommendations G.650-G659.

The most common SMF is the standard single mode fiber (SSFM) whose optical and mechanical properties are standardized by ITU-T G.652.D recommendations. They can be used in the wavelength range from 1.3 - 1.6 μm and have a low bending loss.

The bend-insensitive fiber (BIF) or bend-resistant fiber (BRF) is the next most popular SMF. It has a lower bending loss than SSMF and meets the recommendations of the ITU-T G.657. Such fibers are suitable for use in FTTH scenarios where fibers could experience tight bends due to the environmental constraints of the deployment site.

MMFs, although susceptible to intermodal dispersion, are however still being used in short-reach transmission applications where the maximum transmission distance does not exceed 2 km. This is because the maximum allowable transmission distance varies inversely as the bandwidth. They are typically used at wavelength range of 850 nm (SSFMs are actually multimode too but are single-mode only in the O-band wavelengths and above).

The most commonly used MMFs are those standardized by ISO/IEC 11801 and TIA-568.3-D. ISO stands for international organization for standards; IEC — international electrotechnical commission; and TIA — telecommunications industry association.

1.2.3 The optical receiver

The optical receiver is the end point of the fiber optic communication system and completes the transmission task by converting the optically transmitted information back to a reliable digitized form.

It typically consists of an optical front end, trans-impedance amplifiers (TIA), analog-to-digital converters (ADC) in case of multi-level received modulation format, and a threshold decision module. The optical front end converts the received modulated optical signal into an electric current. The TIA amplifies this current to a suitable output voltage level, the ADC samples the voltage level to discrete voltage sample values in case multilevel modulation format is received or if further digital signal processing will be required, and the threshold decision module (either an analog threshold e.g. for OOK or a digital threshold in software e.g. for multi-level modulation formats) makes decision on what bits were transmitted.

There are two broad categories of optical receivers; direct detection (DD) receivers for intensity-only modulated signals, and coherent detection receivers (coherent receiver) for joint amplitude and phase modulated signals.

The DD receiver is the simplest type of receiver and its optical front end consists of a single photodiode. The DD receiver requires one TIA, and has no need for ADCs. Instead it utilizes a clock recovery module before the decision module.

The standard coherent detection receiver's optical front end consists of a local oscillator laser, at least one 90° optical hybrid and four photodiodes (or two balanced photodiodes). Afterwards, at least two TIAs and two ADCs. In a dual polarization transmission scenario, the component count is doubled.

Photodiode A photodiode is a semiconductor device that operates in reverse bias mode and converts light to electric current. Its quantum efficiency, η defines the number of charge carrier pairs generated by a number of photons over a given time and is given by Eq. (1.10) [41, 40]

$$\eta = \frac{I/e}{P/hf} \tag{1.10}$$

where I is the photodide output current, e is the constant for elementary charge, P is the photodiode received power, hf is the photon energy with h the Planck constant and f the frequency of the incident light.

The ratio I/P is the responsivity, R, of the photodiode and is given by Eq. (1.11) [40]:

$$R = \frac{I}{P} = \eta\frac{e}{hf} \approx \frac{\eta\lambda(\text{nm})}{1240(\text{nm})} \tag{1.11}$$

The responsivity increases with wavelength until a cutoff wavelength is reached and then it drops rapidly [40]. The output current from a photodiode due to an incident light of power P_{in} is $I = RP_{\text{in}}$.

Photodiodes could either be positive-intrinsic-negative (PIN) photodiodes or avalanche photodiodes (APD). The difference is that the APD has an internal amplification factor M_{APD}: $I_p = M_{\text{APD}}RP_{in}$ while the PIN photodiode does not. This however makes the APD incur excess noise in some situations when compared to the PIN photodiode.

The minimum value of received power that a photodiode can detect to attain a given BER is called the sensitivity of the photodiode. The lower this value is, the better the photodiode since it leads to an increase in the optical budget for a fixed transmit power. The maximum received power that a photodiode can tolerate without saturation is the overload limit of the photodiode.

One way to make up for a poor receiver sensitivity is to use an optical amplifier before the receiver (pre-amplified scheme). In such a scheme the optical amplifier is able to increase the signal-to-noise ratio (SNR) however it also generates amplified spontaneous emission (ASE) noise. In a non-amplified scheme, the receiver components generate both shot noise and thermal noise. Shot noise is related to the random generation of the electron stream that makes up an electric current. It is voltage dependent. Thermal noise is generated in the absence of applied voltage by the random motion of electrons in resistive elements. It is temperature dependent.

Depending on the transmission scenario, either kind of noise can be more significant than the others. In pre-amplified schemes, ASE noise dominates. In non-amplified schemes shot noise dominates in coherent detection, while thermal noise dominates in DD when the transmission losses are large enough to lower the received photocurrent, such that shot noise generated by the small photocurrent is less than the thermal noise. When shot noise dominates, the APD can have a worse SNR than the PIN photodiode because of the excess noise generated inside the APD due to its amplification factor. APD photodiodes are however attractive because of the dominance of thermal noise in practical receivers, where the amplification factor of the APD leads to an improvement in the receiver sensitivity. [46].

1.2.3.1 Direct detection receiver

The DD receiver is suitable for intensity-modulated signals and the transmission system is referred to as intensity modulation and direct detection (IM-DD). The DD receiver is relatively simple and has a cost-effective design. The IM-DD communication system is the fundamental optical communication system and the component count for the DD receiver is the minimum required. Fig. 1.6 gives the schematic of a standard DD receiver.

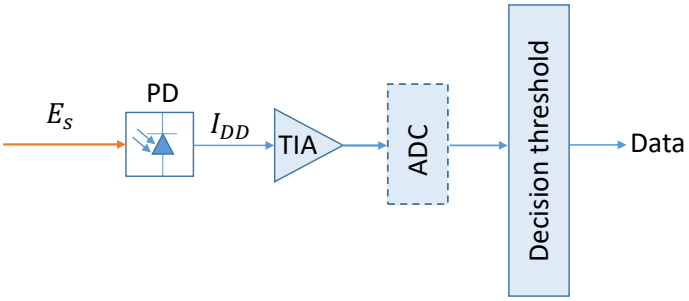

Figure 1.6: Direct detection (DD) receiver. PD: photodiode, TIA: transimpedance amplifier, ADC: analog-to-digital converter (optional).

Assuming the received signal field $E_s(t)$, without any fiber impairments, is defined as:

$$E_s(t) = A_s e^{-j(\omega_s t + \phi_s)} \tag{1.12}$$

then A_s is the signal field amplitude, ω_s is the signal field angular frequency, and ϕ_s is the signal field phase.

At the photodiode , the received optical signal power is converted to an electric output current $I_{DD}(t)$ via the relation $I_{DD}(t) = RP_s(t)$, where R is the responsivity of the photodiode and $P_s(t)$ is received optical signal power into the photodiode; $P_s(t) = K|E_s(t)|^2$, with K a proportionality constant. The output photocurrent can be expressed, dropping the dependence on t, as:

$$I_{DD} = RKA_s^2 = RP_s \tag{1.13}$$

We can see in Eq. (1.13) that the output of the photodiode in DD depends on the square of the received signal field.

1.2.3.2 Coherent detection receiver

The coherent detection (CohD) receiver is suitable for joint amplitude and phase modulated signals. CohD involves recovery of a transmitted message signal by mixing the modulated received signal with a locally generated carrier signal of either the same frequency (homodyne) as or different frequency (heterodyne) from the received signal. Assuming the received signal field of Eq. (1.12), the locally generated carrier (local oscillator) $E_{lo}(t)$ can then be defined as:

$$E_{lo}(t) = A_{lo}e^{-j(\omega_{lo}t+\phi_{lo})} \tag{1.14}$$

where A_{lo}, ω_{lo}, and ϕ_{lo} are defined similarly as in Eq. (1.12) but for the local oscillator.

90° optical hybrid The 90° optical hybrid consists of two couplers that mix the optical signal and the local oscillator signal to realize a phase diversity coherent receiver. The four output ports of the 90° optical hybrid can then be connected to two balanced photodetectors (BPDs) — one BPD for the in-phase I component and the other BPD for the quadrature Q component — each with a pair of photodiodes.

In a polarization and phase diversity coherent receiver, two of such 90° optical hybrids are used — one for each orthogonal polarization tributary. Hence, the requirement of eight photodiodes or four balanced photodiodes. Fig. 1.7 gives the schematic of a standard polarization and phase diverse CohD receiver.

90° optical hybrid output signal derivation The couplers in the 90° optical hybrid have a transfer matrix T given as:

$$T = \frac{1}{\sqrt{2}}\begin{bmatrix} 1 & 1 \\ 1 & -1 \end{bmatrix} \tag{1.15}$$

For input signals $[E_{in1}, E_{in2}]^{\mathrm{T}}$, the output signals from the coupler $[E_{out1}, E_{out2}]^{\mathrm{T}}$ are given by:

$$\begin{bmatrix} E_{out1} \\ E_{out2} \end{bmatrix} = \frac{1}{\sqrt{2}}\begin{bmatrix} 1 & 1 \\ 1 & -1 \end{bmatrix}\begin{bmatrix} E_{in1} \\ E_{in2} \end{bmatrix} \tag{1.16}$$

The coupler has two input arms and two output arms. While the input of the coupler can have either one or two signals present, the output will usually have two signals present. This leads to either of the following combinations at the input $[E_{in1}, E_{in2}]^{\mathrm{T}}$, $[E_{in1}, 0]^{\mathrm{T}}$, or $[0, E_{in2}]^{\mathrm{T}}$, with $(.)^{\mathrm{T}}$ the transpose operation. The corresponding output signals will be $[(1/\sqrt{2})(E_{in1} + E_{in2}),\ (1/\sqrt{2})(E_{in1} - E_{in2})]^{\mathrm{T}}$, $[(1/\sqrt{2})(E_{in1}),\ (1/\sqrt{2})(E_{in1})]^{\mathrm{T}}$, or $[(1/\sqrt{2})(E_{in2}),\ (1/\sqrt{2})(E_{in2})]^{\mathrm{T}}$ respectively.

In the 90° optical hybrid, the input signal to one of the arms before the second (i.e. last) coupling stage is shifted by 90° or $\pi/2$ radians. This is effectively a multiplication by $e^{j\pi/2}$ or j. The four output fields after the second coupling stage, for input signals

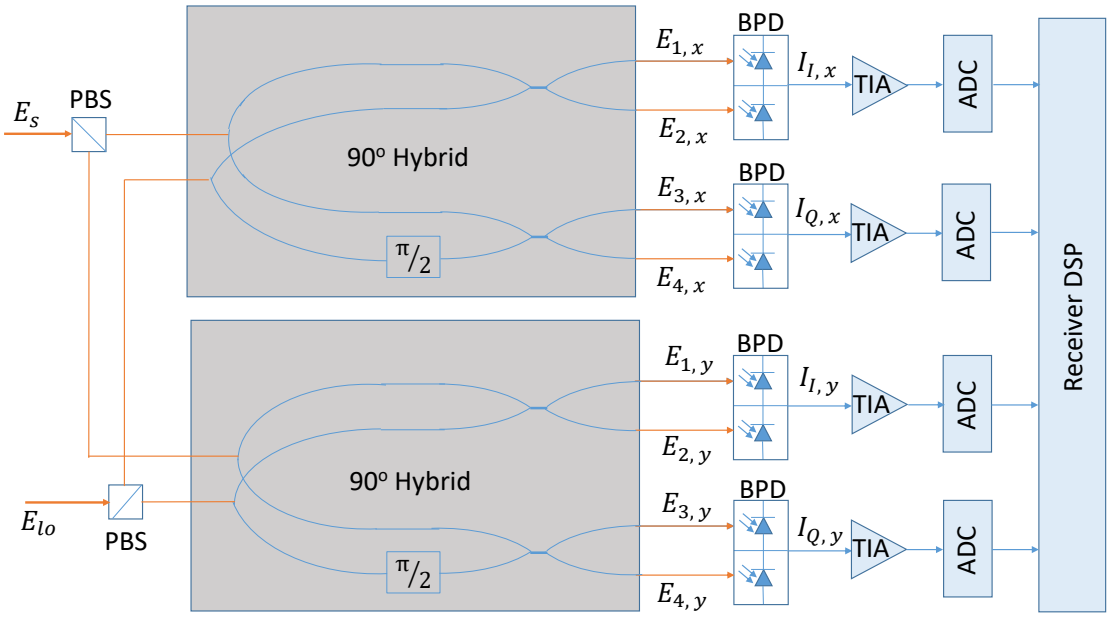

Figure 1.7: Standard polarization and phase diverse CohD receiver. PBS: polarization beam splitter, BPD: balanced photodiode, TIA: transimpedance amplifier, ADC: analog-to-digital converter, x: polarization x tributary, y: polarization y tributary.

$E_s(t)$ and $E_{lo}(t)$ can then be written (for one tributary of a polarization and phase diverse coherent receiver) as:

In-phase components:

$$E_1 = (1/\sqrt{8})[E_s(t) + E_{lo}(t)] \tag{1.17}$$
$$E_2 = (1/\sqrt{8})[E_s(t) - E_{lo}(t)] \tag{1.18}$$

Quadrature components:

$$E_3 = (1/\sqrt{8})[E_s(t) + jE_{lo}(t)] \tag{1.19}$$
$$E_4 = (1/\sqrt{8})[E_s(t) - jE_{lo}(t)] \tag{1.20}$$

Eq. (1.17) – Eq. (1.20) apply to one polarization tributary. Similar sets of equations can be obtained for the second polarization tributary from a second 90° optical hybrid. We would only need to replace E_1 to E_4 with E_5 to E_8.

At the photodiodes, the received optical signal power is converted to an electric output current $I_{PD}(t)$ via the relation $I_{PD}(t) = RP_{in}(t)$, where R is the responsivity of the photodiode and $P_{in}(t)$ is received optical signal power into the photodiode. The power $P(t)$ corresponding to Eq. (1.17) – Eq. (1.20) can generally be written as $P(t) = K|E(t)|^2$, with K a proportionality constant.

Solving specifically for the $P(t)$ for each $E(t)$, and dropping the dependence on t for simplicity of expression, we have,

$$P_1 = K\left|(1/\sqrt{8})(E_s + E_{lo})\right|^2 \tag{1.21}$$
$$= (K/8)[(E_s + E_{lo})(E_s + E_{lo})^*] \tag{1.22}$$
$$= (K/8)[E_sE_s^* + E_sE_{lo}^* + E_{lo}E_s^* + E_{lo}E_{lo}^*] \tag{1.23}$$

Simplifying each term in Eq. (1.23) separately and utilizing Eq. (1.12) and Eq. (1.14),

$$E_s E_s^* = A_s e^{-j(\omega_s t+\phi_s)} A_s e^{j(\omega_s t+\phi_s)} = A_s^2 \tag{1.24}$$
$$E_s E_{lo}^* = A_s e^{-j(\omega_s t+\phi_s)} A_{lo} e^{j(\omega_{lo} t+\phi_{lo})} = A_s A_{lo} e^{-j(\omega_s t-\omega_{lo} t+\phi_s-\phi_{lo})} \tag{1.25}$$
$$E_{lo} E_s^* = A_{lo} e^{-j(\omega_{lo} t+\phi_{lo})} A_s e^{j(\omega_s t+\phi_s)} = A_{lo} A_s e^{j(\omega_s t-\omega_{lo} t+\phi_s-\phi_{lo})} \tag{1.26}$$
$$E_{lo} E_{lo}^* = A_{lo} e^{-j(\omega_{lo} t+\phi_{lo})} A_{lo} e^{j(\omega_{lo} t+\phi_{lo})} = A_{lo}^2 \tag{1.27}$$

Substituting Eq. (1.24) − Eq. (1.27) into Eq. (1.23),

$$P_1 = (K/8)[A_s^2 + A_{lo}^2 + A_s A_{lo}(e^{j(\omega_s t-\omega_{lo} t+\phi_s-\phi_{lo})} + e^{-j(\omega_s t-\omega_{lo} t+\phi_s-\phi_{lo})})] \tag{1.28}$$
$$= (K/8)[A_s^2 + A_{lo}^2 + A_s A_{lo}(2\cos(\omega_s t - \omega_{lo} t + \phi_s - \phi_{lo}))] \tag{1.29}$$
$$= (K/8)[A_s^2 + A_{lo}^2 + 2A_s A_{lo}(\cos([\omega_s - \omega_{lo}]t + \phi_s - \phi_{lo}))] \tag{1.30}$$

Setting $P_s = KA_s^2$, $P_{lo} = KA_{lo}^2$, and $\omega_{IF} = \omega_s - \omega_{lo}$,

$$P_1 = (1/8)[P_s + P_{lo} + 2\sqrt{P_s P_{lo}}\cos(\omega_{IF} t + \phi_s - \phi_{lo})] \tag{1.31}$$

A similar derivation can be made for P_2 which gives,

$$P_2 = (1/8)[P_s + P_{lo} - 2\sqrt{P_s P_{lo}}\cos(\omega_{IF} t + \phi_s - \phi_{lo})] \tag{1.32}$$

We can proceed to derive P_3 and then P_4 can be easily written afterwards.

$$P_3 = K\left|(1/\sqrt{8})(E_s + jE_{lo})\right|^2 \tag{1.33}$$
$$= (K/8)[(E_s + jE_{lo})(E_s + jE_{lo})^*] \tag{1.34}$$
$$= (K/8)[(E_s + jE_{lo})(E_s^* - jE_{lo}^*)] \tag{1.35}$$
$$= (K/8)[E_s E_s^* - jE_s E_{lo}^* + jE_{lo} E_s^* + E_{lo} E_{lo}^*] \tag{1.36}$$

Substituting Eq. (1.24) − Eq. (1.27) into Eq. (1.36),

$$P_3 = (K/8)[A_s^2 + A_{lo}^2 + A_s A_{lo} j(e^{j(\omega_s t-\omega_{lo} t+\phi_s-\phi_{lo})} - e^{-j(\omega_s t-\omega_{lo} t+\phi_s-\phi_{lo})})] \tag{1.37}$$
$$= (K/8)[A_s^2 + A_{lo}^2 - A_s A_{lo}(2\sin(\omega_s t - \omega_{lo} t + \phi_s - \phi_{lo}))] \tag{1.38}$$
$$= (K/8)[A_s^2 + A_{lo}^2 - 2A_s A_{lo}(\sin([\omega_s - \omega_{lo}]t + \phi_s - \phi_{lo}))] \tag{1.39}$$

Setting $P_s = KA_s^2$, $P_{lo} = KA_{lo}^2$, and $\omega_{IF} = \omega_s - \omega_{lo}$,

$$P_3 = (1/8)[P_s + P_{lo} - 2\sqrt{P_s P_{lo}}\sin(\omega_{IF} t + \phi_s - \phi_{lo})] \tag{1.40}$$

A similar derivation can be made for P_4 which gives,

$$P_4 = (1/8)[P_s + P_{lo} + 2\sqrt{P_s P_{lo}}\sin(\omega_{IF} t + \phi_s - \phi_{lo})] \tag{1.41}$$

The P_s i.e. P_1, P_2, P_3, and P_4 onto each photodiode can now be converted to photocurrent I_{PD} at the output of the photodiode respectively as:

$$I_{PD1} = RP_1 = (R/8)[P_s + P_{lo} + 2\sqrt{P_s P_{lo}}\cos(\omega_{IF} t + \phi_s - \phi_{lo})] \tag{1.42}$$
$$I_{PD2} = RP_2 = (R/8)[P_s + P_{lo} - 2\sqrt{P_s P_{lo}}\cos(\omega_{IF} t + \phi_s - \phi_{lo})] \tag{1.43}$$
$$I_{PD3} = RP_3 = (R/8)[P_s + P_{lo} - 2\sqrt{P_s P_{lo}}\sin(\omega_{IF} t + \phi_s - \phi_{lo})] \tag{1.44}$$
$$I_{PD4} = RP_4 = (R/8)[P_s + P_{lo} + 2\sqrt{P_s P_{lo}}\sin(\omega_{IF} t + \phi_s - \phi_{lo})] \tag{1.45}$$

For single-ended detection, only one current component in each quadrature is needed, e.g. I_{PD1} and I_{PD3}. However, in balanced detection the in-phase and quadrature components are given as:

$$I_I = I_{PD1} - I_{PD2} = (R/2)\sqrt{P_s P_{lo}}\cos(\omega_{IF}t + \phi_s - \phi_{lo}) \tag{1.46}$$
$$I_Q = I_{PD4} - I_{PD3} = (R/2)\sqrt{P_s P_{lo}}\sin(\omega_{IF}t + \phi_s - \phi_{lo}) \tag{1.47}$$

For homodyne detection $\omega_{IF} = 0$ and for heterodyne detection $\omega_{IF} \neq 0$. The derivations above apply to a **polarization and phase diverse coherent receiver**.

If only a **phase diverse coherent receiver** is considered, and assuming the local oscillator has exactly the same polarization as the input signal, the output equations change as follows due to the absence of any coupling/ splitting stage before the 90° optical hybrid (such coupling/ splitting is only required before the optical hybrids for polarization diversity):

$$I_{PD1} = RP_1 = (R/4)[P_s + P_{lo} + 2\sqrt{P_s P_{lo}}\cos(\omega_{IF}t + \phi_s - \phi_{lo})] \tag{1.48}$$
$$I_{PD2} = RP_2 = (R/4)[P_s + P_{lo} - 2\sqrt{P_s P_{lo}}\cos(\omega_{IF}t + \phi_s - \phi_{lo})] \tag{1.49}$$
$$I_{PD3} = RP_3 = (R/4)[P_s + P_{lo} - 2\sqrt{P_s P_{lo}}\sin(\omega_{IF}t + \phi_s - \phi_{lo})] \tag{1.50}$$
$$I_{PD4} = RP_4 = (R/4)[P_s + P_{lo} + 2\sqrt{P_s P_{lo}}\sin(\omega_{IF}t + \phi_s - \phi_{lo})] \tag{1.51}$$

For single-ended detection, only one current component in each quadrature is needed, e.g. I_{PD1} and I_{PD3}. However, in balanced detection the in-phase and quadrature components are given as:

$$I_I = I_{PD1} - I_{PD2} = R\sqrt{P_s P_{lo}}\cos(\omega_{IF}t + \phi_s - \phi_{lo}) \tag{1.52}$$
$$I_Q = I_{PD4} - I_{PD3} = R\sqrt{P_s P_{lo}}\sin(\omega_{IF}t + \phi_s - \phi_{lo}) \tag{1.53}$$

It is important to note that the output of the photodiode in CohD is proportional to the received signal field and not the square of the received signal field as in DD. This linearization of the received signal field is advantageous for impairment equalization and/ or mitigation.

1.2.3.3 Comparison of direct detection and coherent detection receivers

We can broadly compare the DD and standard dual-polarization (DP) balanced CohD receivers with table 1.3

Table 1.3: Comparison of DD and standard dual-polarization balanced CohD receivers

Component	DD	CohD
Number of photodiodes	1	8
Number of TIAs	1	4
Number of ADCs	1	4
Number of 90°hybrids	N/A	2
Photocurrent	I_{DD}	$\sqrt{\frac{P_{lo}}{P_s}}I_{DD}$

Table 1.3 gives, at a glance, a high level comparison between standard DD and standard DP balanced CohD receiver. In the component section, the name 'component' does not refer to a specific item. It rather refers to the basis of comparison which, here, is at both the device level and signal field level.

At the device level we can count the number of components (hence interfaces) that would be required for each type of detection. The standard DD has a minimal component requirement. At the signal field level, we can compute the photocurrents of DD and standard DP balanced CohD assuming the same type of photodiodes (i.e. same responsivity). We can see that the photocurrent signal can be increased by a factor of $\sqrt{\frac{P_{lo}}{P_s}}$ in the CohD case compared to DD thanks to the constructive interference with the local oscillator whose power, P_{lo}, can be arbitrarily controlled within the limit of the local oscillator laser capabilities. This inherently can lead to an increase in the sensitivity of the CohD receiver as P_{lo} is usually much greater than P_s.

So far, we have been able to briefly present an overall view of the physical layer of the fiber optic communication (FOC) system. This overview will facilitate understanding of the network architecture of FOC systems.

Earlier on, we mentioned that the PON was the most common network architecture of the optical access due to cost considerations for scalability. We also mentioned that to meet the increasing demand for capacity there have been several evolutions of the PON across a number of generations. With the FOC overview in mind, we are in a better position to describe the PON in detail in the next section.

1.3 Passive optical network (PON)

The PON presents, as we shall soon see, a cost-effective point-to-multipoint (P2MP) architecture for the optical access network (OAN) when compared to other architectures — point-to-point (P2P) and the P2MP active optical network (AON).

Increasing demand for capacity has led to several evolutions of the PON across a number of generations. The evolutions first begin by standardization with ITU-T and IEEE providing the recommendations. Then, the telecommunication industry and academia proceed to research, develop, and potentially commercialize products that meet the specifications in the recommendations (i.e. standards). The purpose of these recommendations is to ensure interoperability.

The various architectures of the OAN are given in Fig. 1.8. The P2P or home-run fiber architecture has fiber cables run from the central office to every customer. It has the advantage of being the simplest architecture in terms of medium access control (MAC) protocol because there is no need for the usually complex management that comes with link sharing. However, it has the great disadvantage of requiring a large number of fibers and transceivers inside the central office. This number scales as the number of end users, and the cost is therefore prohibitive.

The P2MP architecture uses either a power splitter (which could be either active or passive) or a wavelength multiplexer (mux)/ demultiplexer (demux) in the field as a remote node (RN) to distribute broadcast signals or wavelength division multiplexing (WDM) signals respectively to the end users. It is also possible to have a mix of both the power splitter and the wavelength mux/ demux schemes.

The cost effectiveness of the PON can be readily seen, as sharing part of the infrastructure among all users decreases the number of end-to-end (E2E) optical fiber cables, interfaces, and civil works required to connect the users. Moreover it does not use any active device in the RN. Instead it uses a passive splitter, hence greatly curbing the operational/ maintenance cost requirement for the network operator.

The optical distribution network (ODN) is the part of the PON between the optical line termination (OLT) located at the central office, and the optical network unit (ONU). It represents the single-rooted P2MP tree of optical fibers with splitters, combiners, filters

and possibly other passive optical components. A composite ODN consists of two or more passive segments interconnected by active devices with each of the segments being either an optical trunk line or an optical distribution segment. A passive optical distribution segment is a simple ODN itself. Two ODNs with distinct roots can share a common subtree [12].

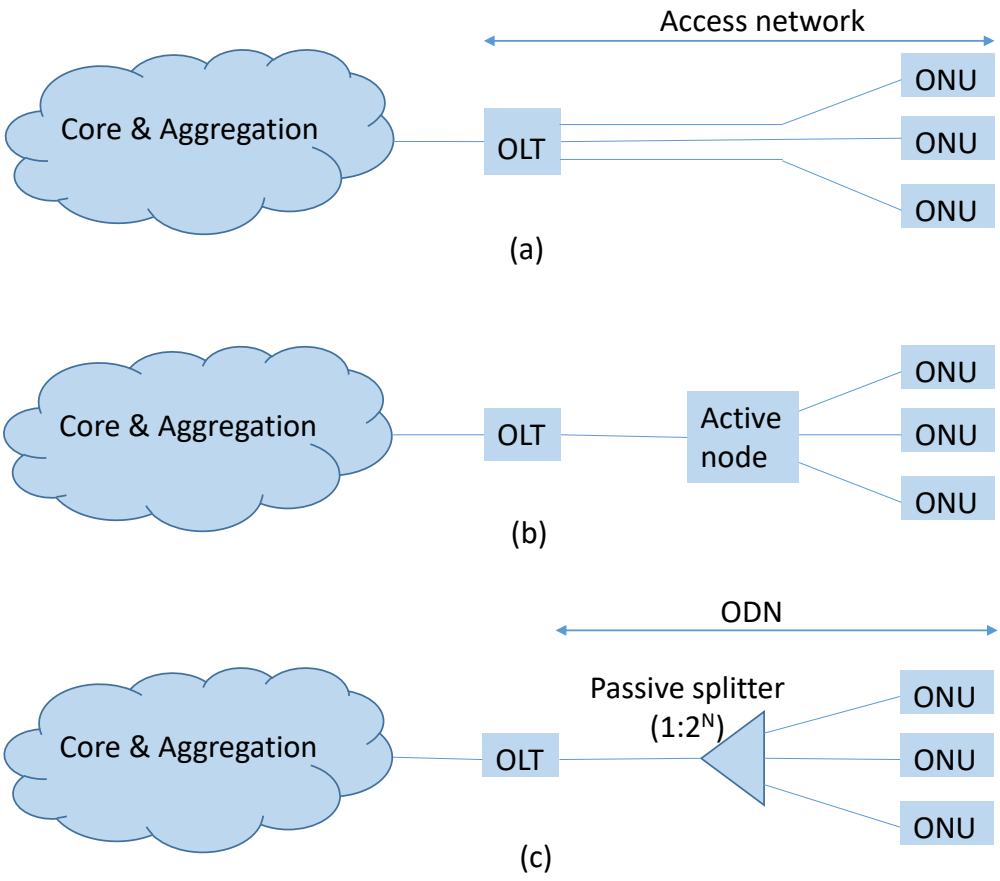

Figure 1.8: Typical architectures of optical fixed access network. (a) Point-to-point (P2P) (b) Point-to-multipoint active optical network (P2MP AON) (c) Point-to-multipoint passive optical network (P2MP PON). OLT: optical line termination, ONU: optical network unit, ODN: optical distribution network.

The OLT is a network element in an ODN-based OAN that terminates the root of at least one ODN and provides an OAN service node interface (SNI).

The ONU is a network element in an ODN-based OAN that terminates a leaf of the ODN and provides an OAN user-network interface (UNI).

Signal transmission from the OLT towards the ONU is referred to as downstream (DS) while signal transmission from ONU towards OLT is referred to as upstream (US). Distinct wavelengths are used for DS and US transmission and they could both be within a wavelength band or in different wavelength bands. The passive splitter in the P2MP PON defines the splitting ratio or fan-out of the ODN. A splitting ratio of 1:2 implies a two-way split and leads to approximately 3.5 dB of attenuation at the output of the splitter. For a higher-order split ratio of $1{:}2^N$ the splitter constitutes an attenuation of about $3.5N$ dB.

There have been various evolutions of the PON according to recommendations that

have been standardized by the ITU-T. There are still some recommendations that are currently under study. The ITU-T study group 15 (SG15), series G.980 - G.989, G.9800 - G.9899, and their relevant G.supplements are the recommendations that concern the OAN. These recommendations are provided below. The first number in brackets indicates the year the recommendation started while the subsequent number[s] indicate[s] the year of amendment to the recommendation.

ITU-T G983.x (1998/2005) Broadband optical access systems based on PON (BPON). The BPON was the first system deployed with a DS/US rate of 662/155 Mbps on a single wavelength in either direction. Time division multiplexing (TDM)-PON. IM-DD

ITU-T G984.1 (2003/2012) Gigabit-capable PON (GPON): DS/US rate of 2.5/1.25 Gbps on a single wavelength in either direction. TDM-PON. IM-DD

ITU-T G987.x (2008/2012/2016) 10-Gigabit-capable PON (XG-PON) systems. DS/US rate of 10/2.5 Gbps on a single wavelength in either direction. TDM-PON. IM-DD

ITU-T G989.x (2013/2013/2015/2023) 40-Gigabit-capable PON (NG-PON2). Utilizes four wavelengths to give a DS/US rate of 10/10 Gbps per λ. Time and wavelength division multiplexing (TWDM)-PON. IM/DD

ITU-T G9807.1 (2016/2017/2023) 10-Gigabit-capable symmetric PON (XGS-PON). symmetric DS/US rate of 10/10 Gbps on a single wavelength in either direction. TDM-PON. IM-DD

ITU-T G9804.1 (2019/2024) Higher speed PON (HS-PON). DS/US rate of 50/25 Gbps on a single wavelength in either direction. TDM-PON. IM-DD with DSP and/or CohD with DSP.

ITU-T G9804.3 (2021/2024) 50-Gigabit-capable PON (50G-PON). 50 Gbps on a single wavelength in either direction. TDM-PON. IM-DD with DSP and/or CohD with DSP.

There are also the recommendations from the IEEE that were evolving in parallel with the ITU-T recommendations;

IEEE 802.3ah (2000) Ethernet PON (EPON). Symmetric DS/US rate of 1/1 Gbps

IEEE 802.3av (2006) 10-Gigabit-capable ethernet PON (10GE-PON). Symmetric DS/US rate of 10/10 Gbps

IEEE 802.3ca (2014) Next generation EPON (NG-EPON). Symmetric DS/US rate of 25/25 Gbps.

These recommendations consider the potential issues envisaged in the next generation PON and are amended as necessary. Some of the issues such as choice of MAC technology (TDM, WDM, TWDM, etc.), co-existence, interoperability, etc. greatly delay the commercialization and deployment of the recommendations. For example the NG-PON2 initially proposed was a WDM-PON and it had the feature of replacing the passive splitter

in the ODN with an arrayed wave-guide grating. This meant that it could not coexist with previous TDM-PON and would require a restructuring of the ODN. Instead a TWDM-PON proposal was put forward with 4 wavelengths, each at 10 Gbps, in each direction. However, NG-PON2 did not see much implementation in the market because XG-PON, which was less expensive, was already in deployment stage at the time. Also in the OAN, the single-wavelength PON standards specify a large linewidth tolerance (a few MHz) [54] for the lasers which allows for low-cost uncooled devices. The use of a multiwavelength system could require a stricter wavelength control, depending on the width of each wavelength channel, hence temperature-controlled lasers which are costly. These factors prevented the commercial success of NG-PON2 [55].

Since NG-PON2 utilizes 10 Gbps line rate channels, the target of beyond 10 Gbps per channel motivated the next steps in PON standardization towards solutions that provide higher bit rates on a single wavelength per direction. This paved the way for the consideration of the introduction of DSP in the PON transceivers [55].

The currently deployed systems permit a coexistence of GPON, XG(S)-PON and 10GE-PON. They are all TDM-PON and based on IM-DD without DSP, and in O-band since the effect of CD is minimal in this wavelength band. With regards to increase in capacity, NG-PON2 was seen a threat in the market and the IEEE 802.3ca project commenced with the intention to counter this threat by proposing to standardize 100GE-PON. There was already a good market for 25 Gbps/λ in the data center ecosystem which utilized four 25 Gbps wavelengths for its 100 Gbps ethernet optical interface to transmit over a single fiber (100GBASE-LR4). However the 100GBASE-LR4 optics cannot be used for PON as PON requires a single fiber whereas LR4 optics utilize two fibers, and the power budget of PON is much higher (approx. 30 dB) due to the presence of a passive splitter. Also 100GE-PON would require a total (DS and US) of eight wavelengths and this would be problematic for the wavelength planning in O-band, while also preventing coexistence with previous PON standards. Hence the ambition of standardizing 100GE-PON was lowered to 50GE-PON (completed in 2020) which required four wavelengths. This led to a final wavelength plan with a DS band (1340 - 1344 nm) and three US bands (1260 - 1280 nm, 1284 - 1288 nm, 1290 - 1310 nm). The wavelength plan accommodates coexistence between 10GE-PON and 50GE-PON. Low-density parity check (LDPC) forward error correction (FEC) codes, powerful transmitters, and improved APD receivers were used to sustain a higher power budget. Evolution of the transceivers and data rates for the PON has closely followed the evolution of the data center market [16, 56, 55].

There was also an interest in a 25 Gbps/λ PON (25G-PON) which was specified by a multisource agreement (MSA) as 25GS-PON in 2021. ITU-T did not provide any recommendations for 25G-PON but, instead in the HS-PON recommendation, targeted achieving a symmetric service rate that would exceed 40 Gbps/λ. To achieve this much higher line rates, ITU-T SG15 had put forward the recommendation, G.supplement 64, for considering PON transmission technologies above 10 Gbps per wavelength. Candidate modulation technologies suggested include non-return-to-zero (NRZ) without DSP in O-band, NRZ with DSP in C-band, or NRZ with duobinary detection; electrical duobinary; optical duobinary; PAM4; and discrete multitone (DMT). Receiver side was assumed to include adaptive equalization with feedforward equalizer (FFE), least mean square (LMS) adaptation algorithm, and decision threshold optimization. The FEC options proposed include Reed-Solomon (RS) code, Bose-Chaudhuri-Hocquenghem (BCH) codes, and LDPC codes.

Considering coexistence and low cost alongside the target symmetric service rate greater than 40 Gbps/λ, 50 Gbps/λ was suggested to meet the capacity requirement. The proposed system would use NRZ on-off keying (OOK) due to the lower loss budget,

irrespective of the higher bandwidth requirement. It also will utilize wavelength and co-existence planning with the use of powerful FEC codes, which are also strong points from the IEEE 802.3ca project. However, different from IEEE 802.3ca project, it assumes the use of DSP to achieve 50 Gbps operation. The final recommendation was standardization of 50G-PON system in 2021.

This 50G-PON is a single wavelength per direction PON and will be the first IM-DD-based PON to introduce DSP. It is usuall for the optical telecommunication industry to strive for the highest possible speed per channel and then utilize WDM to increase the capacity afterwards. This would mean that attention will be given to pushing the capacity of the IM-DD PON beyond 50 Gbps/λ with or without DSP and exploring TWDM PON when the maximum capacity is reached for a single wavelength.

However to scale to even higher capacity, there are not much options for wavelength planning in the already occupied O-band. This leads to consideration of the C-band where the fiber loss is low but the CD is high. Hence more DSP power would be required for equalization. If DSP is not able to compensate for CD beyond the maximum possible service rate to be achieved on a single wavelength in O-band for an IM-DD scheme, then it would also be impossible to compensate CD in C-band while retaining the same IM-DD scheme due to the higher CD in C-band.

One possible option would be to move to C- or L-band and adopt coherent optical transmission (i.e. utilize CohD). In the accesss networks context, CohD has the advantage of easier CD compensation thanks to the linearization that CohD brings, higher sensitivity due to the presence of a local oscillator - therefore higher split ratio can be accomodated, capacity increase due to the availability of multiple degrees of freedom for modulation, and potential of frequency selectivity. However, CohD raises the question about complexity and cost especially for use in PON which has an asymmetric architecture. This has led to a lot of research into low-cost coherent (coherent lite) technologies for the PON.

It is in fact the case in data centers and some of the coherent lite technologies researched for data centers are being proposed for PON. These technologies would require careful evaluation in the application context since the data center architecture is different from the PON architecture.

Since the demand for capacity, among others, is predicted to increase in the future to meet the requirements of new services, we expect to see single channel requirements exceed 100 Gbps (100G-PON) and beyond (i.e. 200G-PON, 400G-PON, etc.).

Noting the difficulties highlighted earlier that IM-DD would have to face for single wavelength transmission, and the potential scalability that CohD offers, it is worth the while to investigate coherent technologies for the future PON. For this reason, in this thesis, we take sides with the use of CohD for 100 Gbps and beyond PON. We will therefore proceed next to review some of the intersting proposals for CohD PON or coherent PON (CPON).

1.3.1 Coherent PON (CPON)

The future PON is expected to support capacities of 100 Gbps/λ and beyond. IM-DD 100 Gbps/λ C-band PON has been demonstrated [57] but it requires a very high launch power of approximately 18 dBm and complex receiver DSP based on machine learning.

The use of coherent technology in PON has been shown to meet the PON power budget requirements for data rates beyond 100 Gbps. It was demonstrated in [58] that, from a power budget perspective, 100- and 200 Gbps/λ systems are feasible using single- or dual-polarization (DP) QPSK modulation. The system could provide additional margins in

excess of 8 dB beyond the 29 dB power budget required by class N1 PON standards.

There a number of challenges that coherent technolgy will have to face when used in PON namely — low target cost, low power consumption, and burst-mode operation in US (and potentially in DS too depending on the application scenario).

To tackle these challenges, researchers are currently working along these directions for CPON: component integration for cost reduction, simplified coherent receivers (coherent lite receivers), new ASIC solutions for power consumption reduction, new DSP algorithms for burst-mode equalization and phase/ clock recovery, or a combination of these. In this thesis, we will focus more on the burst-mode equalization aspect which we shall introduce in the relevant chapter.

The term "coherent lite" was first used in [25] and it is meant to describe an intermediate approach between IM-DD and full coherent system architecture. They sacrifice the performance of full coherent systems to reduce complexity in terms of decreasing amount of optoelectronic components [59, 60] , and the DSP and power consumption requirement [25, 61, 62, 63]

The standard CohD receiver consists of a local oscillator (LO), a polarization beam splitter (PBS), two 90° optical hybrids, four balanced photodiodes (BPD), four transimpedance amplifiers (TIAs) and four ADCs. Its standard mode of detection could either be intradyne (i.e. polarization and phase diverse detection where the local oscillator frequency is close to the signal frequency) or homodyne polarization and phase diverse where the local oscillator is at the same frequency of the signal. If heterodyne detection (i.e. where the local oscillator and the signal frequency leads to an intermediate frequency that is greater than $2\pi f$, with f the signal frequency [38]) is used, it results in a simplification of the receiver components by replacing the 90° optical hybrids with a 3-dB coupler and reducing the numbers of BPDs, TIAs, and ADCs by two [64]. However, the cost to pay is the requirement of larger bandwidth for the components to achieve digital baseband conversion.

Another simplification can come from playing with the polarization. This can be done by utilizing only a single polarization hence getting rid of the PBS at the receiver. The penalty for doing this is 3 dB as we will sacrifice half the system data rate. From the point of view of photonic integration, the PBS is a difficult element to integrate and getting rid of it would allow the total components required come down to a single BPD, one TIA, and one ADC. This however, would lead to the issue of polarization control. The receiver can be made polarization insensitive by utilizing transmitter-side DSP with a coding technique such as Alamouti coding [64]. However, to utilize such coding scheme requires the same dual polarization transmitter as in full CohD and sending redundant information on one polarization tributary, hence a 3-dB loss in potential system data rate. An Alamouti equalizer is required at the receiver side for proper signal detection [65]. Compared to a full coherent system, the Alamouti coherent lite system requires four times more electrical bandwidth to transmit the same bit rate. In comparison to a DD system, the Alamouti coherent lite system is component-wise complex by the presence of the 3-dB coupler, the LO, and one extra photodiode. A further reduced component count Alamouti coherent lite receiver can be achieved with the use of a single photodiode. There are also schemes that propose to get rid of the LO by using a common transceiver laser. Another advantage of this Alamouti scheme is that is is able to utilize one ADC. Considering the power consumption, the DACs and ADCs contribute significantly to the power consumption. Hence techniques that reduce the number of interfaces could offer minimal complexity. There are other schemes that utilize a 3×3 coupler with single ended detection in either symmetric or asymmetric configuration alongside Alamouti coding [66]. However such schemes utilize 3 ADC interfaces in the symmetric configuration and 2 ADC interfaces

in the asymmetric configuration, with the symmetric configuration outperforming the asymmetric.

In a self-homodyne architecture [25, 67], the transmitter laser is split and propagated on a separate fiber and then used at the receiver as a local oscillator. Such a scheme has been mostly developed with the target towards datacenters. The use of such a scheme in PON will not be so efficient as the gain from the presence of an LO will be inhibited as the LO also needs to pass through the passive splitter.

There are also other schemes for coherent detection of IM-DD transmitted signals with the use of a Kramers-Kronig (KK) coherent receiver [60]. The KK receiver is actually a direct detection receiver that can digitally reconstruct the phase information for coherent detection from intensity measurement. Its drawbacks are that: it does not make use of a local oscillator which means there is no amplification and has a limit on the sensitivity; it requires a strong unmodulated carrier which impacts the power efficiency; the signal processing to recover the phase information requires a sample rate that is doubled and narrow optical filters are required. While KK receivers allow simpler receiver architectures and CD compensation, their power consumption is similar to DSP-based coherent recevier [20].

Considering the DSP, to get closer to the IM-DD would require DSP-free coherent lite techniques. A number of these schemes have been demonstrated such as [25, 61, 62, 63]. These DSP-free techniques make use of analog signal processing eliminating the need for DACs and ADCs as in [25] and avoiding further receiver DSP post compensation by imposing strict requirements on the optical components such as perfectly matched coherent lite receivers and sufficient electronic bandwidth availability. Such schemes will not be robust in dynamic channel environments but will be better suited for stable environments such as data centers. However, considering that PON is a short reach network with less CD impact compared to long-haul networks, the DSP for CD equalization in PON will not be as complex as that in the core networks. Hence lower complexity DSP algorithms can be envisaged. In [24] they propose hardware efficient signal processing technologies for CPON. They introduce two types of adaptive equalization (AEQ); the first proposal sacrifices DGD compensation based on the assumption that in the PON system the DGD is sufficiently small compared to the symbol period. Hence they use a 1-tap butterfly filter for polarization demultiplexing neglecting DGD compensation. The second proposal sacrifices some CD compensation while providing DGD compensation. They use 5-tap butterfly filter to compensate for DGD and then 18-tap filter for CD compensation. They demonstrate a DP-QPSK 100 Gbps/λ 80 km system for downstream and achieve downstream loss budgets of 40.7 dB and 39.5 dB with OLT output of 7 dBm for simplified AEQ without and with DGD compensation respectively.

As stated earlier, a common issue for of all next generation OANs utilizing DSP is burst-mode operation. The DSP algorithms will have to be compatible with burst-mode operation [26, 55, 68] in the upstream, and in the downstream — to be used as a new capability based on the use case analysis. Different ONUs at different distances from the OLT would communicate at different instants of time. The emitters at the ONUs switch off between bursts, as opposed to conventional P2P links where the transceivers emit continuously. The burst-mode receiver must therefore handle incoming bursts within a short time interval without losing packets of information.

A notable digital signal processing block that will need to adapt to burst-mode operation is the equalization block. The equalizer would have to estimate the channel and then equalize the received signals in as short a time as possible to meet up with the latency requirements of the application/ use case. This would require equalizers with fast convergence. If the equalizer is robust enough and has sufficiently fast convergence, then it can

be employed in multiple application scenarios where AEQ DSP is required, almost as a one-size-fit all solution.

In this thesis we will focus on investigating such robust equalizers, optimizing them and analysing their performance for potential use in the future OAN. The next subsection presents some of the envisaged future OAN use cases where such robust equalizers, required for CPON, would be needed.

1.3.2 Use cases for future OANs — next generation PONs

The advantageous prospects of CPON facilitate a number of use cases for the next generation PONs including, but not limited to: industrial services including control of devices/ systems such as process automation and factory automation, intelligent transport systems/ train control [69, 14] (requiring low latency), mobile front-haul or back-haul [13, 70, 31] (requiring low latency and high bandwidth), intra-plant and inter-plant networks (requiring high bandwidth and low latency), cloud virtual reality (requiring high bandwidth, low latency, low jitter, and low packet loss).

The architecture and technology to be utilized in each use case will depend on the requirements as each option has some tradeoffs. Taking mobile front-haul and back-haul for example, the system architecture broadly consist of remote radio units (RRUs) and baseband units (BBU). The front-haul consists of network elements between the RRU and BBU, while the back-haul consists of network elements between the BBU and the core network. In 5G, the RRU and BBU are evolved into three units — centralized unit (CU), distributed unit (DU), and active antenna unit (AAU). This leads to new definitions of front-haul as network elements connecting AAUs and DUs, a new mid-haul connecting DUs and CUs, and back-haul connecting CUs to the core network [31]. An architectural tradeoff exists to balance the E2E requirements of throughput and signal processing complexity. This tradeoff exist as functional split options with up to 8 split options between back-haul and front-haul [31]. The number of network components in each segment, depending on the functional split option, determines the amount and nature of processing, hence latency, that can be tolerated. The rate of convergence and complexity of equalization algorithms would determine what functional split options they would be best suited for. The system could also benefit from passive WDM architecture (WDM-PON) where each RRU/ AAU at different transmiting wavelengths connect to a common fiber through multiplexers with the DU as the OLT and the AAU as the ONU.

Generally, selecting a suitable architecture for a given use case is a multifaceted domain that requires compromise. However, as PON inherently has an asymmetric architecture it is quite natural that more expensive and complex solutions be proposed for the OLT and less expensive solutions should be proposed for the ONU.

Focusing on a most common aspect related to the DSP (burst mode operation) and then autonomous operation, we would attempt to fill in the gaps in equalization algorithms related to these in chapters 2 and 3.

First attempt is to come up, in section 2.4 with an equalizer, utilizing the correlation based algorithm, with access points to the channel related parameters.

Secondly, in section 2.5.1, we evaluate the performance of this equalizer to varying channel conditions typical of the OAN.

Next we go further, in section 3.2, to enhance the operation of the equalizer by allowing it to self-adapt beyond its original capabilities. Since these contributions are receiver-side-DSP-related, we therefore introduce, in the next section, the common receiver-side DSP operations utilized for fiber optic communications — some of which could also be done at the transmitter-side.

1.4 State-of-the-art of DSP for fiber optic communications

The use of DSP in FOCs has been an enabler for high-speed optical fiber communication. DSP permits a larger tolerance to impairments due to its capability to digitally equalize and mitigate the effects of the impairments in a robust, flexible, and adaptive way.

DSP operations are performed on samples of the received signal after the analog-to-digital (AD) conversion. It is usual to have the digitized signal at two samples per symbol. In this case, the digitized signal is said to be oversampled and the oversampling ratio is two. The advancement in high-speed CMOS ADCs permit digital sampling of high data-rate signals. The integration of these ADCs with DSP in a single application-specific integrated circuit (ASIC) led to a great revolution in the design of optical transceivers.

DSP can be utilized in high-capacity DD systems and more traditionally in CohD systems.

The DSP operations can be broadly categorized into equalization and synchronization. The received signal is usually equalized before it is synchronized. Equalization involves undoing the effect of the channel on the transmitted signal. Synchronization involves correcting for the differences between the clock frequency at the transmitter and the receiver. Synchronization is necessary because the transmitter and receiver clocks are independent as they are usually far away from each other, hence not necessarily synchronized.

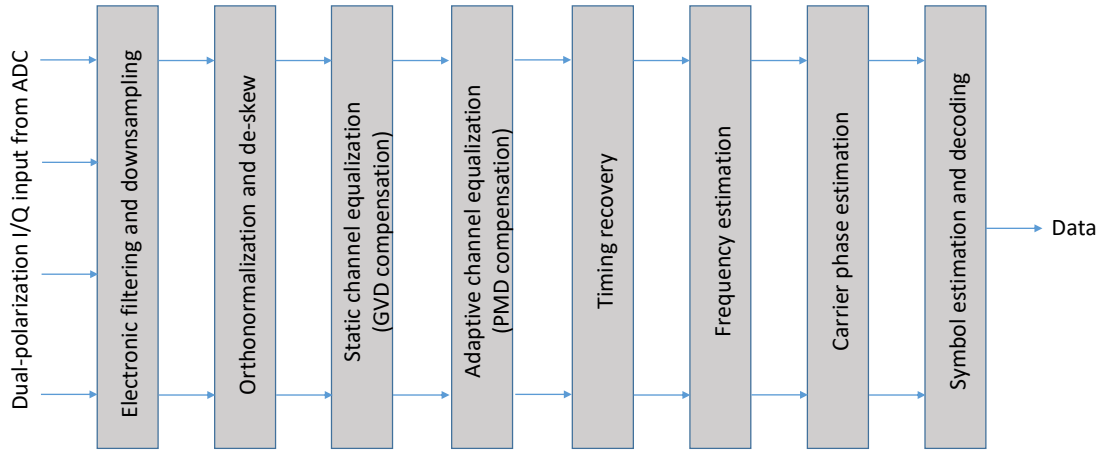

Figure 1.9: Typical CohD receiver DSP chain. I/Q: In-phase/Quadrature, ADC: analog-to-digital-converter, GVD: group velocity dispersion, PMD: polarization mode dispersion.

Fig. 1.9 shows the typical DSP stages in a CohD receiver. We will describe the stages, pertinent to the work done hereafter, in the subsections that follow below.

1.4.1 Orthonormalization and de-skew algorithms

Imperfections in the optical front end of a CohD receiver could be in the form of in-phase-quadrature (I-Q) skew due to imperfectly matched optical path lengths and optical hybrid imbalance (i.e. optical hybrids not exactly 90°). The de-skew algorithm compensates for the path length mismatch, while the orthonormalization algorithm compensates for the optical hybrid imbalance.

The I-Q skew can be compensated by cross-correlating the signals [39] and by interpolation [71].

The optical hybrid imbalance can be compensated by orthornomalization algorithms. Two of such algorithms are the Gram-Schmidt orthogonalization algorithm and the Löwdin orthogonalization algorithm [39, 45]. The basic concept of the orthogonalization algorithms is to align non-orthogonal vectors in a vector space to orthogonal directions (i.e. creating new basis for the vector space). When the new basis vectors have been obtained, their normalization results in an orthonormal basis.

1.4.2 Chromatic dispersion compensation

In section 1.2.2.5 we mentioned that the NLSE of Eq. (1.9) provides insights to digitally invert the fiber channel to equalize or mitigate the impairments within the confines of some assumptions. It is important to state that equalization means that we can completely undo the effect of the channel, while mitigation means that we can not completely undo the effect of the channel but significantly decrease it.

Numerically solving Eq. (1.9) can be made easier if the linear and non-linear parts are considered separately. This is the split-step method [49]. Since attenuation is related to the signal power, it can be compensated by amplification but this also leads to ASE noise and other non-linear impairments. Assuming an unamplified scheme and no non-linear impairments, we can easily solve, in frequency domain, a reduced form of Eq. (1.9) that models only the GVD.

$$\frac{\partial A(z,t)}{\partial z} = j\frac{\beta_2}{2}\frac{\partial^2 A(z,t)}{\partial t^2} \tag{1.54}$$

Solving Eq. (1.54) in frequency domain results in Eq. (1.55)

$$A(z,t) = A(0,t)\exp\left(-j\frac{\beta_2}{2}\omega^2 z\right) \tag{1.55}$$

where $A(z,t)$ is the signal field at the end of the fiber of length z, and $A(0,t)$ is the undistorted signal field at the beginning of the fiber. Eq. (1.55) shows that the effect of GVD on an input field is a phase shift, in frequency domain, of value $G(z,\omega)$ as in Eq. (1.56)

$$G(z,\omega) = \exp\left(-j\frac{\beta_2}{2}\omega^2 z\right) \tag{1.56}$$

Hence a GVD compensating filter, $G^{-1}(z,\omega)$, Eq. (1.57), can be designed in the frequency domain by inverting the sign of β_2. The overlap-and-save (OVS) [72, 73, 74, 75] algorithm can be used, in the frequency domain, for GVD equalization. In this OVS scheme, the time domain received oversampled signal is grouped according to blocks and then the fast Fourier transform (FFT) is applied to convert the oversampled signal into the frequency domain. This frequency domain oversampled signal is then multiplied by $G^{-1}(z,\omega)$ and then the result is converted back to time domain via the inverse fast Fourier transform (IFFT) operation.

$$G^{-1}(z,\omega) = \exp\left(j\frac{\beta_2}{2}\omega^2 z\right) \tag{1.57}$$

The compensating filter $G^{-1}(z,\omega)$, can also be approximated using a finite impulse response (FIR) filter in time-domain. The first step towards deriving the FIR filter is to obtain the time domain expression of $G^{-1}(z,\omega)$ which is given by Eq. (1.58)

$$g^{-1}(z,t) = \sqrt{\frac{c}{jD\lambda^2 z}}\exp\left(j\frac{t^2}{2\beta_2 z}\right) = \sqrt{\frac{c}{jD\lambda^2 z}}\exp\left(j\frac{\pi c t^2}{D\lambda^2 z}\right) \tag{1.58}$$

Eq. (1.58) is the impulse response of $g^{-1}(z,t)$ and is of infinite duration. It can be truncated to obtain an FIR which can be implemented digitally. The tap weights of the truncated impulse response is given as Eq. (1.59) [76]

$$h(n) = \sqrt{\frac{ct^2}{jD\lambda^2 z}} \exp\left(-j\frac{\pi ct^2}{D\lambda^2 z}n^2\right) \tag{1.59}$$

with $-\left\lfloor \frac{N}{2} \right\rfloor \leq n \leq \left\lfloor \frac{N}{2} \right\rfloor$ and $N = 2 \times \left\lfloor \frac{|D|\lambda^2 z}{2ct^2} \right\rfloor + 1$ where n is the sample index. The number of taps N of the FIR filter should span the extent of pulse spreading $\Delta\tau_{CD}$ due to CD. The number of symbols over which the CD spreads a pulse, i.e. the amount of time spreading $\Delta\tau_{CD}$ of CD per symbol duration is given by Eq. (1.60) [45]:

$$\frac{\Delta\tau_{CD}}{T_s} = 2\pi \left|\beta_2\right| k R_s^2 L \times 10^{-6} \tag{1.60}$$

where $|\beta_2|$ is the CD coefficient in ps^2/km, k is a coefficient that depends on the modulation format and is defined as a ratio between the spectral width of the modulated signal and the symbol rate, R_s is the symbol rate in GBaud, L is the length in km.

1.4.3 PMD compensation

Insight to the compensation of PMD first begins with modelling of the PMD impairment. The PMD impairment of the optical fiber can be modelled as a series of short concatenated birefringent sections, and the DGD in each section varies randomly and can assume any value at any instant of time.

We can represent each birefringent section as a 2×2 Jones matrix which is a product of individual matrices namely: a rotation matrix $\mathbf{R}(\theta)$, a diagonal birefringent phase shift matrix $\mathbf{B}(\phi)$, and a diagonal DGD matrix, $\mathbf{DGD}(\Delta\tau, \omega)$ [45]. More details about the form of these matrices will be provided in the next chapter.

The mean value of the DGD, $\Delta\tau$, is referred to as the PMD,$\langle\Delta\tau\rangle$, and PMD is also a random variable for different fibers. Fibers are usually characterized by their PMD coefficient, in units of ps/$\sqrt{\text{km}}$, which is also a random variable for different fibers. Sometimes the PMD is talked about loosely in terms of the PMD coefficient in units of ps/$\sqrt{\text{km}}$ but care must be taken to understand the interpretation provided. The DGD of the optical fiber has been shown to follow a Maxwellian probability density function given by Eq. (1.61) [50, 45]

$$f(\Delta\tau) = \frac{32}{\pi^2}\frac{\Delta\tau^2}{\langle\Delta\tau\rangle^3} \exp\left(\frac{-4\Delta\tau^2}{\pi\langle\Delta\tau\rangle^2}\right) \tag{1.61}$$

In uncompensated systems, the usual design rule for optical fibers is that the maximum DGD, $\Delta\tau_{max}$ should not exceed 30% of the symbol period T_B, and the PMD should be 1/3 of $\Delta\tau_{max}$. This leads to the condition that the PMD should be less than 10% of the symbol period, T_B. This is a tolerance limit for reliable transmission without PMD compensation. Higher tolerance limits can be permitted with PMD compensation strategies for example through the use of DSP as we shall soon see.

The probability that the DGD of a link will exceed $\Delta\tau$ is given by the outage probability $F_c(\Delta\tau)$ as in Eq. (1.62):

$$F_C(\Delta\tau) = \frac{4}{\pi}\frac{\Delta\tau}{\langle\Delta\tau\rangle} \exp\left(\frac{-4}{\pi}\left(\frac{\Delta\tau}{\langle\Delta\tau\rangle}\right)^2\right) + \text{erfc}\left(\frac{2\Delta\tau}{\pi\langle\Delta\tau\rangle}\right) \tag{1.62}$$

To get the amount of time spreading per symbol duration, i.e. the number of symbols over which the average DGD spreads a pulse we can use Eq. (1.63) below [45]:

$$\frac{\langle \Delta\tau \rangle}{T_s} = \text{PMD}_{\text{coeff}} \sqrt{L} R_s \times 10^{-3} \tag{1.63}$$

where T_s is the symbol period, $\text{PMD}_{\text{coeff}}$ is the PMD coefficient in $\text{ps}/\sqrt{\text{km}}$ and can be found in the data sheet of the fiber, R_s is the symbol rate in GBaud, L is the length in km.

If we know the maximum amount of DGD expected, we can compute the number of taps, N, of an equalizer necessary to compensate for the DGD. To correct a DGD of $\Delta\tau$, the temporal span $(N-1)T_s$, of the equalizer (fractionally-spaced) with N taps has to be greater than $\Delta\tau$ i.e. $N - 1 \geq \left\lceil \frac{\Delta\tau}{T_s} \right\rceil$. For example, given a 100 Gbps 31.25 GBaud DP-QPSK system, the symbol period T is 32 ps (i.e. $T = 1/31.25$ GBaud) and the sample period $T_s = \text{T}/2 = 16$ ps. If we want to compensate $\Delta\tau$ of 192 ps, we would require $N = \left\lceil \frac{192}{16} \right\rceil + 1 = 13$ taps.

Since PMD, due to its stochastic nature, is a dynamic impairment, its equalization requires the use of an adaptive equalizer than can adapt its filter taps (coefficients) according to the channel variability. A common way to design such an adaptive equalizer is to use the gradient descent optimization technique.

The gradient descent schemes perform adaptation by iteratively computing the error from a cost function, and then driving this error down to zero. The cost function is defined to suit the requirement of the application scenario and its value, which is the error, should be zero for an ideal case. Variability in the channel conditions will make the error have non-zero values at different times. However, we would like the errors observed over a given time duration to get closer to zero. This means that the equalizer will have to adapt its taps to make this possible. Hence an error gradient can be computed based on the derivative of the cost function with respect to the tap weights of the equalizer. The value of the error gradient can then be used in the computation of new filter taps that should be closer to the optimal filter taps. This computation is performed iteratively until the error gradient approaches zero (i.e. convergence). At this point, we expect to have the optimal filter taps.

The typical equalizer filter update equation for a gradient descent scheme is given by Eq. (1.64).

$$\mathbf{f}(k+1) = \mathbf{f}(k) - \mu \frac{\partial \text{ Cost function}}{\partial \mathbf{f}(k)} \tag{1.64}$$

The new filter value $\mathbf{f}(k+1)$ is computed from the old value $\mathbf{f}(k)$ based on the error gradient (i.e. cost function derivative). This error gradient can either be positive or negative. For a negative gradient, the new value of the filter should be higher than the previous value, while for a positive gradient, the new value of the filter should be lower than the previous value. The increment is in a direction opposite to the error gradient.

The speed at which we can approach the optimal filter taps (i.e. speed of convergence) is determined by a step-size parameter, μ. The smaller the step-size, the slower the convergence, and vice-versa. However, with a small μ we can reach the global minimum more efficiently than with a large μ which might miss it due to the large jumps. There are also schemes that make this step size have a variability for efficient performance [77].

The value of the cost function (i.e. error) could either be computed from the received signals directly (blind), from decisions made on the received signals (decision-directed), or from known transmitted signals (data-aided). These lead to different kinds of equalizer implementation strategies and the choice of either strategy will depend on a number

of factors. For example, in a decision-directed approach, decision needs to be made on the received signals. This constitutes additional steps in terms of operational complexity compared to the blind approach. Although the convergence speed would could be faster. In a data-aided scheme we would require known transmitted symbols referred to as *pilots* which would constitute an overhead for the data transmission.

1.4.4 Carrier recovery

Carrier recovery involves the retrieval of the frequency and phase changes of the optical carrier. In a CohD system, frequency and phase changes of the carrier distort the original signal phase information. It is therefore necessary to estimate these changes and eliminate them. This can be done by carrier frequency offset (CFO) estimation and carrier phase estimation (CPE).

1.4.4.1 Carrier frequency offset compensation

The frequency of the transmitted signal and the local oscillator in a CohD system can drift considerably due to temperature effects. This will lead to frequency fluctuations between transmitted symbols. Since the frequency of the carrier is usually much higher than the signal modulation frequency, it is possible to track the change in carrier frequency by examining the rate of phase change between adjacent symbols. A number of ways to achieve this include the use of the Viterbi-Viterbi algorithm [78], and block-wise frequency domain algorithm [79].

1.4.4.2 Carrier phase estimation

The spontaneous emission process that occurs in lasers lead to random fluctuations of the carrier phase. The frequency of these phase fluctuations is usually much slower than the signal modulation frequency. Hence we cannot track the phase fluctuations in the same way as the frequency offset, from symbol to symbol. It is therefore preferable to perform CPE after CFO compensation. A number of ways to perform CPE exist [78, 80, 81, 82] particularly noting the Viterbi-Viterbi algorithm [78] mostly for constant modulus modulation formats, and blind phase search (BPS) algorithm [81] for higher order modulation formats. More information about CPE and a subtlety of the Viterbi-Viterbi algorithm for QPSK format is described in Appendix B.

At this point, we have briefly discussed the typical DSP receiver operations for impairment equalization and mitigation in a CohD receiver. We will however go into more details on PMD compensation using an adaptive equalizer suitable for constant modulus modulation formats — constant modulus algorithm (CMA). We focus on CMA because of its robustness in dynamic and potentially unknown channel conditions. It is also necessary to understand the operation of the CMA to follow the modifications that will be proposed in later chapters. We therefore introduce the CMA next.

1.5 Constant Modulus Algorithm (CMA) Equalizer

In multi-user wireless transmission systems, the Constant Modulus Algorithm (CMA) equalizer as proposed by [83] has been traditionally utilized at the receiver for equalization, to mitigate the effects of inter-symbol interference (ISI) and cross-talk due the multi-path nature of the wireless channel. This multi-user transmission scenario together

with the multi-path characteristic of the wireless channel necessitate that the equalizer be a multiple-input multiple-output (MIMO) equalizer. The nomenclature of the CMA equalizer also implies that it is best suited for signals with a constant modulus, e.g. phase modulated signals such as binary phase shift-keying (BPSK) and quadrature phase shift-keying (QPSK) formats.

In a dual polarization (DP) coherent optical transmission scenario, the CMA equalizer is also applicable at the receiver. This is because the optical communication channel, just like the wireless channel, has characteristics of multi-path, ISI, and cross-talk. For the optical channel, the orthogonal polarization axes correspond to the multi-user and multi-path case where each polarization axis can be utilized by users and represents one possible path of communication among two paths; the cross-talk and ISI due to multi-path correspond to the polarization cross-talk and ISI induced by the birefringence of the fiber optic channel leading to polarization mode dispersion (PMD) — an impairment that limits the transmission capacity of high speed fiber optic communication systems. In this wired optical context, the CMA equalizer performs two roles while compensating for PMD — polarization demultiplexing to retrieve two orthogonal polarization signals at the output thereby mitigating the polarization cross-talk, and then compensation of the PMD-induced ISI.

The CMA equalizer has been utilized for equalization of BPSK modulated signals [84] and has been shown to work well even for higher order modulation formats such as quadrature amplitude modulation (QAM) [85].

It is a blind adaptive equalizer meaning that it does not require knowledge of the value of the input signal, and it updates its filters' coefficients (or taps) with gradient descent algorithms that iteratively improve the estimate of the filter coefficients by feedback of error signals.

The constant modulus nature of the algorithm implies that the cost function aims at minimizing the expectation of the deviation of the squared modulus of the equalizer output signal from unity. Details of the operation of the CMA equalizer will be described next.

1.5.1 CMA Equalizer Principle

The CMA equalizer, as stated previously, is a blind adaptive equalizer, digitally designed (i.e. the signals and functions related to the equalizer design are sampled, hence they are discretized) and that updates the coefficients of its filters iteratively through gradient descent algorithms (see section 1.4.3). The filters have a finite impulse response (FIR) and the equalizer structure, as shown in Fig. 1.10, is defined by a butterfly arrangement of the filters, $\mathbf{f}_{pq}$, with $p, q \in \{1, 2\}$. The set, $\{1, 2\}$, denotes the two orthogonal polarization tributaries. The notation $\mathbf{f}_{pq}$ describes the equalizer filter that equalizes the multi-path channel with signal going to output polarization p from input polarization q. This leads to four possible filters corresponding to four possible multi-path channels resulting from the polarization mixing combinations.

At a given iteration time index k, we can represent the fractionally-spaced (FS) equalizer (FSE) input signals for the two input polarization tributaries of the equalizer with vectors $\mathbf{y}_1$ and $\mathbf{y}_2$; and the symbol-spaced (T-spaced) equalizer output signals for the two output polarization tributaries of the equalizer with vectors $\mathbf{z}_1(k)$ and $\mathbf{z}_2(k)$. The equalizer output, $\mathbf{z}_p(k)$, is then given by Eq. (1.65), with m, the oversampling ratio, and L the length of the FS $\mathbf{f}_{pq}$.

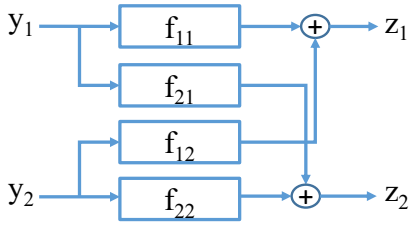

Figure 1.10: CMA butterfly equalizer structure

$$\mathbf{z}_p(k) = \sum_{q=1}^{2} \sum_{l=1}^{L} \mathbf{f}_{pq}^{(k)}(l)\mathbf{y}_q(m(k-1)+l) \tag{1.65}$$

At the output of the equalizer, $\mathbf{z}_p(k)$ is symbol-spaced (T-spaced) — meaning the oversampling ratio is one — and so the time index, k, corresponds to the symbol index. The time index, k, in $\mathbf{f}_{pq}^{(k)}$ indicates that the filter coefficients are updated and attain a new value at each iteration time, while for $\mathbf{z}_p(k)$ it indicates the current estimated value of the received symbol $\mathbf{y}_q(k)$ at that time instant. This is convenient since the equalizer output is symbol-spaced hence k can be both the iteration index and the symbol index. Then packing everything in matrix form, denoting $n = m(k-1)$, we can write at time index k,

$$\mathbf{Z}(k) = \mathbf{F^T}^{(k)}\mathbf{Y}(n) \tag{1.66}$$

Where $\mathbf{Z}(k) = [\mathbf{z}_1(k), \mathbf{z}_2(k)]^{\mathrm{T}}$, $\mathbf{Y^T}(n) = [\mathbf{y}_1(n+1), \mathbf{y}_1(n+2), \cdots, \mathbf{y}_1(n+L), \mathbf{y}_2(n+1), \mathbf{y}_2(n+2), \cdots, \mathbf{y}_2(n+L)]$, and the complex conjugate $\overline{\mathbf{Z}}(k) = \overline{\mathbf{F^T}}^{(\mathbf{k})}\overline{\mathbf{Y}}(n)$. Note that $\mathbf{F^T}$ is the transpose of $\mathbf{F}$ and has size $2 \times 2L$.

CMA pertains to gradient descent algorithms that aim at minimizing a cost function $J(\mathbf{f})$ according to $\mathbf{f}$. Denoting $J(\mathbf{f}^{(k)})$ as $J(\mathbf{f}, k)$, the update equation for the FIR coefficients $\mathbf{f}$ is:

$$\mathbf{f}^{(k+1)} = \mathbf{f}^{(k)} - \mu \nabla_{\mathbf{f},\bar{\mathbf{f}}} J(\mathbf{f}, k), \tag{1.67}$$

where μ is the step-size and $\nabla_{\mathbf{f},\bar{\mathbf{f}}}$ is the operator whose coefficients can be expressed as $2\partial/\partial\bar{\mathbf{f}}$.

The CMA as proposed by [83] utilizes a cost function $J(\mathbf{f})$ given by Eq. (1.68), which aims at minimizing the expectation of the deviation of the squared modulus of the signal from unity.

$$J_{\mathrm{CMA}}(\mathbf{f}) = \mathbb{E}\left[\left(|z|^2 - 1\right)^2\right] = \mathbb{E}\left[\left(z\bar{z} - 1\right)^2\right] \tag{1.68}$$

The update Eq. (1.67) now becomes:

$$\mathbf{f}_{pq}^{(k+1)} = \mathbf{f}_{pq}^{(k)} - 2\mu \left[\frac{\partial J_{\mathrm{CMA}}(\mathbf{f}, k)}{\partial \bar{\mathbf{f}}_{pq}}\right] \tag{1.69}$$

with

$$\frac{\partial J_{\mathrm{CMA}}(\mathbf{f}, k)}{\partial \bar{\mathbf{f}}_{pq}} = 2\mathbb{E}\left[\left(|z_p(k)|^2 - 1\right) z_p(k) \overline{\mathbf{y}}_q(k)\right] \tag{1.70}$$

Plugging Eq. (1.70) into Eq. (1.69) provides the individual filter tap update equations for the CMA equalizer:

$$\mathbf{f}_{pq}^{(k+1)} = \mathbf{f}_{pq}^{(k)} - 2\mu\{2\mathbb{E}\left[\left(|z_p(k)|^2 - 1\right) z_p(k) \overline{\mathbf{y}}_q(k)\right]\} \tag{1.71}$$

Often, the expectation, $\mathbb{E}[.]$ that applies to the cost function is omitted in the literature. The reason for this depends on the nature of the channel environment whether stationary or non-stationary. For stationary environment the expectation is retained and the flavor of the gradient descent algorithm is the method of steepest descent. For a non-stationary environment, the expectation operator is omitted and the flavor of the gradient descent algorithm is the method of stochastic gradient descent [86].

In the stochastic gradient descent case, as the iterations progress, the information from the past samples are propagated into the update equations which mimic an averaging over a sliding window. Thus, without additional complexity, random fluctuations of the channel as the alphabet modulation or the intensity noise are sufficiently filtered out.

The PMD induced by birefringence of the fiber optic channel renders the channel non-stationary, hence the method of stochastic gradient descent is suitable for the CMA equalizer in dynamic channel equalization of such dynamic impairments as PMD. The final update equation for the equalizer filter coefficients, in compact form, is given by Eq. (1.72):

$$\mathbf{f}_{pq}^{(k+1)} = \mathbf{f}_{pq}^{(k)} - 4\mu(|z_p(k)|^2 - 1)z_p(k)\overline{\mathbf{y}}_q(k) \tag{1.72}$$

After a certain number of iterations the CMA equalizer converges and the final filter coefficients obtained are close to the optimal Wiener filter solution [86, 45]. The filter coefficients obtained are not optimal due to the stochastic nature in which the cost function approaches its minimum value. Hence, the final solution will always fluctuate around the optimal minimum value [86].

However, a major advantage of the CMA equalizer is that it does not require an inversion of the signal correlation matrix as in the case of Weiner filter that results in an optimal solution in a wide-sense stationary environment. It also does not require the use of pilot symbols and hence does not have the constraint of transmission overhead. The blind operation of the CMA equalizer also means that it is the equalizer of choice in dynamic channel environments that require robust equalization algorithms. The optical access network is an example of such an environment with optical fibers deployed in a variety of ways and in varying environmental conditions.

Regardless of the aforementioned advantages attributed to the CMA equalizer it has an issue related to the demultiplexing capability upon convergence. We will present this convergence problem next.

1.5.2 Convergence Problem of the CMA Equalizer

The convergence problem of the CMA equalizer arises from the fact that the four filter coefficients (or taps) are updated independently, and some situations may arise where the two output signals of the equalizer lock on to the same polarization tributary [87, 39]. This convergence problem is known as a **singularity**.

When a singularity occurs, it means that two independent signals at the input of the equalizer do not end up as two independent signals at the output of the equalizer. If the two independent signals are on say X- and Y- polarizations at the input of the equalizer (for example corresponding to polarization inputs 1 and 2 of the equalizer in Fig. 1.10) respectively, then the equalizer output signals could either converge to one of the following cases below:

1. X-polarization input and Y-polarization input both converge to X-polarization output (indicating a loss of Y-polarization input information).

2. X-polarization input and Y-polarization input both converge to Y-polarization output (indicating a loss of X-polarization input information).

3. X-polarization input signal is recovered at the Y-polarization output and vice-versa (indicating an inverted polarization convergence).

4. X-polarization input signal is recovered at the X-polarization output, likewise Y-polarization input signal is recovered at the Y-polarization output (indicating proper polarization convergence).

Proper polarization demultiplexing, upon convergence, requires that two orthogonally polarized signals are recovered at the output of the equalizer. Since in practice we do not know which polarization tributary is X or Y, cases 3 and 4 are not considered as singularities. Only cases 1 and 2 are considered as singularities.

There are only a few analyses in the literature about the reason for the occurrence of the singularities. However, a detailed treatment of the cause of the underlying problem was provided in [39] where a control surface analysis of the convergence of the CMA equalizer showed that the singularities arise due to a bifurcation of the estimate of the correct polarization rotation angle for polarization demultiplexing. It also gives a hint that the singularities depend on the polarization rotation angle and the initialization of the filter coefficients. In [87], an analytical treatment of the situation was presented by formulating the problem as that of finding the inverse Jones matrix of the channel.

As stated earlier, the CMA equalizer is well suited for dynamic channel environments such as those of the optical access where robust equalization algorithms will be required in the context of next generation optical access networks. It is therefore necessary to mitigate the singularity problem efficiently if this equalizer must be used.

A considerable amount of work has been directed towards mitigating the singularity problem of the CMA equalizer [87, 88, 89, 90, 91, 92, 93].

In [87] they obtain the filter coefficients for singularity-free polarization demultiplexing by analytically deriving the inverse Jones matrix of the channel. However, they make an assumption that the fluctuation of the phase of the symbols, which occurs at the symbol rate of the QPSK signals, is time-independent. This assumption does not hold except if a constraint is made to transmit the same symbols all the time. They also do not consider the effect of the polarization rotations. In [88] they base their technique on the reasoning that when singularities occur, the convergence of the CMA equalizer is delayed. Hence, they deliberately apply a fixed amount of polarization rotations to a block of the received signal and then compute a metric based on the CMA cost function to determine the polarization state that gives the highest error slope. They then use the value of the phase angles corresponding to the highest error slope to initialize the filter taps for the standard CMA equalizer and update these taps employing a step-size parameter that is variable. While this technique ensures fast convergence, it is not clear if it actually mitigates singularities. Due to the stochastic nature of the convergence of the CMA algorithm, one instantaneous value of the error slope is not sufficient to guarantee proper polarization demultiplexing capability. In [89] they propose to use a training sequence to initialize the filter coefficients, and afterwards proceed with blind equalization. They also monitor the sign of the linear polarization Stokes parameter, S_1, to determine if a singularity will occur or not. They state that in the absence of polarization dependent loss (PDL), the channel matrix is unitary and the S_1 parameter will always be such that singularities will not occur. However, this scheme has the drawback of the training symbol overhead. In [90] they propose PDL mitigation as a means of mitigating singularities and target high PDL regimes. However, their scheme utilizes singular value decomposition and

channel inversion which are computationally expensive. In [91] they propose a two-stage CMA equalizer for singularity mitigation where in the first stage, only two out of the four filters are optimized and then in the second stage all four filters are optimized. However, they use the filter tap initialization strategy of [87, 94] based on the assumption that the polarization tributaries are always orthogonal which, as presented in [88], is not always the case especially in the presence of polarization dependent loss (PDL). In [92] they introduce a correlation based approach for wireless communication and then later applied it to coherent optical communication in [93]. Notably in [93] they state that the occurrence of singularities increases with the polarization mode dispersion (PMD) due to the correlations between the equalizer output signal (i.e. polarization cross-talk) induced by PMD. This method is interesting because it directly addresses the CMA cost function while retaining the fully blind operation of the equalizer. However, the dependence of the parameters of their multi-user (MU) CMA and the channel PMD has not been fully established and the derivation of the MU-CMA update equation has drawbacks that can and should be improved. Therefore, further investigation of this correlation based approach is necessary as there are gaps to be filled which could lead to the development of a correlation based algorithm that is closely related, in terms of complexity, to the already minimally complex standard CMA algorithm, and whose parameters can potentially be tuned to better suit the environment of its deployment. For this reason we proceed with the investigation and present our findings in the next chapter.

CHAPTER 2

A correlation-avoidance CMA for singularity mitigation

Without commitment, you'll never start. Without consistency, you'll never finish.
— Denzel Washington

Contents

2.1 Introduction

The constant modulus algorithm (CMA) equalizer was previously introduced in section 1.5 for impairment equalization in digital coherent optical (DCO) transmission systems. To maximize transmission capacity, DCO systems exploit the available information transmission degrees of freedom of a light wave — i.e. in-phase and quadrature components along two orthogonal polarization tributaries — by utilizing multidimensional modulation formats such as quadrature phase shift-keying (QPSK) and quadrature amplitude modulation (QAM) in dual polarization division multiplexing (PDM) configuration [95].

Recently, this PDM DCO transmission scheme has attracted attention for optical access networks [96, 97] where data rates well beyond 100 Gb/s are anticipated. Moreover, the use of digital signal processing (DSP) alongside coherent detection enables digital equalization of both static and dynamic impairments such as chromatic dispersion (CD) and polarization mode dispersion (PMD) respectively by means of digital filters [39]. Dynamic impairments require the use of adaptive equalizers that track the time variation of the channel and update the equalizers' filter coefficients accordingly by means of gradient descent algorithms. A well-known adaptive equalizer is the multiple-input multiple-output (MIMO) CMA equalizer [83, 98, 92] which, for optical fibre transmission, performs polarization demultiplexing while also compensating for PMD [94, 93, 84, 99].

However, the polarization demultiplexing capability of the CMA is not perfect and the two polarization outputs of the equalizer sometimes converge toward the same input polarization tributary, missing the other orthogonal tributary. This is the so-called singularity issue of the CMA [87, 39, 94]. Various techniques have been proposed to mitigate this issue as in [87, 88, 89, 90, 91] or specifically in [93] where a constraint against multi-user (MU) correlation is added to the CMA, and their limitations have been described in section 1.5.2.

The technique of [93] with multi-user CMA (MU-CMA), is particularly interesting from the point of view of minimizing complexity while enhancing the singularity avoidance performance of CMA. The CMA is already a low-complexity scheme and adding a correlation constraint to the CMA cost function would not result in a drastic increase in its original complexity. However, the relationships between the MU-CMA parameters and the channel parameters for singularity avoidance have not been explicitly provided, the degrees of freedom that the MU-CMA parameters offer have not been fully investigated, and the derivation of the MU-CMA update equation has drawbacks that can be improved. To harness the maximum benefit of the correlation based approach for singularity mitigation, we propose to fully explore the correlation-based approach which will lead to the development of an amended algorithm — Correlation Avoidance (CA)-CMA. This then allows us to derive and establish relationships between the CA-CMA and the channel parameters, and to analyze the robustness of the CA-CMA to varying polarization states over a wide PMD range expected in the optical access [100, 101, 102].

In the following, section 2.2 describes the system and the methodology we adopted. Section 2.3 introduces the channel model for both the PMD-only and combined CD and PMD cases. Section 2.4 presents the equalizer model beginning from the standard CMA to the derivations of the amended correlation-based CA-CMA equalizer. Section 2.5 presents the simulation results and discussion of the singularity performance of the CA-CMA for both the PMD-only and then the combined CD and PMD cases. This introduction, sections 2.2, 2.3.1, 2.4, 2.5.1, and 2.5.2 have been published in [103].

2.2 System description and methodology

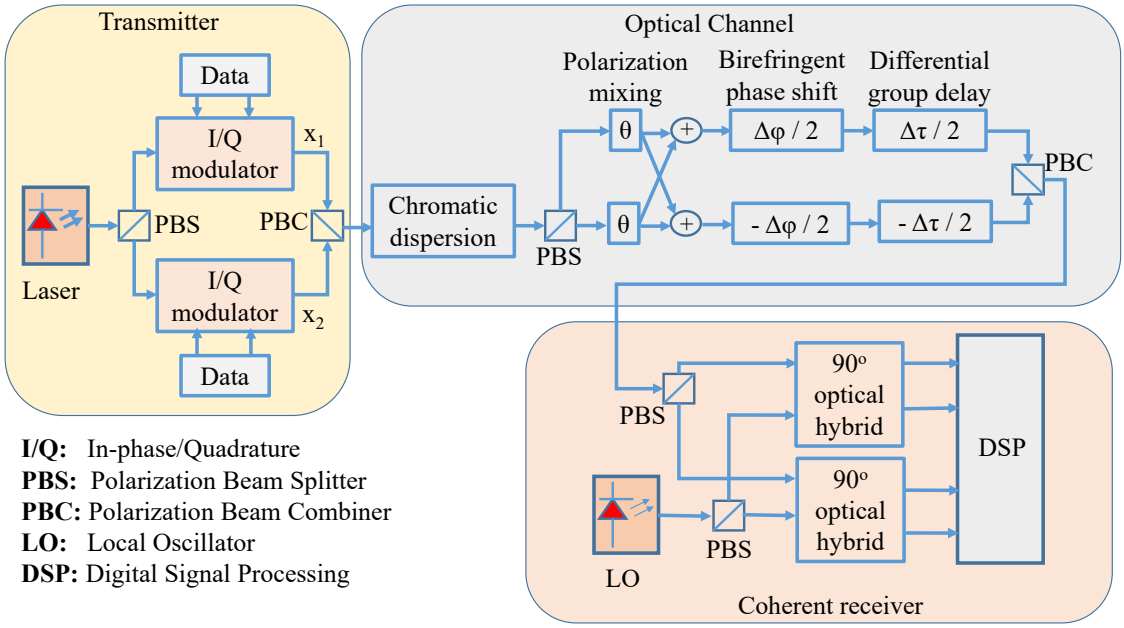

Figure 2.1: Block diagram of dual-polarization digital coherent optical (DCO) simulator model

Focusing on the polarization tributaries, the system block diagram that represents the DCO transmission system is shown in Fig. 2.1.

A laser in C-band (1550 nm) is split by the polarization beam splitter (PBS) into two orthogonal polarization signals each being modulated by two independent randomly generated data sequences through an in-phase/quadrature (I/Q) modulator to yield the I/Q modulated signals $\mathbf{x}_1(t)$ and $\mathbf{x}_2(t)$. The I/Q transmitted sequences are generated using oversampling ratio of 8, and electronically filtered using a Root Raised Cosine (RRC) filter. Then, the modulated signals $\mathbf{x}_1(t)$ and $\mathbf{x}_2(t)$ are polarization multiplexed by the polarization beam combiner (PBC) and propagated through a model of a standard single mode fibre of length 20 km, typical of the optical access.

The impairments taken into account are the attenuation (0.2 dB/km), the chromatic dispersion (17 ps/nm/km) and the instantaneous differential group delay (DGD) which will be referred to in terms of the corresponding instantaneous PMD. Notably different from core or metropolitan networks, the optical access network can suffer from high environmental constraints (e.g. aerial fibres) and ageing, hence the mean PMD can vary over a wide range from link to link and for a given link from time to time. Values ranging from 0.05 ps/$\sqrt{\text{km}}$ up to 1.45 ps/$\sqrt{\text{km}}$ have been reported in outdoor PMD measurements [100]. Given a Maxwellian probability distribution function for the instantaneous PMD, an outage probability of 10^{-7} which corresponds to an outage of 3s per year, leads to realizations of the PMD that can be as high as 8.7 ps/$\sqrt{\text{km}}$.

We introduce the effects due to attenuation and chromatic dispersion (CD) to the PDM signal. Then the polarization rotation mixing effects due to birefringent phase shift, and differential group delay are applied to the orthogonal signals, after which they are again multiplexed by another PBC. A single birefringent element is considered. This permits analysis of specific polarization states and corner cases that lead to singularities.

At the receiver, two PBSs split the PDM received signal and a local oscillator (LO) signal at the same wavelength of the transmit laser. These split signals are respectively

mixed in two 90° optical hybrids to recover the in-phase and quadrature signal components on both polarization axes. The recovered in-phase and quadrature signal components are then passed on to the digital signal processing (DSP) block where they are RRC filtered and downsampled to 2 samples per symbol. Additive White Gaussian noise (AWGN) is introduced to achieve typical BER of 10^{-4}. Then, a group velocity dispersion compensation stage mitigates chromatic dispersion. Next, the adaptive fractionally spaced equalizer (FSE) compensates for the PMD and performs polarization de-multiplexing. Afterwards, carrier phase estimation (CPE) is performed to mitigate both transmitter and LO phase noise. Finally, hard-decision decoding on the transmitted symbols and bit error rate (BER) calculation are performed.

2.3 Channel Model

2.3.1 PMD Channel Model

We will start by considering the PMD impairment acting in the absence of chromatic dispersion (CD). The PMD is modelled by a single birefringence element, in the frequency domain, as a product of a rotation matrix $\mathbf{R}(\theta)$, a differential group delay (DGD) matrix $\mathbf{DGD}(\tau,\omega)$, a birefringent phase shift matrix $\mathbf{B}(\phi)$, and an inverse rotation matrix $\mathbf{R}(-\theta)$:

$$\mathbf{R}(\theta)=\begin{bmatrix}\cos(\theta) & -\sin(\theta)\\ \sin(\theta) & \cos(\theta)\end{bmatrix},\mathbf{B}(\phi)=\begin{bmatrix}e^{j\phi/2} & 0\\ 0 & e^{-j\phi/2}\end{bmatrix},\mathbf{DGD}(\tau,\omega)=\begin{bmatrix}e^{j\omega\tau/2} & 0\\ 0 & e^{-j\omega\tau/2}\end{bmatrix} \tag{2.1}$$

with $j=\sqrt{-1}$. The combined channel effect, $\mathbf{H_{PMD}}(\omega)$ can be written as

$$\mathbf{H_{PMD}}(\omega)=\mathbf{R}(\theta)\mathbf{B}(\phi)\mathbf{DGD}(\tau,\omega)\mathbf{R}(-\theta) \tag{2.2}$$

and the matrix multiplication Eq. (2.2) can be simplified to:

$$\mathbf{H_{PMD}}(\omega)=\begin{bmatrix}\cos(\chi)+j\sin(\chi)\cos(2\theta) & j\sin(\chi)\sin(2\theta)\\ j\sin(\chi)\sin(2\theta) & \cos(\chi)-j\sin(\chi)\cos(2\theta)\end{bmatrix} \tag{2.3}$$

with $\chi=(\omega\tau+\phi)/2$.

The signal received into the equalizer is impaired by $\mathbf{H_{PMD}}(\omega)$ and noise $\mathbf{N}(\omega)$ and given, in frequency domain, as

$$\mathbf{Y}(\omega)=\mathbf{H_{PMD}}(\omega)\mathbf{X}(\omega)+\mathbf{N}(\omega) \tag{2.4}$$

with $\mathbf{Y}(\omega)=[\mathbf{Y_1}(\omega),\mathbf{Y_2}(\omega)]^{\mathrm{T}}$, $\mathbf{X}(\omega)=[\mathbf{X_1}(\omega),\mathbf{X_2}(\omega)]^{\mathrm{T}}$ and $\mathbf{N}(\omega)=[\mathbf{N_1}(\omega),\mathbf{N_2}(\omega)]^{\mathrm{T}}$.

The resulting time domain expression for the received signal is (see derivation in appendix A):

$$\begin{aligned}\mathbf{y_1}(t)=\mathbf{x_1}\left(t+\frac{\tau}{2}\right)e^{j\frac{\phi}{2}}\cos^2(\theta)+\mathbf{x_1}\left(t-\frac{\tau}{2}\right)e^{-j\frac{\phi}{2}}\sin^2(\theta)\\ +\left(\frac{\mathbf{x_2}\left(t+\frac{\tau}{2}\right)e^{j\frac{\phi}{2}}-\mathbf{x_2}\left(t-\frac{\tau}{2}\right)e^{-j\frac{\phi}{2}}}{2}\right)\sin(2\theta)+\mathbf{n_1}(t)\end{aligned} \tag{2.5}$$

$$\begin{aligned}\mathbf{y_2}(t)=\mathbf{x_2}\left(t+\frac{\tau}{2}\right)e^{j\frac{\phi}{2}}\sin^2(\theta)+\mathbf{x_2}\left(t-\frac{\tau}{2}\right)e^{-j\frac{\phi}{2}}\cos^2(\theta)\\ +\left(\frac{\mathbf{x_1}\left(t+\frac{\tau}{2}\right)e^{j\frac{\phi}{2}}-\mathbf{x_1}\left(t-\frac{\tau}{2}\right)e^{-j\frac{\phi}{2}}}{2}\right)\sin(2\theta)+\mathbf{n_2}(t)\end{aligned} \tag{2.6}$$

Eq. (2.5) and Eq. (2.6) describe the intersymbol interference (ISI) and cross-talk that PMD induces. It is also clear to see that in a hypothetically ideal condition where $\tau = 0$ and $\phi = 0$, only the AWGN noise affects the transmitted signal. There would be other impairments e.g. due to phase noise and frequency offset but we will not model them here.

2.3.2 PMD + CD Channel Model

In case CD is not compensated, then we will have the PMD and CD impairments acting together. The effect of the CD is the same for the two received polarization tributaries. The frequency domain expression of the CD channel model, $\mathbf{H_{CD}}(\omega)$ is given as [76]:

$$\mathbf{H_{CD}}(\omega) = \begin{bmatrix} e^{\frac{-j\beta_2\omega^2 z_f}{2}} & 0 \\ 0 & e^{\frac{-j\beta_2\omega^2 z_f}{2}} \end{bmatrix} \tag{2.7}$$

where β_2 is the dispersion coefficient, ω is the angular frequency, and z_f is the fiber length. The combined channel effect with PMD and CD can then be expressed in frequency domain as:

$$\mathbf{H}(\omega) = \mathbf{H_{CD}}(\omega)\mathbf{H_{PMD}}(\omega) \tag{2.8}$$

and the matrix multiplication Eq. (2.8) can be simplified to:

$$\mathbf{H}(\omega) = \begin{bmatrix} e^{-\xi}(\cos(\chi) + j\sin(\chi)\cos(2\theta)) & e^{-\xi}(j\sin(\chi)\sin(2\theta)) \\ e^{-\xi}(j\sin(\chi)\sin(2\theta)) & e^{-\xi}(\cos(\chi) - j\sin(\chi)\cos(2\theta)) \end{bmatrix} \tag{2.9}$$

with $\xi = (j\beta_2\omega^2 z_f)/2$.

The received signal into the equalizer, in frequency domain, is then:

$$\mathbf{Y}(\omega) = \mathbf{H}(\omega)\mathbf{X}(\omega) + \mathbf{N}(\omega) \tag{2.10}$$

In time domain, the received signal is a convolution of the time domain expressions of Eq. (2.7) and Eq. (2.4).

2.4 CMA, MU-CMA and CA-CMA Equalizers

In this section we will proceed with the investigation of the correlation-based CMA equalizer by re-deriving the update equations starting from the cost function of the standard CMA equalizer.

The principle of operation and the derivation of the CMA equalizer update equations were provided in section 1.5.1. Maintaining the same notations for the signals and utilizing the same butterfly equalizer structure of Fig. 1.10, we will proceed to the cost function analysis to introduce the correlation-based criterion. We however recall the fractionally-spaced equalizer (FSE) filters of length L, $\mathbf{f}_{pq}^{(L)}$ with $p, q \in \{1, 2\}$; the m-times oversampled input signal to the equalizer $\mathbf{y}_q(k)$; and the symbol-spaced output signal from the equalizer $\mathbf{z}_p(k)$, with k the iteration index.

In a polarization division multiplexing (PDM) context, the PMD impairment induces correlations between the equalizer input signals which lead to CMA singularities [94, 93, 84, 99]. Hence, if these correlations are penalized, the equalizer can be made more robust against singularities. This is the reasoning followed by [93] adding a multi-user cross-correlation constraint as proposed in [92] to the standard CMA cost function proposed

by [83]. The new cost function $J_{\text{MU-CMA}}(\mathbf{f}, k)$, leaving out the p, q subscripts, can be expressed as:

$$J_{\text{MU-CMA}}(\mathbf{f}, k) = J_{\text{CMA}}(\mathbf{f}, k) + J_{\text{CA}}(\mathbf{f}, k) \tag{2.11}$$

with the cross-correlation constraint,

$$J_{\text{CA}}(\mathbf{f}, k) = \sum_{p,q;p\neq q} \sum_{\delta=\delta_1}^{\delta_2} |r_{pq}(\delta)|^2 \tag{2.12}$$

where $r_{pq}(\delta) = \mathbb{E}\left[z_p(k)\overline{z_q}(k-\delta)\right]$ is the expectation of the cross-correlations between equalizer polarization outputs (p, $q \in \{1, 2\}$) at iteration k, δ being the correlation lag that permits to embrace the maximum differential group delay (DGD). The constraint on the cross-correlations is introduced by their square modulus since otherwise, being either positive or negative they could cancel out each other, thus reducing the strength of the constraint.

In line with the gradient descent algorithm approach of function minimization, the multi-user CMA (MU-CMA) introduced in [93] has the general form of the filter update equation (leaving out the p, q subscripts) as

$$\mathbf{f}^{(k+1)} = \mathbf{f}^{(k)} - \mu \nabla_{\mathbf{f},\bar{\mathbf{f}}} J_{\text{MU-CMA}}(\mathbf{f}, k) \tag{2.13}$$

Recall that μ is the step-size and $\nabla_{\mathbf{f},\bar{\mathbf{f}}}$ is the operator whose coefficients can be expressed as $2\partial/\partial\bar{\mathbf{f}}$. The factor 2 comes from the Wirtinger calculus for computing complex gradients [45].

The update Eq. (2.13) now becomes:

$$\mathbf{f}_{pq}^{(k+1)} = \mathbf{f}_{pq}^{(k)} - 2\mu \left[\frac{\partial J_{\text{CMA}}(\mathbf{f}, k)}{\partial \bar{\mathbf{f}}_{pq}} + \frac{\partial J_{\text{CA}}(\mathbf{f}, k)}{\partial \bar{\mathbf{f}}_{pq}} \right] \tag{2.14}$$

with

$$\frac{\partial J_{\text{CMA}}(\mathbf{f}, k)}{\partial \bar{\mathbf{f}}_{pq}} = 2\mathbb{E}\left[(|z_p(k)|^2 - 1) z_p(k) \overline{\mathbf{y}}_q(k) \right] \tag{2.15}$$

and

$$\frac{\partial J_{\text{CA}}(\mathbf{f}, k)}{\partial \bar{\mathbf{f}}_{pq}} = 2 \sum_{\substack{n=1 \\ n\neq p}}^{2} \sum_{\delta=\delta_1}^{\delta_2} r_{pn}(\delta)\ \mathbb{E}\left[z_n(k-\delta)\ \overline{\mathbf{y}}_p(k) \right]. \tag{2.16}$$

Plugging Eq. (2.15) and Eq. (2.16) into Eq. (2.14) provides the individual filter tap update equations with both CMA and CA contributions as given by Eq. (2.17):

$$\begin{aligned} \mathbf{f}_{pq}^{(k+1)} = \mathbf{f}_{pq}^{(k)} - 2\mu \{ & 2\mathbb{E}\left[(|z_p(k)|^2 - 1) z_p(k) \overline{\mathbf{y}}_q(k) \right] \\ & + 2 \sum_{\substack{n=1 \\ n\neq p}}^{2} \sum_{\delta=\delta_1}^{\delta_2} \mathbb{E}\left[z_p(k) \overline{z_n}(k-\delta) \right]\ \mathbb{E}\left[z_n(k-\delta)\ \overline{\mathbf{y}}_p(k) \right] \}. \end{aligned} \tag{2.17}$$

Often, $\mathbb{E}[.]$ that applies to the CMA contribution in Eq. (2.17) is omitted in the stochastic gradient context since as the iteration process progresses, the information from the past samples is propagated into the update equations which mimics an averaging over a sliding window. Thus, random fluctuations of the channel with the alphabet modulation or the intensity noise are sufficiently filtered out without additional complexity. Hence, we do not account for $\mathbb{E}[.]$ either. Conversely, considering the cross-correlation contribution that is PMD dependent, the averaging operation has a deep impact on the proper convergence

of the algorithm as shown and discussed in the coming sections. Therefore, $\mathbb{E}[.]$ is implemented in the cross-correlation contribution using a uniform averaging over the most recent w symbols as introduced in Eq. (2.18).

Dealing with the correlation lag δ, the symmetric interplay of the polarizations suggests considering values centered at zero. In that case, the property of the discrete cross-correlation $r_{pq}(\delta) = r_{qp}(-\delta)$ allows to reduce the summation over δ to the positive integers while doubling related cross-correlation contributions. Then, also doubling the contribution at $\delta = 0$ and making $\mu' = 4\mu$ leads to update equations similar to [93]. This is not the way we have followed. We strictly implement the cross-correlation over $[-\delta_2, \delta_2]$.

Finally, comes an original contribution of ours — a set of coefficients update equations referred to as correlation-avoidance CMA (CA-CMA):

$$\mathbf{f}_{pq}^{(k+1)} = \mathbf{f}_{pq}^{(k)} - 4\mu\{(|z_p(k)|^2 - 1)z_p(k)\overline{\mathbf{y}}_q(k) + \frac{1}{w^2} \times \sum_{\substack{n=1 \\ n\neq p}}^{2} \sum_{\delta=-\delta_2}^{\delta_2} \sum_{i=k}^{k-w+1} [z_p(i)\overline{z_n}(i-\delta)] \sum_{i=k}^{k-w+1} [z_n(i-\delta)\ \overline{\mathbf{y}}_p(i)]\}. \quad (2.18)$$

The CA-CMA differs from the MU-CMA in the following respects:

1. The use of the expectation operator in the cross-correlation contribution of Eq. (2.18).
2. The introduction of the w, the window size.
3. The sum of the cross-correlation over $[-\delta_2, \delta_2]$ rather than $[0, \delta_2]$

2.5 Simulation Results

2.5.1 Simulation parameters and results (PMD-only case)

The aim of the simulation is to verify through the analysis of the number of singularities n_s, the capabilities of the CA-CMA algorithm against PMD according to the parameters of the CA-CMA: the number of taps L, the correlation lag depth δ_2, and the window size, w. To that turn, we subject the CA-CMA algorithm to different polarization states and PMD variations as listed in Table 2.1. We considered 2000 polarization states uniformly distributed over the Poincaré sphere. The number of singularities, n_s, obtained will be the major metric of interest. It corresponds to the number of polarization states, out of the 2000 states, which converge to a singularity situation. We represent deterministic instantaneous DGD values by the corresponding instantaneous PMD values. Recall that the PMD is a random variable that follows a Maxwellian probability distribution. Hence, we will discuss in terms of the instantaneous PMD values, referring to it as PMD. The range of PMD values considered is 0 to 10 ps/$\sqrt{\text{km}}$ (at intervals of 1 ps/$\sqrt{\text{km}}$) to depict the values obtainable in the optical access network [100]. The range of the correlation lag depth δ_2 is from 0 to 10 to verify and establish a bound for the conjecture in [93] about δ_2.

Considering the range of values for the variables; PMD (11 values), the number of taps (5 values), the correlation lag depth (11 values), and the window size (4 values), the total combination of variables amounts to 2420 possible combinations. Each of these combinations is one realization of a channel with a fixed set of parameters for the CA-CMA. We would then like to retrieve the configuration for which we have the least amount of singularities. We consider proper convergence of the algorithms toward the steady state once the relative change in the values of the equalizer coefficient (tap) weights falls down

Table 2.1: Simulation parameters

Parameter	**Value**
Modulation format	QPSK
Baud rate R_s	32 GBd
Oversampling	2 at the equalizer inputs
Fibre length l	20 km
Dispersion parameter	17 ps/nm/km (C-band)
PMD realizations	[0: 10] ps/$\sqrt{\text{km}}$
Theta, θ	$[-\pi/2 : \pi/2]$
Phi, ϕ	$[0 : \pi]$
Bit Error Ratio (BER)	10^{-4}
Number of taps of equalizer L	[5, 9, 13, 17, 21]
Iterations stopping criterion th	[3×10^{-4},10^{-5}]
Step-size μ	0.001
Correlation lag depth δ_2	[0: 10]
Correlation window size w	[10, 20, 30, 40]

to a given mean absolute error threshold value, th. A simulation approach is considered because the fast variation of the PMD are difficult to reproduce in the lab. Since a simulation approach is considered, there might be statistical variation of the results depending on the random seeds. We proceed with a single random seed at first to ensure a reasonable simulation time and then examine the effect of the randomness afterwards.

Fig. 2.2 shows the singularity signature, n_s, as a function of the total parameter combinations for CA-CMA with th values of 3×10^{-4} and 10^{-5}, and for conventional or standard CMA with th equal to 10^{-5}. The periodic pattern of spikes seen is due to the repeated ordering of the other parameters for the different PMD values which make up the parameter combinations. These combinations are described by the parameter combination index on the horizontal- or x-axis. Related values of the parameters are displayed in the lower subplot. We observe an overall n_s variation that remains relatively consistent across all parameter combinations up to 4 ps/$\sqrt{\text{km}}$ PMD. Then, it increases to a maximum between parameter combination indices 1500 and 2000 corresponding to 7 and 8 ps/$\sqrt{\text{km}}$ respectively before decreasing toward an average of 50 after 8 ps/$\sqrt{\text{km}}$. Whereas the CMA equalizer never achieves singularity-free operation, there are sets of parameters that guarantee zero singularities using the CA-CMA up to 4 ps/$\sqrt{\text{km}}$ PMD.

Fig. 2.3 is a zoom on one spike region of Fig. 2.2 within the vertical dashed lines near the parameter combination index 1000 (i.e. 4 ps/$\sqrt{\text{km}}$ PMD) and also retaining only the combinations corresponding to $L = 5$. In same Fig. 2.3, the regions over which the window size w is constant are demarcated along the horizontal dashed line and the value of the window size is displayed below the line. Within each window size region, the correlation lag depth δ_2 varies from 0 to 10. CA-CMA with th of 3×10^{-4} does not achieve zero singularity whereas CA-CMA with th equals to 10^{-5} achieves it. While not shown here, lower th have been tested over the combinations set for both CMA and CA-CMA. It did not provide any further reduction of n_s. Thus, 10^{-5} can be seen as the optimal threshold. Otherwise, Fig. 2.3 shows that n_s decreases as w increases. However, at each w, two regions can be identified: a dip at the smallest δ_2 (0,1), with few singularities that

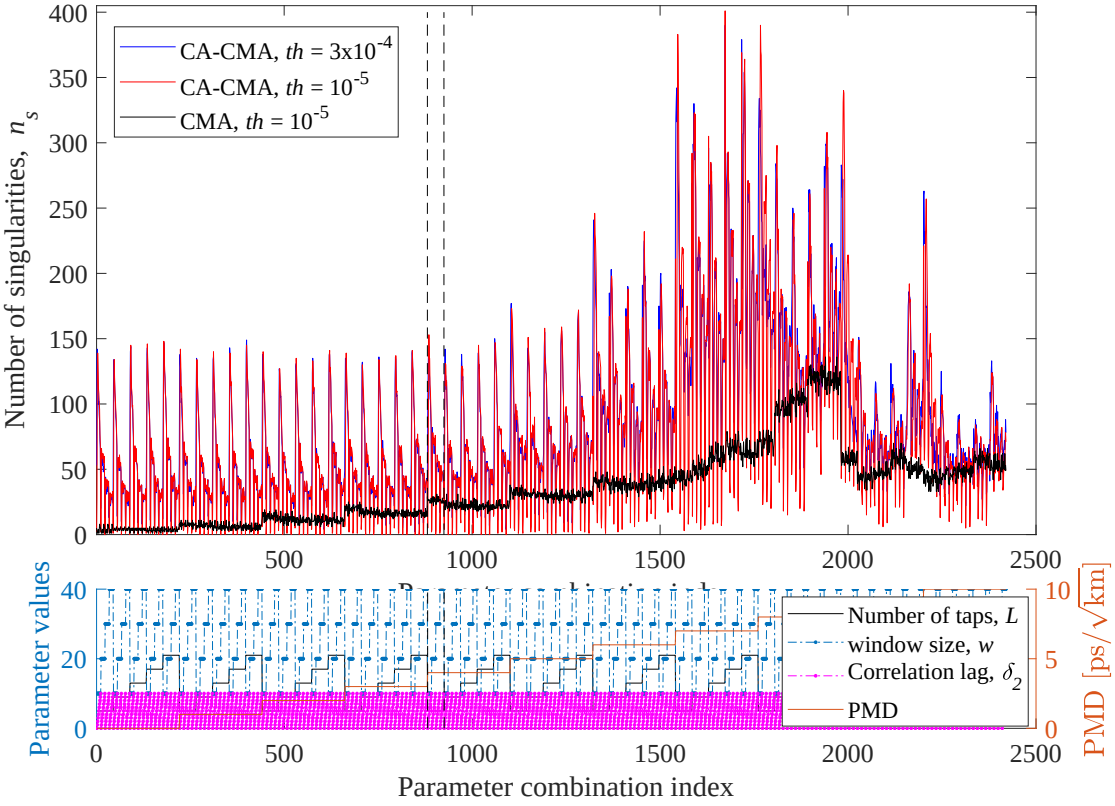

Figure 2.2: Singularity signature for CMA, CA-CMA

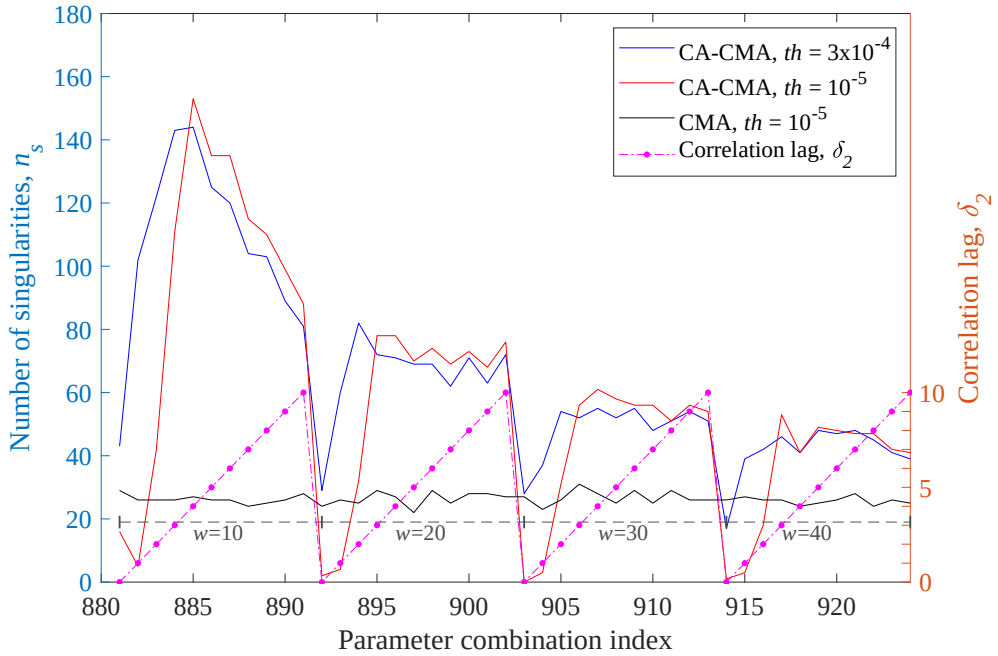

Figure 2.3: Singularity signature of CMA and CA-CMA according to w and δ_2 at 4 ps/$\sqrt{\text{km}}$ PMD for 5 filter taps.

increasing w can reduce down to zero and another region with high n_s levels on which, increasing w has a stronger quenching impact than increasing δ_2.

So, focusing on the smaller values of δ_2, the impact of δ_2 according to PMD and the number of taps is shown Fig. 2.4, for a given w. For $\delta_2 = 0$, as already underlined, CA-CMA can ensure zero singularity up to 4 ps/$\sqrt{\text{km}}$ at some L. Afterwards, n_s increases sharply. For $\delta_2 = 1$, although robust against singularities at low PMD, from 0 up to 3 ps/$\sqrt{\text{km}}$, zero singularity is not achieved, contrary to the range 3 to 5 ps/$\sqrt{\text{km}}$ where zero singularity is achieved. After 5 ps/$\sqrt{\text{km}}$, n_s increases sharply. For $\delta_2 = 2$, over 0 to 2 ps/$\sqrt{\text{km}}$ the curve levels off before decreasing down to a minimum shifted by about 2 ps/$\sqrt{\text{km}}$ as compared to the case $\delta_2 = 1$. Then, it increases again sharply. However, in any case n_s is always significantly higher than what is obtained with δ_2 equals 0 or 1. The curve for $\delta_2 = 3$ has similar behaviour but shifted even further toward the highest PMD values.

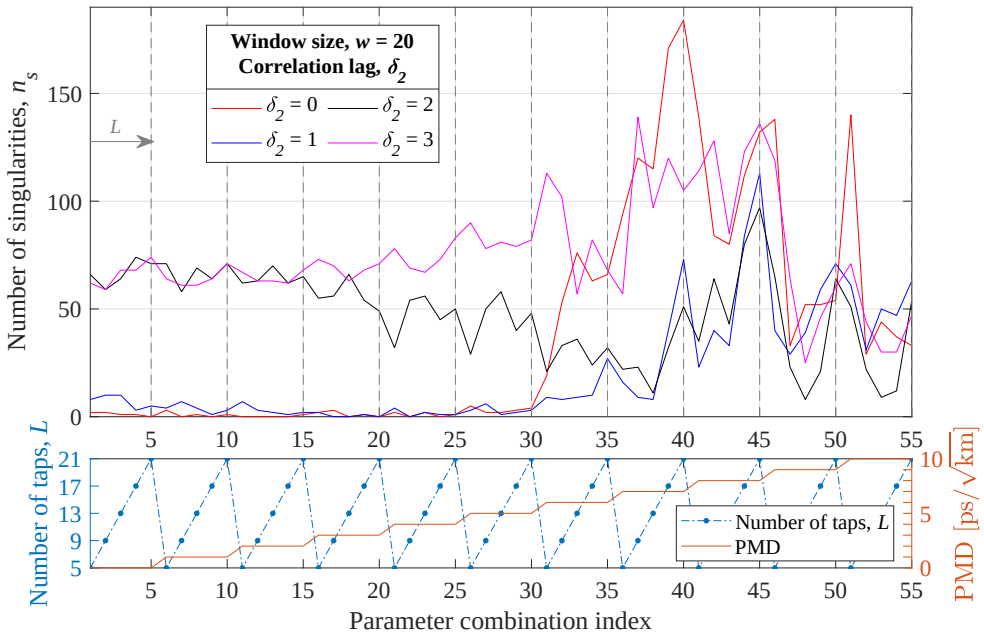

Figure 2.4: Dependence of singularities on δ_2 at $w = 20$ for CA-CMA

Fig. 2.5 plots the set of parameters leading to zero singularity i.e. the operating points of CA-CMA. From 0 to 5 ps/$\sqrt{\text{km}}$ PMD, the number of taps 13 allows to cover the overall PMD range. Here, can also be found the highest density of working {PMD,w} couples. L equals to 9 and 21 allow to cover PMD up to 4 ps/$\sqrt{\text{km}}$, while with $L = 5$, the algorithm shows weaker avoidance capability. One can view also that as the PMD increases the window size should be increased to get at least one working point. Particularly, a window size of 10 can only achieve zero singularity in the range of 0 to 1 ps/$\sqrt{\text{km}}$.

2.5.2 Discussion

Considering PMD mitigation, as seen in Fig. 2.2 and Fig. 2.3, for certain equalizer parameters, CA-CMA clearly outperforms conventional CMA with respect to the singularity avoidance capability, enabling singularity-free operation. A value of $\delta_2 = 0$ allows zero singularities over 0 to 5 ps/$\sqrt{\text{km}}$ PMD. While in our analysis the PMD is significantly worse than what is usually considered, and although PMD range explored in [93] is not explicitly mentioned, our finding gives a value significantly lower than $\delta_2 = 18$ mentioned in

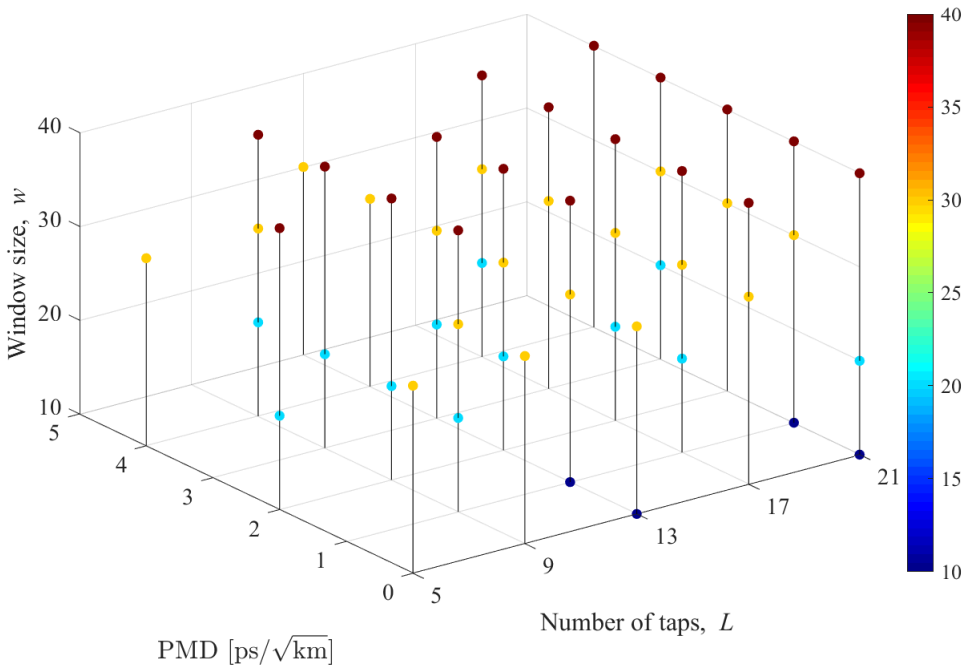

Figure 2.5: Parameters potentially leading to singularity-free operation for CA-CMA

[93]. This lower value would enable a significant reduction of complexity and computation efforts.

Otherwise, as we go deeper into the details, according to Fig. 2.4, the dips of the singularity signature corresponding to the lowest singularity locations, are dependent on both the value of δ_2 and the PMD. The higher the PMD, the higher the cross-correlation lag should be: δ_2 set to 0 up to 5 ps/$\sqrt{\text{km}}$ PMD, δ_2 set to 1 over the 5 to 6 ps/$\sqrt{\text{km}}$ PMD region, *etc.* 5 ps/$\sqrt{\text{km}}$ PMD corresponds to 22.36 ps time spreading or 71.5% of the symbol time T_s, 5 to 6 ps/$\sqrt{\text{km}}$ corresponds to 71.5% to 86% of T_s.

Furthermore, Fig. 2.3, shows that beyond $\delta_2 = 2$ the increase of δ_2 has no impact any more. This is consistent with the fact that at PMD corresponding to DGD less than T_s, the synchronous samples with δ_2 equal to zero are sufficient to get the cross-correlation and build the constraint. Afterwards, δ_2 equals 1 or 2 is necessary. Since even for a PMD value of 10 ps/$\sqrt{\text{km}}$ the DGD (44.72 ps) is less than 2 symbols, capturing cross-correlation beyond $\delta_2 = 2$ is not relevant.

The issue is that the proper tuning of δ_2 with the PMD does not work as efficiently as the PMD increases: as observed in Fig. 2.4, even at the minimum of the curves, beyond $\delta_2 = 2$, n_s never reaches the zero-singularity floor any more. However, Fig. 2.3 reveals that the increase of w is able to quench this increase of n_s, including at its minimum. This gives insight about a relationship between the noise level and the increase of n_s. An interpretation is that increasing the correlation lag depth δ_2 permits capturing cross-correlations induced with higher DGD but, still, it captures the contributions at lower δ_2 where there is no signal anymore (noisy cross-correlations). In this context, a refined scheme can be envisioned to extend the capability of CA-CMA by selecting only the cross-correlation in coincidence with the DGD or, in a more general way, giving higher weight to cross-correlations that have higher signal-to-noise ratio (SNR).

2.5.2.1 Reliability of zero-singularity parameters

For low values of δ_2 and within a given range of the instantaneous PMD, 0-5ps/$\sqrt{\text{km}}$, zero singularities have been shown to be possible from the results and discussion above. However, the number of singularities n_s is not absolutely always zero for all parameter combinations corresponding to these low values of δ_2 and in the PMD range 0-5ps/$\sqrt{\text{km}}$. This raises the question about how reliable the zero-singularity parameters are. We can measure this reliability by running multiple simulations with different random seed values and then calculating how many of the runs result in zero singularities, i.e. $n_s = 0$. The reliability, r would then be a ratio of the number of runs that result in $n_s = 0$ to the total number of runs.

We perform this reliability test using 50 random seed values for a selection of 5 parameter combinations among the parameter combinations that resulted in zero singularities. The use of 50 random seeds and not more is because of the time it takes to run the simulations and for statistical significance, 50 simulation runs are acceptable.

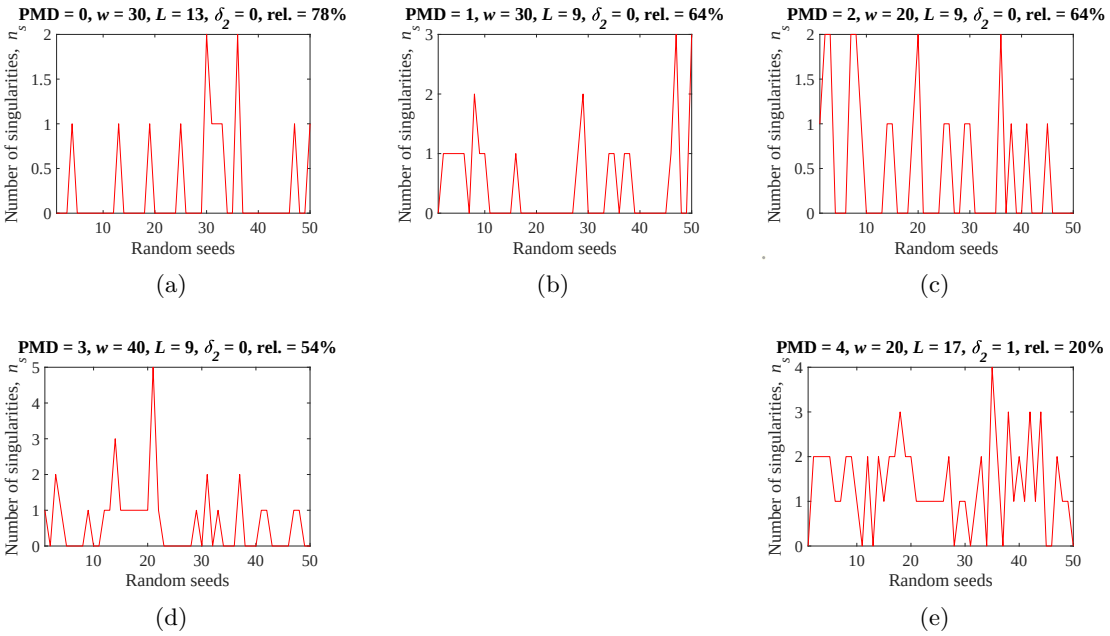

Figure 2.6: Reliability of zero-singularity parameters

Fig. 2.6 presents the results of the reliability test for five selections among the parameter combinations that lead to zero singularities. We can see that as the PMD increases, the reliability decreases. At a window size $w = 30$ as in Fig. 2.6a and Fig. 2.6b, the reliability is 78% at a PMD = 0 and 64% at a PMD = 1ps/$\sqrt{\text{km}}$, and $L = 9$. Looking at Fig. 2.6c and Fig. 2.6d, at $L = 9$, when the PMD increases from 2ps/$\sqrt{\text{km}}$ to 3ps/$\sqrt{\text{km}}$ an increase in w cannot improve the reliability at this higher PMD value. The reliability does not get better than 64% but rather degrades to 54%. This shows that as the PMD increases, the reliability decreases.

2.5.3 Simulation parameters and results (CD + PMD case)

Here, the aim is to verify through the analysis of the number of singularities, n_s, the singularity avoidance capability of the CA-CMA algorithm in the presence of both CD and PMD according to the parameterization of the CA-CMA. The parameters of the CA-

CMA considered are the number of taps L, the correlation lag depth δ_2, and the window size w.

The simulation set-up and parameters are the same as that shown in Fig.2.1 and section 2.5.1 respectively, with the exception that in the DSP block, we do not implement group velocity dispersion (GVD) compensation which equalizes the CD-induced inter-symbol interference (ISI). This could lead to a trade-off on the overall DSP complexity where the CD mitigation can be made less complex or even totally left out.

As in section 2.5.1 we subject the CA-CMA algorithm to different polarization states and PMD values, with a fixed CD. We considered the same 2000 polarization states uniformly distributed over the Poincaré sphere (as in section 2.5.1) and chromatic dispersion dictated by the dispersion parameter, $D = 17$ ps/nm/km which corresponds to the dispersion parameter value in C-band for the standard single mode fiber. From the reliability analysis, we consider a window size $w = 40$, and a number of taps, $L = 13$ which we have shown to be more robust compared to other equalizer parameter selections.

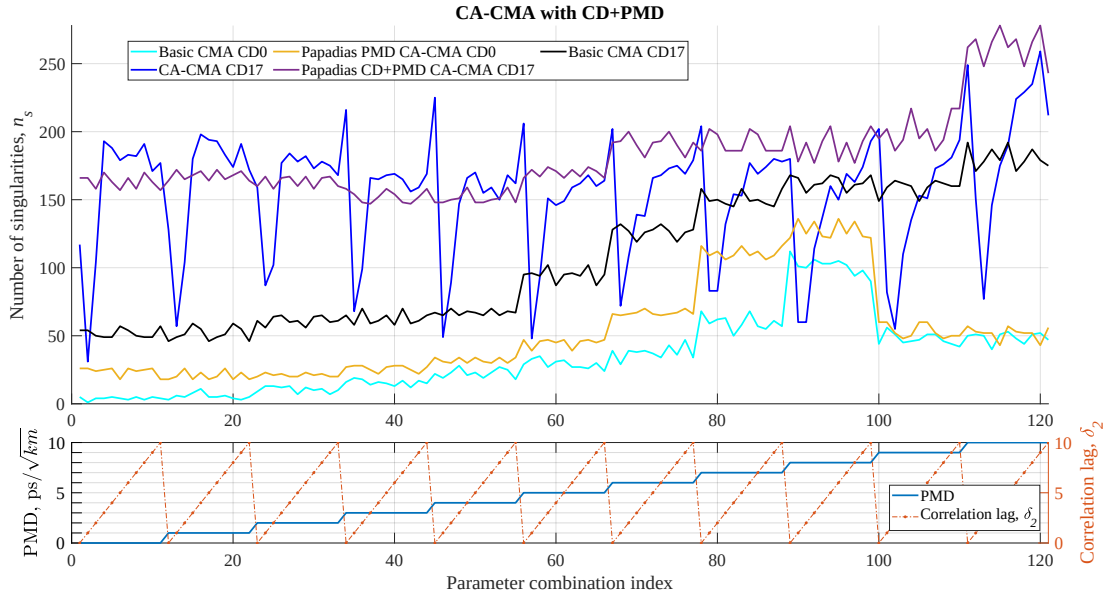

Figure 2.7: CA-CMA in the presence of both CD and PMD

Fig 2.7 presents the simulation results for the singularity avoidance performance of the CA-CMA in the presence of both CD and PMD. The lower plot indicates the evolution of the PMD in a step-wise manner and the evolution of δ_2 within each PMD region. Only the curve, in the upper plot, with the dips (i.e. CA-CMA CD17) has a variation with δ_2. The other CA-CMA curves are plotted for fixed values of δ_2, while the basic/standard CMA curves do not have any dependence on δ_2. However, within each PMD region, for the curves that are plotted at a fixed value of δ_2, the same value of δ_2 is repeated (10 times) in 10 simulation runs, each with a different random seed, as a fast way to investigate the reliability. While for the basic CMA curves, 10 simulation runs at different random seeds are made for the same purpose. Within each PMD region when either δ_2 is fixed or there is no dependence on δ_2 (as in the standard CMA), a reliable n_s would mean that the variability of n_s should not have a dynamic range that exceeds 50 singularities. We compare the CA-CMA in the configuration of [93] with $\delta_2 = 18$, the basic/standard CMA, and the CA-CMA (with varying correlation lags depths from $\delta_2 = 0$ to $\delta_2 = 10$). We also indicate the curves with chromatic dispersion compensated (i.e. represented by

CD0 in the legend) alongside the curves for uncompensated CD (i.e. CD17, where CD17 means that the dispersion parameter value is 17 ps/nm/km) for a comparison of the effect of CD on the number of singularities. The black curve is the standard CMA with CD uncompensated. For this curve we can see that at a PMD of 0 ps/$\sqrt{\text{km}}$ the number of singularities is about 50 and this number increases to about 70 as the PMD increases up to 4 ps/$\sqrt{\text{km}}$. Beyond a PMD of 4 ps/$\sqrt{\text{km}}$, n_s increases rapidly reaching about 180 at 10 ps/$\sqrt{\text{km}}$ PMD. The blue curve is the CA-CMA, with CD uncompensated, for values of δ_2 varying from 0 to 10 within each PMD region, as shown in the subplot below the singularity signature curves. For this blue curve, we can see that, just like in the PMD-only case of Fig. 2.3, there are values of δ_2 for which we can obtain a minimum number of singularities, at the dips in the curve, compared to other values of δ_2. These dips occur at $\delta_2 = 1$ for the PMD range 0–5 ps/$\sqrt{\text{km}}$, and at $\delta_2 = 2$ for the PMD range 5–10 ps/$\sqrt{\text{km}}$. We can find working points of the CA-CMA where the value of n_s obtained with the CA-CMA is lower than that obtained with the standard CMA for the PMD value of 0 ps/$\sqrt{\text{km}}$ and for the PMD range 4–10 ps/$\sqrt{\text{km}}$, while being approximately the same for a PMD value of 1 ps/$\sqrt{\text{km}}$, and slightly higher for the PMD range 2–3 ps/$\sqrt{\text{km}}$. It can also be seen that the minimum n_s achieved by the CA-CMA in the presence of both CD and PMD is able to outperform the n_s achieved by the implementation of [93] in the PMD range 7–8 ps/$\sqrt{\text{km}}$ when [93] is handling a simpler situation of PMD alone. At a PMD range of 8 ps/$\sqrt{\text{km}}$ the CA-CMA is also able to outperform the n_s of the standard CMA when standard CMA is handling a simpler situation of PMD-only, and it matches the performance of the case when standard CMA handles PMD alone at 9 ps/$\sqrt{\text{km}}$. Finally looking at the performance of the implementation of [93] when handling both CD and PMD, the n_s is always greater than 150 across all the PMD range considered reaching a maximum n_s of about 280, which is 3 times worse than the CA-CMA, at 10 ps/$\sqrt{\text{km}}$. In fact, the CA-CMA always has working points across the whole PMD range for which it outperforms the implementation of [93].

2.5.4 Discussion

In the presence of CD and PMD, Fig. 2.7 indicates that working points exist for the CA-CMA with the potential to achieve an average lower n_s when compared to both the standard CMA and the scheme implemented in [93], for the range of PMD considered. Particularly, for the PMD range of 4–10 ps/$\sqrt{\text{km}}$, the CA-CMA shows working points that achieve about twice less the n_s achieved by the standard CMA, while showing working points that outperform the implementation of [93] along all the PMD range considered.

We note that the effect of the CD increases the number of singularities such that it is no longer possible to find any working points with zero singularities across the PMD range when the CA-CMA handles both CD and PMD. This is because the effect of the CD causes further spreading in the symbols which results in a reduction in their peak values following the energy conservation principle. The signal-to-noise-ratio (SNR) of the cross-correlations will therefore be decreased, hence the sensitivity of the CA-CMA to cross-correlations is decreased.

At a dispersion parameter value, $D = 17$ ps/nm/km, for a 20 km fiber, the CD-induced spreading corresponds to 8 symbol periods. At PMD of 10 ps/$\sqrt{\text{km}}$ for this length of fiber, the PMD-induced spreading corresponds to a maximum of two symbol periods. Therefore, the total maximum impairment-induced spreading of the signal is about 10 symbol periods. With this large spreading of the combined impairment, we see from Fig. 2.7 that minimum values of n_s are still possible over the PMD range for $\delta_2 = 1$ in the PMD range 0–5 ps/$\sqrt{\text{km}}$, and $\delta_2 = 2$ in the PMD range 5–10 ps/$\sqrt{\text{km}}$. This is

similar to what is observed in the PMD-only case of Fig. 2.3 where the minimum n_s, which could reach zero over the PMD range 0–4 ps/$\sqrt{\text{km}}$, were obtained at $\delta_2 = 0$ and $\delta_2 = 1$ — values lower than in the case of joint PMD and CD compensation.

The proximity in the values of δ_2 between the PMD-only and the joint PMD and CD cases is not unexpected, even though the total impairment spread difference between both cases is about a factor of 5, because the CD spreading does not contribute to polarization mixing but only to ISI. Hence, increasing the value of δ_2 will not result in an extraction of meaningful information about the cross-correlations, but will introduce noisy cross-correlation of the ISI impaired symbols.

However, it might be possible that lower values of n_s can be obtained if the cross-correlations can be sampled (leading to specific cross-products) and computed in such a way as to avoid a great portion of ISI-impaired symbols and selecting the symbols for which there is limited effect of the ISI.

2.6 Conclusion

Analyzing the degrees of freedom that the CMA equalizer and the MU-CMA equalizer of [93] offer, we have introduced CA-CMA equalizer. Using a deterministic approach, we have then studied the singularity avoidance capability of CA-CMA according to its parameters over a wide PMD realization range expected in the optical access network. In that respect, more explicitly than what can be found in the literature, we have been able to exhibit reliable working points of the CA-CMA that lead to singularity-free operation up to 5 ps/$\sqrt{\text{km}}$ PMD corresponding to a DGD up to 22.36 ps for a 100 Gb/s 20-km link in the optical access context. We have also shown that even though the presence of CD increases the number of singularities compared to when the only channel impairment is PMD, the CA-CMA equalizer, when well configured with reliable parameters, is able to reduce the number of singularities, in the presence of both CD and PMD, to levels comparable to and even lower than what the standard CMA achieves in a PMD-only context. Moreover, the weaknesses of MU-CMA and CA-CMA that prevent obtaining even lower number of singularities, than what has been presented, over the range of PMD considered have been identified, and new ideas have been suggested for improvement. Otherwise, since CMA is well suited for constant envelope modulation, we have studied QPSK modulation. Of key interest would be to further consider more advanced modulation formats as Quadrature Amplitude Modulation (QAM). This will be an interesting direction to investigate in a future work.

CHAPTER 3

An advanced CA-CMA for wide-range PMD mitigation

Strive not to be a person of success but a person of value
— Albert Einstein

Contents

3.1 Introduction

Digital coherent detection [39, 95] has attracted attention for optical access [96, 97, 104] since it allows high aggregated capacity beyond 100 Gbps thanks to the use of multi-dimensional modulation formats and digital equalization of impairments such as chromatic dispersion (CD) and polarization mode dispersion (PMD). PMD varies in time, so it requires adaptive equalizers that track the time variation of the channel. In this context, because of its robustness against various channel characteristics, Constant Modulus Algorithm (CMA) that is a blind multiple-input multiple-output equalizer [83, 98] has been considered for optical fibre transmission performing in a single operation, polarization demultiplexing and PMD compensation [94, 93, 84, 99].

However, the polarization demultiplexing capability of the CMA suffers from singularity [39] issues as the two polarization outputs of the equalizer sometimes converge toward the same input polarization signal, so missing the second one. Various techniques have been proposed to mitigate this as in [93] where a constraint against multi-user (MU) i.e. dual polarizations in the optical fiber communication context is added to the CMA cost function.

In line with this idea, in [103], the relationships between the MU-CMA and the channel parameters for singularity avoidance have been studied in details considering deterministic realizations of the optical channel. It resulted into a refined Correlation Avoidance (CA) CMA proposal ensuring zero-singularity working points up to 5 ps/$\sqrt{\text{km}}$ instantaneous PMD values. However, full singularity avoidance could not be achieved over the stringent range of PMD values the optical access system may face i.e. up to 10 ps/$\sqrt{\text{km}}$ instantaneous PMD values [100, 105, 102]. Moreover, it was suggested that among all potential cross-products, only the cross-products that fits the Differential Group Delay (DGD) induced by the PMD should be selected to strengthen the signature of the cross-correlation constraints and thus allow better singularity avoidance over a wider range of PMD.

This chapter investigates this conjecture considering the simulation of a 100 Gbps QPSK transmission system and also proposes, with limited complexity increase, a new self-adaptive CA-CMA scheme that enables efficient CMA singularity avoidance up to 10 ps/$\sqrt{\text{km}}$ instantaneous PMD values. This introduction and the activities, described in the previous sentence, which will be presented in the subsequent sections have been published in [106]. Additionally, the ability of CMA to mitigate chromatic dispersion is examined and potential practical strategies for the DSP configuration are derived.

In the following sections, we briefly present the principle of the CA-CMA. Then we propose a parameterized update equation based on correlation lag sets. We justify the use of the simulation approach for this study and describe the related set-up. At last, we present the results and discuss the behavior of the CA-CMA, coming up with new proposals before concluding.

3.2 CA-CMA principle

Once initialized, we recall that the Finite Impulse Response (FIR) filters $\mathbf{f}_{pq}$ $(p, q \in \{1, 2\})$ of a CMA equalizer are updated by means of a stochastic gradient descent algorithm that minimizes a cost function representative of any deviation from a constant modulus output and which depends on $\mathbf{f}_{pq}$ [83]. CA-CMA, as introduced in section 2.4, adds a constraint to the cost function by introducing the equalizer output signals' cross-correlations to be minimized [93]. Hence, given the equalizer input $\mathbf{y}_{p,q}(k)$, equalizer output $\mathbf{z}_{p,q}(k)$, an averaging window size w, and a correlation lag index δ that indexes the depth of the cross-correlations, the update equations for the CA-CMA are compactly given by Eq. (3.1) [103]

which is the same as Eq. (2.18):

$$\mathbf{f}_{pq}^{(k+1)} = \mathbf{f}_{pq}^{(k)} - 4\mu\{(|z_p(k)|^2 - 1)z_p(k)\overline{\mathbf{y}}_q(k) + \frac{1}{w^2} \times \sum_{\substack{n=1 \\ n\neq p}}^{2} \sum_{\delta=-\delta_2}^{\delta_2} \sum_{i=k}^{k-w+1} [z_p(i)\overline{z_n}(i-\delta)] \sum_{i=k}^{k-w+1} [z_n(i-\delta)\ \overline{\mathbf{y}}_p(i)]\}. \quad (3.1)$$

The time index, k, in $\mathbf{f}_{pq}^{(k)}$ indicates that the filter coefficients are updated and attain a new value at each iteration time, while for $\mathbf{z}_p(k)$ it indicates the current estimated value of the received symbol $\mathbf{y}_q(k)$ at that time instant.

At 100 Gbps, e.g., generated by a 32 Gbaud dual polarization quadrature phase shift-keying (DP-QPSK) system, in case there is no significant CD (at the zero dispersion wavelength) or in case the CD is compensated otherwise, the typical maximum DGD corresponding to $10\text{ps}/\sqrt{\text{km}}$ PMD spreads the signal over two symbols. Then, to avoid integrating noise, the correlation lag limit, δ_2, should be restricted to this two-symbol period.

This means that the correlation constraints of the CA-CMA introduces the computation of at most 5 additional cross-products when compared to the standard CMA case, while in [93] 19 cross-products were used. The 5 cross-products are due to the fact that a cross-correlation lag (or correlation lag) depth of $\delta_2 = 2$ implies the following possible correlation lag indices {-2, -1, 0, 1, 2} which are indexed by δ. It is possible to come up with special configurations of the CA-CMA equalizer that sample the correlation lags and select specific lags, $\delta \in [-\delta_2, \delta_2]$ for use in the update equation.

We can represent these special configurations of the CA-CMA with a restricted set, $\{{}^N\mathbf{D}_d\}$, containing a single element ${}^N\mathbf{D}_d$ comprising a set of cross-products that build the cross-correlations of depth δ_2 where N is the cardinality of the set and $d = \delta_2$.

The single-element set $\{{}^1\mathbf{D}_0\}$, i.e. $\{0\}$ $(N = 1, d = 0)$, represents the cross-products of the equalizer outputs at the same instant of time i.e., the correlation of a given polarization with the other polarization at the same instant time, the correlation lag index being $\{0\}$; $\{{}^3\mathbf{D}_1\}$ represents a full cross-correlation with a lag of 1 symbol, the correlation lag indices being {-1, 0, 1}; $\{{}^2\mathbf{D}_1\}$ represents a cross-correlation with a lag of 1 symbol but excluding ${}^1\mathbf{D}_0$, the correlation lag indices being {-1, 1}; and $\{{}^3\mathbf{D}_2\}$ represents the cross-products with a lag of 2 symbols but excluding the cross-products $\{{}^2\mathbf{D}_1\}$, the correlation lag indices being {-2, 0, 2}.

This allows to select, among the set of cross-products, a reduced set of cross-products that as suggested in [103], tracks the potential cross-correlations where the maximum of energy is located i.e., at the DGD.

Since the CA-CMA works the same for both polarization tributaries, one of them being late or ahead with respect to the other, symmetric set of cross-products are considered. The update, Eq. (3.1), now depends on the set $\{{}^N\mathbf{D}_d\}$ of cross-products and can be written as given by Eq. (3.2):

$$\mathbf{f}_{pq}^{(k+1|\{{}^N\mathbf{D}_d\})} = \mathbf{f}_{pq}^{(k|\{{}^N\mathbf{D}_d\})} - 4\mu\{(|z_p(k)|^2 - 1)z_p(k)\overline{\mathbf{y}}_q(k) + \frac{1}{w^2} \times \sum_{\substack{n=1 \\ n\neq p}}^{2} \sum_{\delta\in\{{}^N\mathbf{D}_d\}} \sum_{i=k}^{k-w+1} [z_p(i)\overline{z_n}(i-\delta)] \sum_{i=k}^{k-w+1} [z_n(i-\delta)\ \overline{\mathbf{y}}_p(i)]\}. \quad (3.2)$$

Where $\mathbf{f}_{pq}^{(k|\{{}^N\mathbf{D}_d\})}$ means that the filter coefficients (taps) at iteration time index k depend on the set $\{{}^N\mathbf{D}_d\}$. Eq. (3.2) differs from Eq. (3.1) only in the sum over δ.

3.3 Simulation setup

Optical access networks undergo high environmental constraints, e.g., aerial fibres in stormy conditions. Consequently, the mean PMD can vary over a wide range with particular realizations of the PMD that can be as high as 8.7 ps/$\sqrt{\text{km}}$ [100, 105, 102, 103]. These conditions of fast PMD variation are difficult to reproduce in the Lab. Thus, we consider a simulation approach to model a 32 Gbaud dual polarization QPSK transmission link. The simulation set-up is the same as Fig. 2.1 and we recall the system description. A laser in C-band (1550 nm) is split by the polarization beam splitter (PBS) into two orthogonal polarization signals each being modulated by two independent randomly generated data sequences through an in-phase/quadrature (I/Q) modulator to yield the I/Q modulated signals $\mathbf{x}_1(t)$ and $\mathbf{x}_2(t)$. The I/Q transmitted sequences are generated using oversampling ratio of 8, and electronically filtered using a Root Raised Cosine (RRC) filter. Then, the modulated signals $\mathbf{x}_1(t)$ and $\mathbf{x}_2(t)$ are polarization multiplexed by the polarization beam combiner (PBC) and propagated through a standard single mode fibre of length 20 km, typical of the optical access.

The impairments taken into account are the attenuation (0.2 dB/km), the chromatic dispersion (17 ps/nm/km) and the instantaneous differential group delay (DGD) which will be referred to in terms of the corresponding instantaneous PMD.

We then introduce the effects due to attenuation and chromatic dispersion (CD) to the polarization division multiplexed (PDM) signal. Then the polarization rotation mixing effects due to birefringent phase shift, and differential group delay are applied to the orthogonal signals, after which they are again multiplexed by another PBC. A single birefringent element is considered. This permits analysis of specific polarization states and corner cases that lead to singularities. At the receiver, two PBSs split the PDM received signal and a local oscillator (LO) signal at the same wavelength of the transmit laser. These split signals are respectively mixed in two 90° optical hybrids to recover the in-phase and quadrature signal components on both polarization axes. The recovered in-phase and quadrature signal components are then passed on to the digital signal processing (DSP) block where they are RRC filtered and downsampled to 2 samples per symbol. Additive White Gaussian noise (AWGN) is introduced to achieve typical BER of 10^{-4}. Then, a group velocity dispersion compensation stage mitigates chromatic dispersion. Next, the adaptive fractionally spaced equalizer (FSE) compensates for the PMD and performs polarization de-multiplexing. Afterwards, carrier phase estimation (CPE) is performed to mitigate both transmitter and LO phase noise. Finally, hard-decision decoding on the transmitted symbols and bit error rate (BER) calculation are performed.

The simulations were performed with only one random seed value so there may be statistical variability. However, since we perform the simulations based on the most reliable parameters we obtained in the previous chapter, we expect similar reliability performance.

3.4 Results and discussion

The singularity avoidance capability of the CMA and CA-CMA is studied by computing the number of singularity occurrences over 2000 polarization states uniformly distributed on the Poincaré sphere. PMD values are varied for different correlation lag depths δ_2. In section 3.2 we highlighted that for a 32 Gbaud DP-QPSK system, the time spreading of the DGD due to the wide range of values of PMD considered, does not exceed 2 symbol periods. Hence, we limit the value of the correlation lag depth to a maximum of 2 symbols.

Also, considering the most reliable parameters of the CA-CMA that could achieve zero-singularities, i.e. $n_s = 0$, we set the number of taps and the window size as $L = 13$

and $w = 40$ respectively [103]. This gives a total of 121 possible combinations of channel and equalizer parameters. The algorithms are initialized in a common way by setting the weight of the center tap to unity and the weight of all other taps to zero.

Fig. 3.1 shows the singularity signature for the basic CMA, the CA-CMA with different selections of cross-products — a full cross-correlation with correlation lag depths δ_2 spanning [0:10], a one-sided cross-correlation $\delta_2 = 18$ i.e. {0:18} giving what was proposed in [93], and specific cross-products from the set $\{^N\mathbf{D}_d\}$ as defined in section 3.2.

At first, Fig. 3.1 confirms that the full cross-correlation with a lag greater than the maximum DGD (i.e., $\delta_2 > 2$ which includes the lag of 18 as proposed in [93]), leads to a number of singularities that is always greater than 20, working worse than basic CMA over this δ_2 domain. Then, one observes that the configurations that include the cross-product with no relative delays i.e. $\delta_2 = 0$, provide zero or very few singularities up to 5 ps/$\sqrt{\text{km}}$ for $^1\mathbf{D}_0$, up to 7 ps/$\sqrt{\text{km}}$ for $^3\mathbf{D}_1$ while not working as well as $^1\mathbf{D}_0$ over 0 to 5 ps/$\sqrt{\text{km}}$, and $^3\mathbf{D}_2$ over 9 to 10 ps/$\sqrt{\text{km}}$ working better than both $^1\mathbf{D}_0$ and $^3\mathbf{D}_1$ in this PMD range. Otherwise, Fig. 3.1 shows that over the full range of PMD, $^2\mathbf{D}_1$ produces several tens of singularities being always worse than $^3\mathbf{D}_1$ including when there is no PMD (i.e. PMD value of zero). An interpretation could be that whatever the PMD is, still, the CA-CMA has to perform polarization demultiplexing which, independent of PMD, is necessary since the polarization axes of the transmitter are not *a priori* the same as the axes of the receiver.

We also see from Fig. 3.1 that, as suggested in [103], when the instantaneous PMD value increases, i.e. the DGD increases, the configuration that performs better is the configuration that keeps the cross-products at $\delta = 0$ while retaining only those other cross-products delayed by the DGD. Hence, the total number of cross-products is further reduced to at most 3.

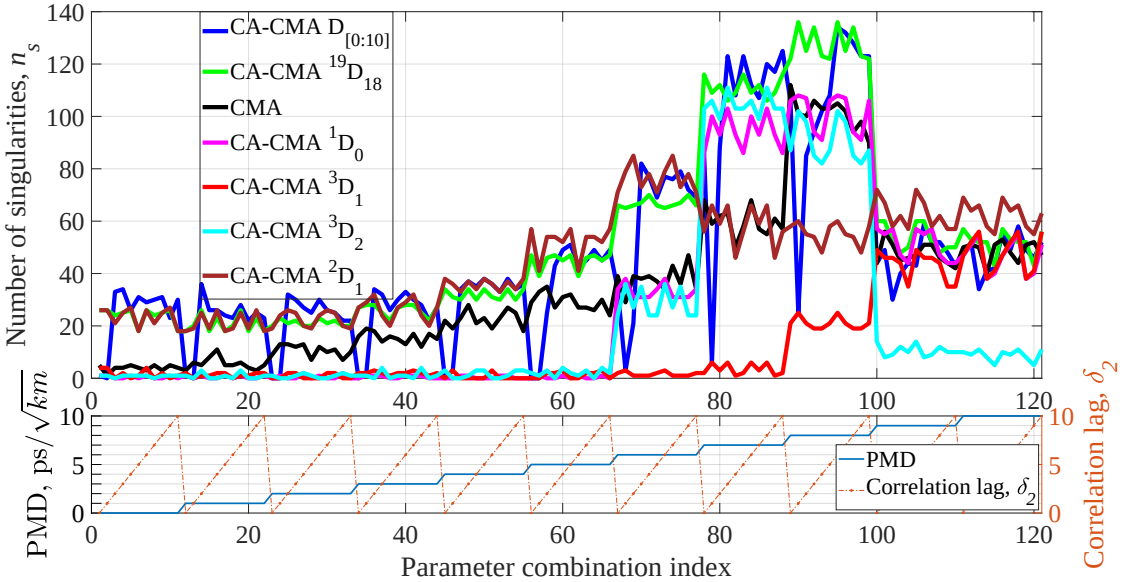

Figure 3.1: Singularity signature for CMA, CA-CMA $\mathbf{D}_{0:10}$, $^{19}\mathbf{D}_{18}$,$^1\mathbf{D}_0$, $^3\mathbf{D}_1$, $^3\mathbf{D}_2$, $^2\mathbf{D}_1$

This is clearly seen in Fig. 3.2, which is a plot of the evolution of the strength $C^{(k)}_{\{^N\mathbf{D}_d\}}(\delta)$ of the cross-products according to the number of iterations, k, i.e. according to time, at a DGD value of 7 ps/$\sqrt{\text{km}}$.

$C^{(k)}_{\{^N\mathbf{D}_d\}}(\delta)$ is defined as the correlation energy, i.e. the square of the absolute value of a cross-product set (or sampled cross-correlation vector) $\{-\delta_2, 0, \delta_2\}$ at a given iteration

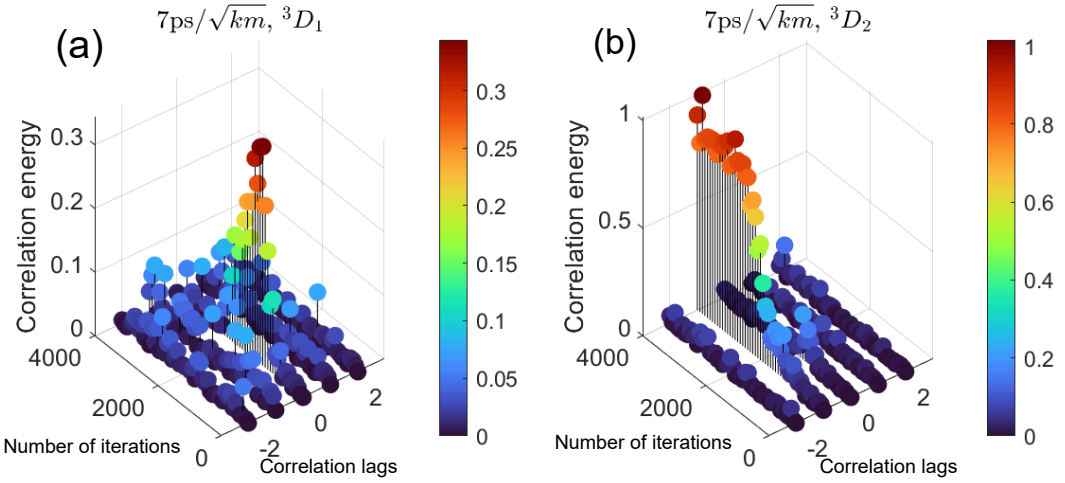

Figure 3.2: Evolution of the correlation energy at a PMD of 7 ps/$\sqrt{\text{km}}$ for (a) ${}^3\mathbf{D}_1$ CA-CMA and (b) ${}^3\mathbf{D}_2$ CA-CMA.

index, k, and is given by Eq. (3.3).

$$C^{(k)}_{\{{}^N\mathbf{D}_d\}}(\delta) = \left| \sum_{i=k}^{k-w+1} [z_p(i)\overline{z_q}(i-\delta)] \right|^2 \text{, where } \delta \in \{-\delta_2, 0, \delta_2\} \tag{3.3}$$

Its dependence on N and d is a way of keeping track of the energy for different sets. After few 100's of iterations, a cross-correlation of a given magnitude rises at a lag that corresponds to this DGD i.e. about 1 time symbol lag. In this situation, ${}^3\mathbf{D}_1$ configuration is able to feed back this error signal to the equalizer and the cross-product energy at this lag ($\delta = \pm\delta_2$) then vanishes as the iteration advances, since the equalizer is properly tuned to match the DGD. This is not the case for ${}^3\mathbf{D}_2$ configuration where the cross-products at $\delta = 1$ continues to increase as the iteration advances leading to a higher probability of singularity as observed in Fig. 3.1.

Fig. 3.3, Fig. 3.4, and Fig. 3.5 show the evolution of the correlation energy for specific sets of cross-products ${}^1\mathbf{D}_0$, ${}^3\mathbf{D}_1$, and ${}^3\mathbf{D}_2$ at PMD values [0, 2, 4, 6, 7, 8, 9] ps/$\sqrt{\text{km}}$. They are plots similar to Fig. 3.2 when Fig. 3.2 is viewed from the top.

Each row of figures represents a particular PMD value while each column of figures represents a particular cross-product set. We can see in Fig. 3.3, which shows the cross-correlation energy at PMD values of 0-, 2-, and 4 ps/$\sqrt{\text{km}}$, that the cross-correlation energy increases to a maximum value as the iteration progresses after which it diminishes. This event is restricted to the correlation lag index, $\delta = 0$ for the sets of cross-products considered.

In Fig. 3.4 which shows the cross-correlation energy at PMD values of 4-, 6-, and 7 ps/$\sqrt{\text{km}}$, we can see that for a PMD value of 6 ps/$\sqrt{\text{km}}$ the cross-correlation energy increases with the iterations for cross-product sets ${}^1\mathbf{D}_0$ and ${}^3\mathbf{D}_2$ without decreasing and has this event restricted to a correlation lag index $\delta = -1$, while it increases to a maximum and then decreases afterwards for the cross-product set ${}^3\mathbf{D}_1$. For a PMD value of 7 ps/$\sqrt{\text{km}}$ the cross-correlation energy increases with the iterations without decreasing afterwards and has this event restricted to $\delta = -1$ for the cross-product set ${}^3\mathbf{D}_2$. For ${}^3\mathbf{D}_1$, the cross-correlation energy increases and then decreases afterwards, and has this event restricted to $\delta = 0$, while for ${}^1\mathbf{D}_0$ the cross-correlation energy is distributed across the correlation lags and does not show a continuous increase with the iterations.

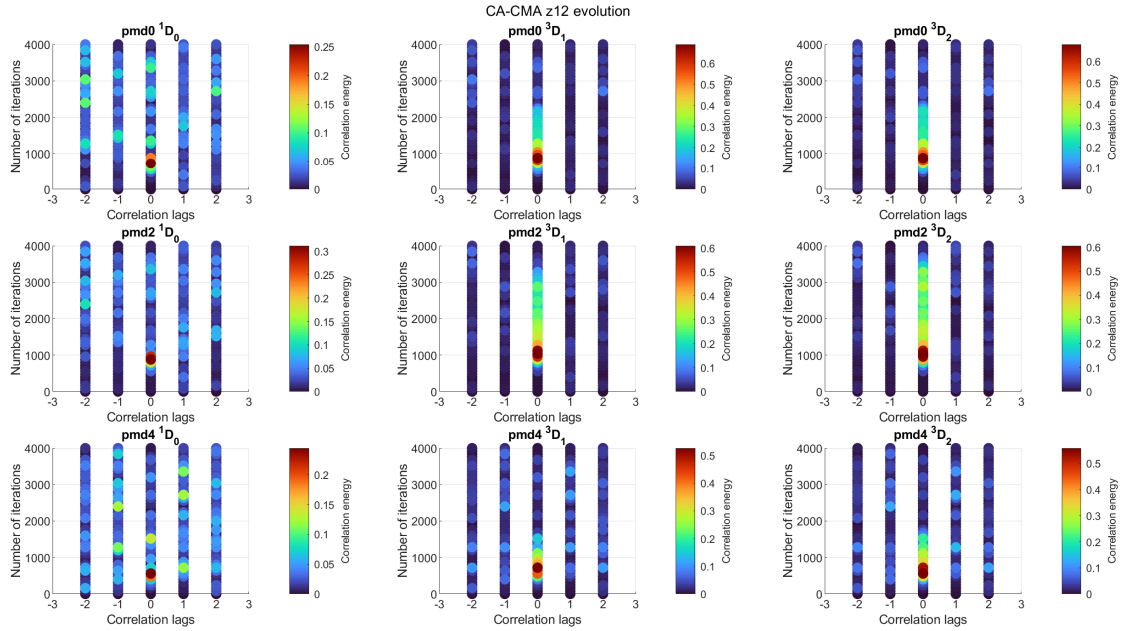

Figure 3.3: Correlation energy for $^1\mathbf{D}_0$ CA-CMA, $^3\mathbf{D}_1$ CA-CMA and $^3\mathbf{D}_2$ CA-CMA at PMD of 0-, 2- and 4 ps/$\sqrt{\text{km}}$

In Fig. 3.5 which shows the cross-correlation energy at PMD values of 7-, 8-, and 9 ps/$\sqrt{\text{km}}$, we can see that at PMD values of 8 and 9 ps/$\sqrt{\text{km}}$, the cross-correlation energy increases with the iterations for cross-product sets $^1\mathbf{D}_0$ and $^3\mathbf{D}_2$. While this increase is restricted to $\delta = 1$ at PMD of 8 ps/$\sqrt{\text{km}}$, it is not restricted to any particular value of δ at PMD of 9 ps/$\sqrt{\text{km}}$. We can also see that for the set $^3\mathbf{D}_1$, at 8 ps/$\sqrt{\text{km}}$, the cross-correlation energy diminishes after attaining a maximum at $\delta = 1$.

The results above show that we can retrieve the DGD information from the magnitude of the cross-correlation energy at a correlation lag, δ, that corresponds to the actual DGD, with $d = |\pm\delta_2|$, when the right set of cross-products $^3\mathbf{D}_d = \{-\delta_2, 0, \delta_2\}$ for a given PMD range are selected. It is important to note that we can retrieve this DGD information at the said value of $d = |\pm\delta_2|$ due to the symmetric nature of the cross-correlation.

This then provides a means to use the cross-correlation energy information $C^{(k)}_{\{^N\mathbf{D}_d\}}(\delta)$ to derive a metric, $C^{(k)}_{switch}(\delta)$, which can enable adaptive operation of the CA-CMA across a wide PMD range. Such kind of adaptive operation will lead to a singularity signature that is a combination the singularity signatures of the best performing configurations of the CA-CMA that have been presented in Fig. 3.1, for the wide range of PMD considered. Still looking at Fig. 3.1, we would then expect such an adaptive algorithm to work in the configuration $^3\mathbf{D}_1$ in the PMD range 0 – 8 ps/$\sqrt{\text{km}}$, and then switch to the configuration $^3\mathbf{D}_2$ in the PMD range 9 – 10 ps/$\sqrt{\text{km}}$ as these are the best cases that lead to minimum number of singularities, n_s not exceeding 20, over the PMD range considered.

This metric for switching the operation of the CA-CMA, $C^{(k)}_{switch}(\delta)$, is defined as the vector sum of the cross-correlation energy $C^{(k)}_{\{^N\mathbf{D}_d\}}(\delta)$ over a number of iterations, $\hat{n}$, and is given by Eq. (3.4). The value of $\hat{n}$ has to be large enough for the cross-correlation constraint to retrieve meaningful correlation information from the equalizer output signals.

$$C^{(k)}_{switch}(\delta) = \sum_{k}^{\hat{n}} \left| \sum_{i=k}^{k-w+1} [z_p(i)\overline{z_q}(i-\delta)] \right|^2, \text{where } \delta \in \{-\delta_2, 0, \delta_2\} \tag{3.4}$$

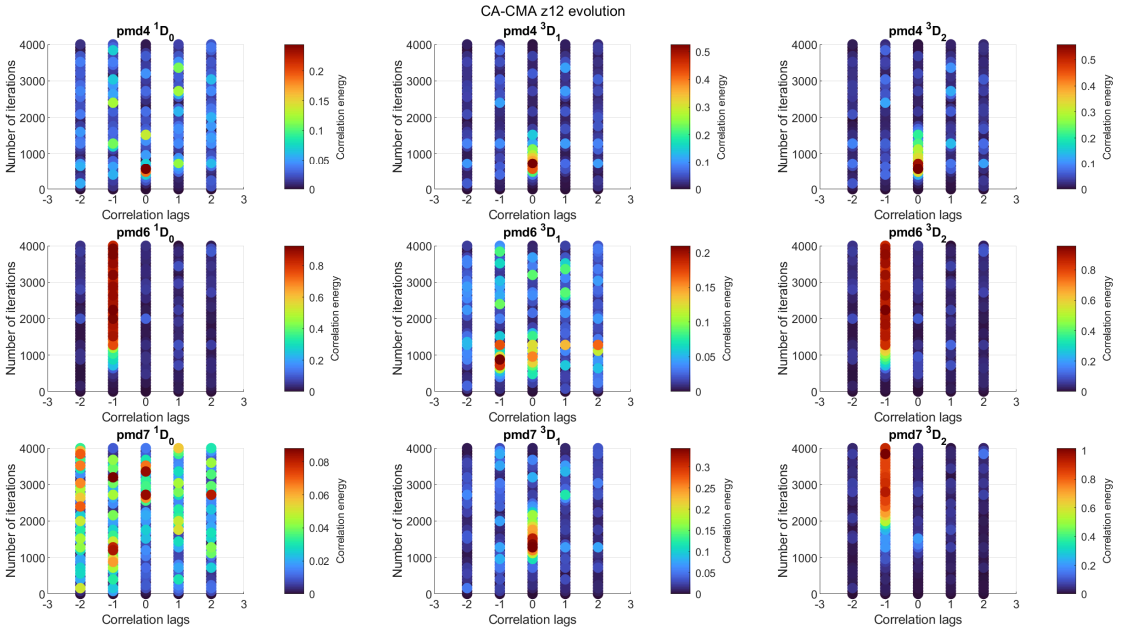

Figure 3.4: Correlation energy for $^1\mathbf{D}_0$ CA-CMA, $^3\mathbf{D}_1$ CA-CMA and $^3\mathbf{D}_2$ CA-CMA at PMD of 4-, 6- and 7 ps/$\sqrt{\text{km}}$

We thus propose a self-adaptive CA-CMA that considers the strength of the cross-products of different relative delay to input the proper one into the update equation of the CA-CMA. This adaptive CA-CMA is restricted to $^1\mathbf{D}_0$ configuration at initialization to enable proper polarization demultiplexing while $C^{(k)}_{switch}(\pm 1)$, or $C^{(k)}_{switch}(\pm 2)$, are then evaluated and compared to $C^{(k)}_{switch}(0)$ to switch to either $^3\mathbf{D}_1$ or $^3\mathbf{D}_2$. It is important to state that the configurations $^1\mathbf{D}_0$, $^3\mathbf{D}_1$, and $^3\mathbf{D}_2$ indicate the selection of cross-products that are fed back to the update equations. To compute $C^{(k)}_{switch}(\delta)$, we retrieve the correlation lags corresponding to a configuration $^5\mathbf{D}_2$ (i.e. {-2,-1,0,1,2}) which is a union of the cross-products — $^1\mathbf{D}_0$, $^3\mathbf{D}_1$, and $^3\mathbf{D}_2$ — that are selected and fed back to the update equations.

The switching criterion is presented in Algorithm 1. The two-times oversampled received signal is the input to three configurations of the CA-CMA, $\{^1\mathbf{D}_0, ^3\mathbf{D}_1, ^3\mathbf{D}_2\}$, depending on the state of the flags, $f_{\{^N\mathbf{D}_d\}}$, which are used to select a given configuration when assigned a value of 1. The flags are initialized to 1, and the number of iterations $\hat{n}$ sufficient to retrieve cross-correlation information is set to 1500 (i.e. 1500 symbols which corresponds to a time length of 47 ns). The maximum number of iterations for the CA-CMA adaptation is set to N_{iter}. The adaptation cycle begins and the switching metric $C^{(k)}_{switch}(\delta)$ is computed for the configuration $^1\mathbf{D}_0$ only. This means that among the $^5\mathbf{D}_2$ full cross-correlations retrieved for the metric, a selection $^1\mathbf{D}_0$, is fed back to the update equations at each iteration index, k. The three configurations of the CA-CMA $\{^1\mathbf{D}_0, ^3\mathbf{D}_1, ^3\mathbf{D}_2\}$ run consecutively until $k = \hat{n}$. Then the vector of cross-correlation lags in $C^{(k)}_{switch}(\delta)$ is retrieved and the condition for switching to either of the configurations of the CA-CMA is evaluated. We can represent the retrieved correlation lag indices {-2,-1,0,1,2} as $\{\delta^{(-2)}, \delta^{(-1)}, \delta^{(0)}, \delta^{(1)}, \delta^{(2)}\}$ where $\delta^{(\cdot)}$ represents the value of the lag at the particular lag index. With this representation, we can now locate the position of the PMD-induced DGD. As noted earlier, $C^{(k)}_{switch}(\delta)$ is able to retrieve the cross-correlation energy and the location of this energy is at the correlation lag index that corresponds

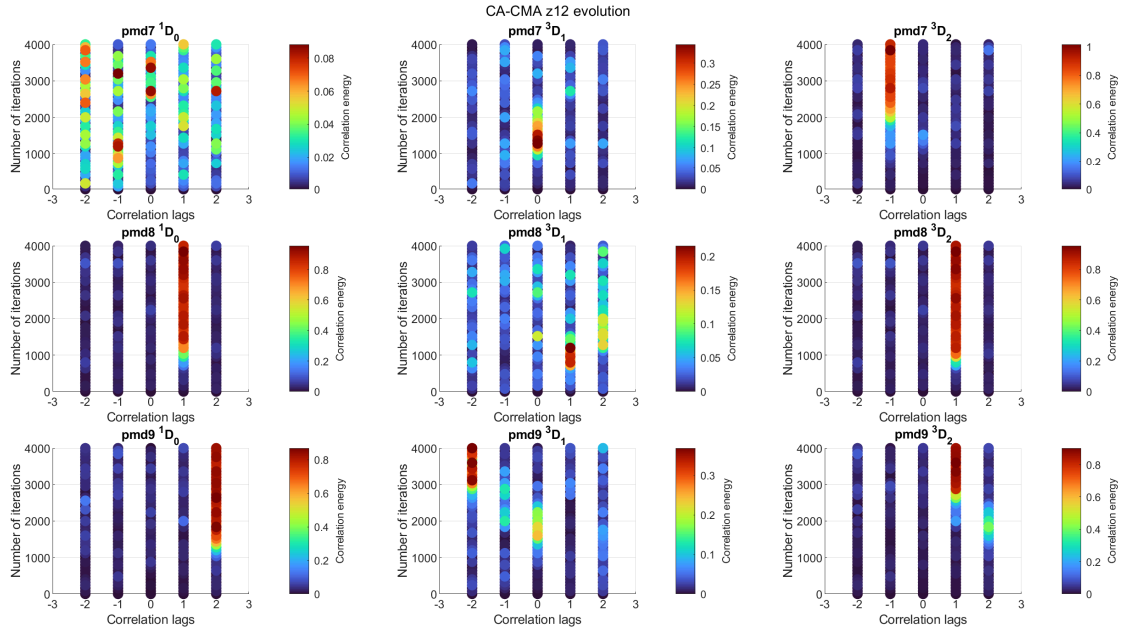

Figure 3.5: Correlation energy for $^1\mathbf{D}_0$ CA-CMA, $^3\mathbf{D}_1$ CA-CMA and $^3\mathbf{D}_2$ CA-CMA at PMD of 7-, 8- and 9 ps/$\sqrt{\text{km}}$

to the symbol time spreading of the DGD. The correlation lag index with the maximum energy is selected, and it specifies the value of the proper cross-correlation lag depth, δ_2. Hence, the corresponding flag $f_{\{^N\mathbf{D}_d\}}$, with $d = \delta_2$, is set to 1, and all other flags are set to 0. This means that the proper configuration of the CA-CMA has been selected while the other configurations have been discarded. The CA-CMA then continues running with this proper configuration until a stopping (or convergence) criterion is triggered. In this case we use the same stopping criterion as in section 2.5.1. The threshold for the stopping criterion was reached after less than 3200 iterations which corresponds to a time length of 100 ns.

The results of this adaptive algorithm is presented in Fig. 3.6 where we can see that it provides the best of the $^1\mathbf{D}_0$, $^3\mathbf{D}_1$ and $^3\mathbf{D}_2$ CA-CMA configuration performance leading to 7dB (i.e. a factor of 5 difference in the average level of singularities) improvement in singularity avoidance compared to other schemes.

This would guarantee proper PMD mitigation over the wide range of instantaneous PMD realization the optical access could face with limited complexity as compared to basic CMA that is already considered as a low-complexity scheme. Here, interestingly, Fig. 3.2 gives also insight of the ability of CA-CMA to provide fast estimation and equalization, since it is already able to account for the cross-correlation of the PMD channel within about 47 ns without considering related optimization e.g. dynamic step size optimization. The objective set in [54] for 50G-PON as preamble length for equalization is 153 ns with a worst case value of 610 ns. As the line rate increases the preamble objective also increases. At 100 Gbps and we achieve a total of 147 ns for equalization with CA-CMA without optimization. We note that the results presented here consider PMD only because we used a group velocity dispersion compensation stage (GVD) to mitigate chromatic dispersion. It is worth noting however that CMA-like algorithms still have the ability to mitigate CD. In this case, the approach proposed in this section to track the DGD, induced by the PMD, through a selection of 3 cross-products has to be amended since CD would disperse the energy. Hence, a more common cross-correlation constraint that has the ability to sense

Algorithm 1 PMD-Adaptive CA-CMA

Algorithm parameters: configurations – $\{^1\mathbf{D}_0, ^3\mathbf{D}_1, ^3\mathbf{D}_2\}$, number of iterations – N, decision point – $\hat{n}$, *input*

$f_{\{^1\mathbf{D}_0\}} \leftarrow 1$, $f_{\{^3\mathbf{D}_1\}} \leftarrow 1$, $f_{\{^3\mathbf{D}_2\}} \leftarrow 1$, $\hat{n} \leftarrow 1500$
for $k \leftarrow 1$ **to** N_{iter} **do** ▷ loop from 1 to N_{iter}
    if ($f_{\{^1\mathbf{D}_0\}} = 1$) **then**
        $C^{(k)}_{\{^1\mathbf{D}_0\}}(\delta) \leftarrow \text{CA-CMA}_{\{^1\mathbf{D}_0\}}(input)$
        $C^{(k+1)}_{switch}(\delta) \leftarrow C^{(k)}_{switch}(\delta) + C^{(k)}_{\{^1\mathbf{D}_0\}}(\delta)$ ▷ compute metric
    end if
    if ($f_{\{^3\mathbf{D}_1\}} = 1$) **then**
        $\text{CA-CMA}_{\{^3\mathbf{D}_1\}}(input)$
    end if
    if ($f_{\{^3\mathbf{D}_2\}} = 1$) **then**
        $\text{CA-CMA}_{\{^3\mathbf{D}_2\}}(input)$
    end if
    if $k = \hat{n}$ **then** ▷ evaluate metric
        $corrLagSet \leftarrow C^{(k)}_{switch}(\delta)$
        if ($\delta^{(0)} = \max(corrLagSet)$) **then**
            $f_{\{^1\mathbf{D}_0\}} \leftarrow 1$, $f_{\{^3\mathbf{D}_1\}} \leftarrow 0$, $f_{\{^3\mathbf{D}_2\}} \leftarrow 0$
        else
            if ($\max(\delta^{(-1)}, \delta^{(1)}) > \max(\delta^{(-2)}, \delta^{(2)})$) **then**
                $f_{\{^1\mathbf{D}_0\}} \leftarrow 0$, $f_{\{^3\mathbf{D}_1\}} \leftarrow 1$, $f_{\{^3\mathbf{D}_2\}} \leftarrow 0$
            else if ($\max(\delta^{(-1)}, \delta^{(1)}) < \max(\delta^{(-2)}, \delta^{(2)})$) **then**
                $f_{\{^1\mathbf{D}_0\}} \leftarrow 0$, $f_{\{^3\mathbf{D}_1\}} \leftarrow 0$, $f_{\{^3\mathbf{D}_2\}} \leftarrow 1$
            end if
        end if
    end if
    if (convergence criterion $\leq$ threshold) **then** ▷ convergence criterion
        break
    end if
end for

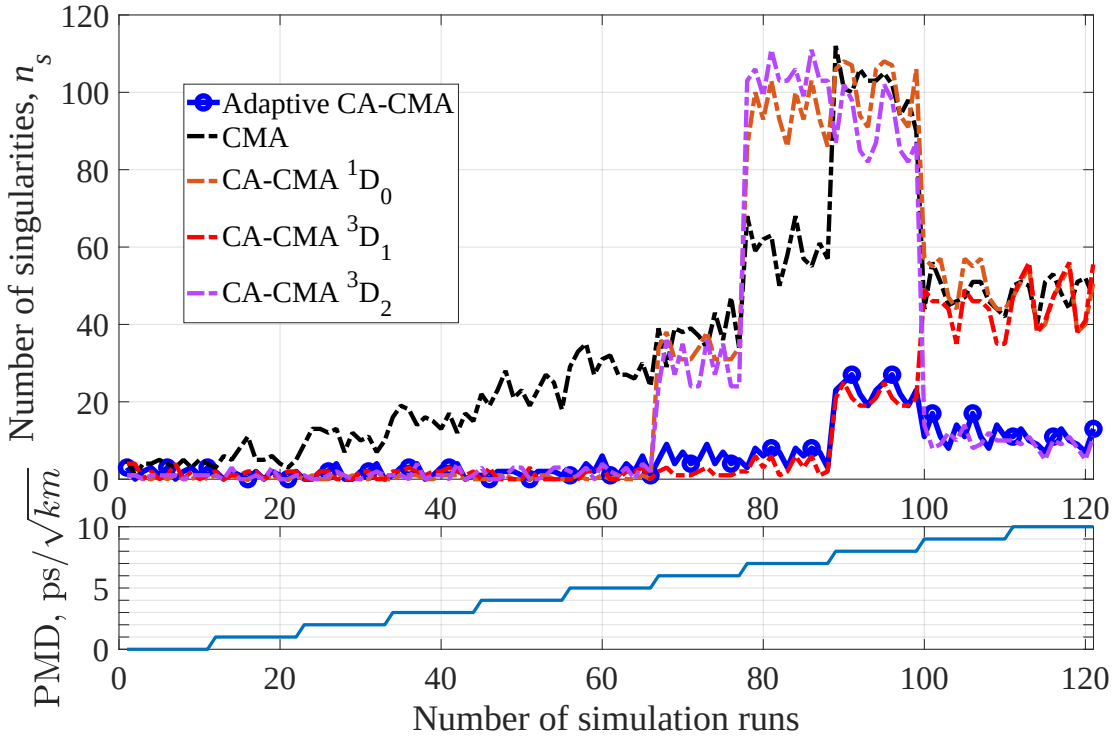

Figure 3.6: Singularity signature for Adaptive CA-CMA, CMA, $^1\mathbf{D}_0$ CA-CMA, $^3\mathbf{D}_1$ CA-CMA and $^3\mathbf{D}_2$ CA-CMA

the channel in a continuous way would have to be used instead to avoid singularity and would probably induce more algorithm complexity. The question would then be to check if this option would be still less complex overall than the option considered in this section where CD and PMD have been mitigated separately. These points are investigated in the next section.

3.4.1 CA-CMA tolerance to CD + PMD

To investigate the performance of this adaptive CA-CMA when subjected to both CD and PMD impairments, we follow the procedure as described in section 3.4 where we subject the CA-CMA algorithm to different polarization states and PMD, including CD variations this time around. We considered the same 2000 polarization states uniformly distributed over the Poincaré sphere (as in section 3.4) and chromatic dispersion values dictated by the dispersion parameter, D, which we vary in the range from 0 to 17 ps/nm/km. The limit of 17 ps/nm/km for the dispersion parameter corresponds to the dispersion parameter value in C-band for the standard single mode fiber.

Another way to vary the CD is to alter the fiber length, but in this case, the spreading due to the PMD will also be altered, and we will have the two impairments varying simultaneously. In order to compare the CA-CMA singularity avoidance capability when PMD alone is considered, with the case of when CD and PMD are both considered, we keep the fiber length fixed, and then vary the CD parameter.

As already seen in subsection 2.5.3 and particularly from Fig. 2.7, there exist working points for which the CA-CMA in the presence of both CD and PMD can achieve lower n_s than both the standard CMA and the proposal of [93] when subjected to both CD and PMD. Notably some working points of the CA-CMA achieve a lower n_s, in the CD and

PMD case, than the standard CMA when the latter is subjected to only PMD.

Fig. 2.7 already gives an insight to the performance of specific configurations of the CA-CMA in the limit of the dispersion parameter D of value 17 ps/nm/km. When the adaptive CA-CMA is subjected to both CD and PMD at this limit of the dispersion parameter, we would therefore expect that it would not perform as efficiently as it did in the PMD-only scenario of Fig. 3.6

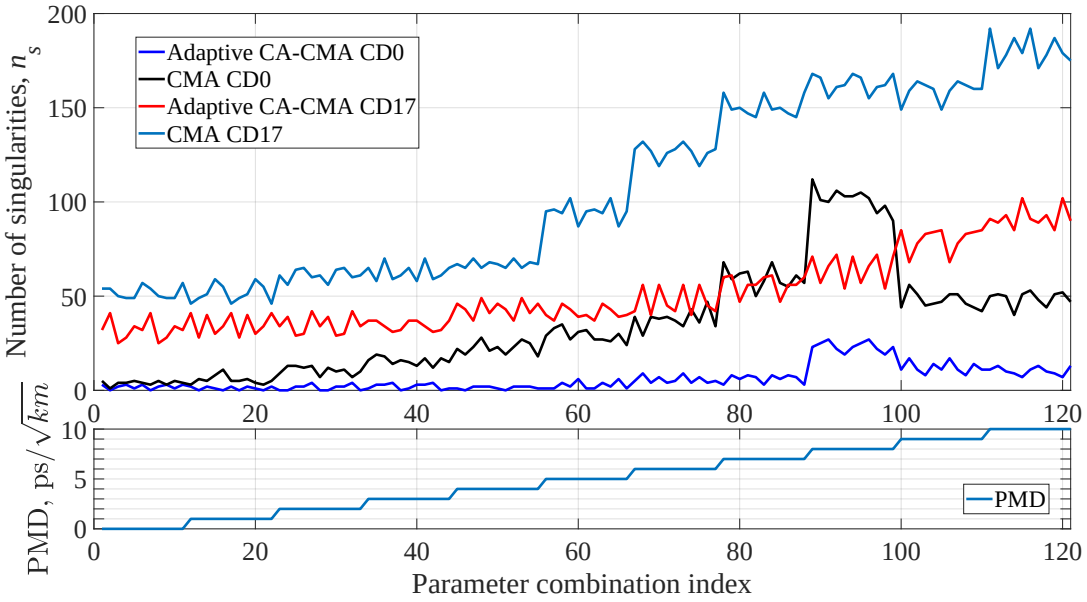

Figure 3.7: CA-CMA in the presence of both CD (D = 17 ps/nm/km) and PMD

We present, in Fig. 3.7, the plot of the adaptive CA-CMA subjected to both CD and PMD. As usual, the notation in the legend CD0 or CD17 specifies the dispersion parameter value. In this plot we also show the standard CMA for the PMD-only case (CMA CD0) and the CD + PMD case (CMA CD17); the adaptive CA-CMA for the PMD-only case (Adaptive CA-CMA CD0) and the CD + PMD case (Adaptive CA-CMA CD17). From the plots for Adaptive CA-CMA CD17 and Adaptive CA-CMA CD0, we can see that the adaptive CA-CMA with D= 17 ps/nm/km does not work as efficiently as when D = 0 ps/nm/km, with the difference in n_s between the two reaching, on average, a factor of 4. This worse performance under high CD is expected due to the additional spreading induced by the CD. However, we can see that it clearly achieves a lower n_s than the standard CMA with D = 17 ps/nm/km across all the range of PMD considered. It is also able to achieve better performance in the PMD range of 7-8 ps/$\sqrt{\text{km}}$ than the standard CMA (CMA CD0) facing a simpler case of PMD alone.

It was highlighted in subsection 2.5.4 that the increase in n_s when CD and PMD are acting together is due to the CD-induced ISI that worsens the strength of the cross-correlations. It was also proposed that it could be possible to obtain lower values of n_s if the cross-correlations can be sampled (leading to specific cross-products) and computed in such a way as to avoid a great portion of ISI-impaired symbols and selecting only the symbols for which there is limited effect of the ISI.

However, it would be interesting to see how the adaptive CA-CMA algorithm responds in n_s to a variation in the CD between the upper and lower D limits of 0- and 17 ps/nm/km respectively. We can investigate for the values of D = 8, 10, 14 ps/nm/km which correspond to symbol spread of 4-, 5-, and 7 symbol periods respectively.

Fig. 3.8 presents the result of this investigation. Again the legend indicates the value of the dispersion parameter as the numeric value right next to the 'CD' notation. We can see that the adaptive CA-CMA curves CD8 – CD14 have n_s values that lie between the n_s values achieved by the upper and lower limits for the adaptive CA-CMA i.e. CD17 and CD0 respectively. For the adaptive CA-CMA CD14 curve, it has similar n_s performance to the adaptive CA-CMA CD0 curve in the PMD region 0 – 3 ps/$\sqrt{\text{km}}$, and the n_s performance transitions towards the adaptive CA-CMA CD17 curve as the PMD increases achieving similar performance to the adaptive CA-CMA CD17 in the PMD range 8 – 10 ps/$\sqrt{\text{km}}$. The adaptive CA-CMA curves CD8 and CD10 show an overall similar performance and have values of n_s that are similar to the adaptive CA-CMA CD0 in the PMD range 0 – 5 ps/$\sqrt{\text{km}}$. Their n_s values deviate from the adaptive CA-CMA CD0 curve by about a factor of 2 for the PMD range 6 – 10 ps/$\sqrt{\text{km}}$. Even though the adaptive CA-CMA CD8 and CD10 curves show similar n_s behavior, we note that at 8 ps/$\sqrt{\text{km}}$ the dynamic range of the CD10 curve is higher than that of the CD8 curve by a factor of 2, and at 10 ps/$\sqrt{\text{km}}$, the dynamic range of the CD8 curve is higher than that of the CD10 curve by a factor of 4. For these two curves, it implies that the switching criterion $C^{(k)}_{switch}(\delta)$ still works, although with reduced sensitivity because of the CD-induced ISI which degrades the strength of the cross-correlations and cross-products. For the adaptive CA-CMA CD14, the switching criterion no longer works well as the CD-induced ISI is increased and the strength of the cross-correlations and cross-products are further degraded.

This further motivates the conjecture that it could be possible to obtain lower values of n_s if the cross-correlations can be sampled (leading to specific cross-products) and computed in such a way as to avoid a great portion of CD ISI-impaired symbols, selecting only the symbols for which there is limited or no effect of the CD-induced ISI. The convergence time in this CD + PMD case did not change compared to the PMD-only case.

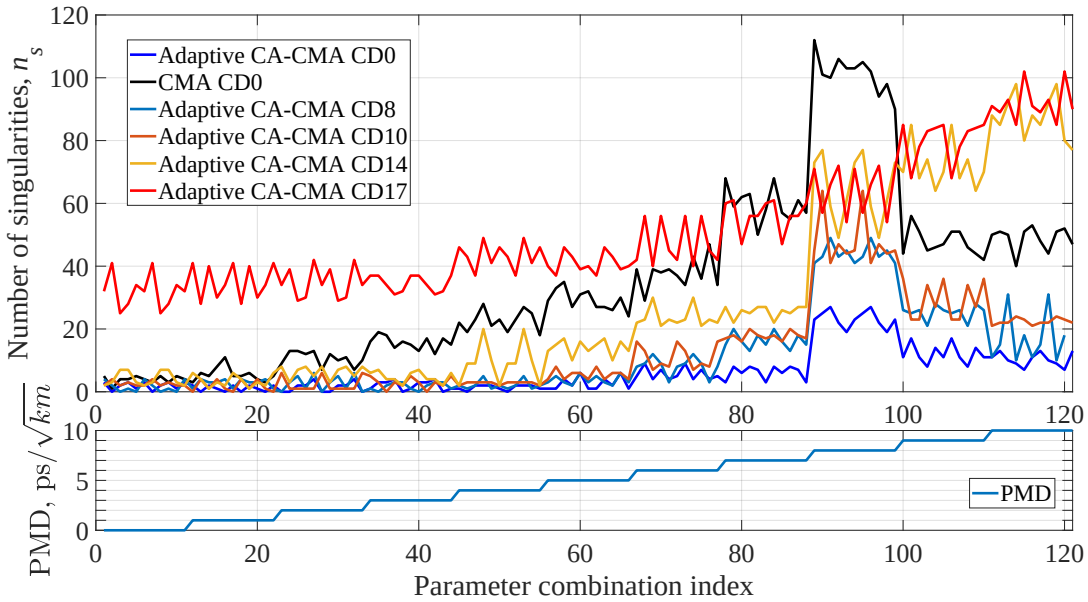

Figure 3.8: CA-CMA in the presence of both CD (D = 0 - 17 ps/nm/km) and PMD

3.5 Conclusion

This chapter proposes a new adaptive CA-CMA that allows proper polarization separation and PMD mitigation achieving efficient CMA singularity avoidance over a wide range of PMD realizations. On average, when mitigating PMD alone, it performs 7 dB better than basic CMA with no significant additional complexity. It also has the ability to converge in about 147 ns and the potential to mitigate CD. The CD mitigation capability and singularity avoidance have also been jointly studied and the adaptive CA-CMA, on average over the PMD range considered, has a similar performance to the basic CMA when the basic CMA is handling PMD alone. This highlights the robustness and the capability of the adaptive CA-CMA to CD mitigation and singularity avoidance. This dual-impairment handling capability can significantly reduce the DSP requirement of a standalone CD mitigation section. The ability to converge fast with no additional increase in complexity but robustly against PMD variability with or without CD can be of importance for the optical access opening room for future studies. It already meets the burst-mode operation preamble objective for equalization in high-speed PON. Particularly, depending on the architecture and the technology utilized in the optical access, the adaptive CA-CMA can reduce the DSP CD mitigation requirement for systems deployed in the C-band where CD can be high.

Conclusions and perspectives

No discipline seems pleasant at the time, but painful. Later on, however, it produces a harvest of righteousness and peace for those who have been trained by it.

— Hebrews 12:11

Conclusions

The optical access network (OAN) will definitely evolve in the next couple of years to support current and evolving needs for differentiated services in industry 4.0 such as transportation (e.g. intelligent transport systems/ train control), mobile front-haul or back-haul, intra- and inter-plant networks, cloud virtual reality (VR), augmented reality (AR), e-learning, e-health (e.g. telesurgery, AR field medical support), online gaming (e.g. holographic communication, immersive extended reality), internet of senses, etc.

These services will require very high data rates, low latency, low jitter, and low packet loss. The system would also need to support very high densification as well as different degrees of node consolidation, enable integrated fixed and wireless networks, achieve interoperability, backward compatibility, and scalability.

The envisioned future OAN that will support these wide range of requirements will have to employ DSP and coherent detection which is not used in the currently deployed systems. They will also have to handle burst-mode operation due to the asymmetric nature of the optical access. Hence a key issue to be addressed in all cases is the latency.

In this thesis, we addressed the issue of latency from the DSP point of view focusing on the adaptive equalization which can impact the latency requirement. Furthermore, considering the environmental deployment scenario of the OAN which can lead to a wide range of polarization mode dispersion (up to 8 ps/$\sqrt{\text{km}}$), and considering that the increase of PMD leads to increased convergence problems for a robust adaptive CMA equalizer, we have proposed an adaptive correlation-avoidance constant modulus algorithm (CA-CMA) equalizer for singularity avoidance over a wide range of polarization mode dispersion (PMD) which covers the PMD range expected in the OAN.

We also analyze the robustness of the CA-CMA across a wide range of PMD (0 - 10 ps/$\sqrt{\text{km}}$) and varying polarization rotation states over a wide range covering the Poincaré sphere for each PMD value. In these cases, the properly tuned CA-CMA can achieve, with high probability, zero singularities in a CD-compensated transmission scenario within the PMD range of (0 - 5 ps/$\sqrt{\text{km}}$) for a 100 Gbps (i.e. 32 GBaud DP-QPSK) coherent transmission system. It can also achieve minimal singularities, being about 7 dB better, compared to the standard CMA and the existing correlation-based schemes across the 0 - 10 ps/$\sqrt{\text{km}}$ PMD range.

In a CD-uncompensated transmission scenario, where the CA-CMA equalizer jointly compensates for CD and PMD, the properly tuned CA-CMA can achieve zero singularities in the 0 - 5 ps/$\sqrt{\text{km}}$ PMD range for a maximum CD corresponding to 160 ps/nm. For higher values of CD, the CA-CMA can achieve minimal singularities, being at least 2 dB better, compared to the standard CMA and the existing correlation-based CMA up to a maximum CD corresponding to 200 ps/nm.

Moreover the advanced CA-CMA can sense the PMD spreading of the channel even in the presence of a CD of up to 200 ps/nm within about 47 ns, and converge in about 100 ns. This makes a total of about 147 ns for its operation in any range of PMD expected in the OAN. This value is already below the objective set for burst-mode operation in 50G-PON [54]. The CA-CMA is also less complex than the existing correlation-based scheme since it requires at most three cross-products in its correlation. It can also facilitate a reduced DSP complexity for CD compensation since it is able to handle some of the CD. This makes the CA-CMA a potential candidate for robust and efficient adaptive equalization in harsh environments for the future OAN.

Perspectives

The results presented in this thesis indicate that the CA-CMA equalizer has a good potential for robust and efficient adaptive equalization in the OAN. However, we believe that there are still some research directions to work on in order to fully exploit its potential capabilities. Some of these directions are as follows:

Fine-granularity CA-CMA : The CA-CMA equalizer we have proposed works on a symbol period step granularity of the cross-correlations and cross-products to mitigate the PMD-induced correlations. Hence it is not able to finely track differential group delays that are a fraction of a symbol period. One way to handle this would be to implement a fractionally spaced cross-correlation to improve the singularity performance of the CA-CMA equalizer. This would however increase the complexity of the equalizer in terms of number of operations but it may also potentially reduce the tracking time for convergence as the impairment-induced cross-correlations could be found in a faster way since more information will be available to the equalizer with a finer granularity implementation.

Variable step-size : The step-size parameter μ in gradient descent-based optimization algorithms greatly impacts the convergence speed. A smaller step-size enables fine tracking leading to a slower convergence while a larger step-size enables a coarse tracking leading to a faster convergence but with possibility to miss the global minimum (if it exists). In our CA-CMA equalizer, we used a fixed step-size of value 10^{-3} which was adequate for our CA-CMA. However a variable step-size tuning where the step size is large in the first few iterations and then gradually decreased as the error function decreases could offer a faster convergence of the CA-CMA.

Higer order modulation formats : We have proposed the CA-CMA equalizer for 100 Gbps obtained by a 32 Gbaud DP-QPSK system. This was reasonable to do because the baud rate is readily feasible and the QPSK modulation format satisfies the requirement of constant modulus for which CMA-like algorithms are well-suited. However, CMA-like algorithms have also been shown to work quite well with higher order modulation formats. In the interest of further capacity increase, scaling up to 200- and 400 Gbps/λ as envisioned in the future OAN, it would be a good direction to investigate the performance of the CA-CMA in higher order modulation formats such as 16-QAM.

Space division multiplexing (SDM) : SDM utilizes space as yet another degree of freedom for capacity increase. Having exploited the four degrees of freedom of a light wave (i.e. amplitude and phase along two polarization tributaries), the only other option currently available is space. If further capacity increase is required in the future OAN, after all other degrees of freedom have been maxed out, the SDM could be considered for the future OAN. In this scenario, our proposed CA-CMA has the potential for application in SDM transmission. In SDM systems where the spatial dimension utilized is the fiber modes, singularities can also occur during transmission due to modal dispersion. The CA-CMA has been experimentally demonstrated to achieve zero singularities in an SDM transmission involving three modes [107]. Further study would be needed on exploring the performance of the CA-CMA for more than three modes.

APPENDIX A

PMD-impaired signal derivation

If it is possible, as far as it depends on you, live at peace with everyone.
— Romans 12:18

Contents

PMD-impaired signal derivation

We derive the proof of Eq. (2.3) for the PMD frequency domain channel model, and Eq. (2.5) - (2.6) for the time-domain received PMD impaired signals, which we stated in section 2.1 of chapter 2.

A.1 Frequency domain PMD channel model

We considered the PMD impairment acting alone and modelled it by a single birefringence element, in the frequency domain, as a product of a rotation matrix $\mathbf{R}(\theta)$, a differential group delay (DGD) matrix $\mathbf{DGD}(\tau,\omega)$, a birefringent phase shift matrix $\mathbf{B}(\phi)$, and an inverse rotation matrix $\mathbf{R}(-\theta)$:

$$\mathbf{R}(\theta)=\begin{bmatrix}\cos(\theta) & -\sin(\theta)\\ \sin(\theta) & \cos(\theta)\end{bmatrix},\mathbf{B}(\phi)=\begin{bmatrix}e^{j\phi/2} & 0\\ 0 & e^{-j\phi/2}\end{bmatrix},\mathbf{DGD}(\tau,\omega)=\begin{bmatrix}e^{j\omega\tau/2} & 0\\ 0 & e^{-j\omega\tau/2}\end{bmatrix} \tag{A.1}$$

with $j=\sqrt{-1}$. The combined channel effect, $\mathbf{H_{PMD}}(\omega)$ can be written as

$$\mathbf{H_{PMD}}(\omega)=\mathbf{R}(\theta)\mathbf{B}(\phi)\mathbf{DGD}(\tau,\omega)\mathbf{R}(-\theta) \tag{A.2}$$

The matrix multiplication in Eq. (A.2) gives:

$$\mathbf{H_{PMD}}(\omega)=\begin{bmatrix}e^{j\chi}\cos^2(\theta)+e^{-j\chi}\sin^2(\theta) & e^{j\chi}\cos(\theta)\sin(\theta)-e^{-j\chi}\cos(\theta)\sin(\theta)\\ e^{j\chi}\cos(\theta)\sin(\theta)-e^{-j\chi}\cos(\theta)\sin(\theta) & e^{j\chi}\sin^2(\theta)+e^{-j\chi}\cos^2(\theta)\end{bmatrix} \tag{A.3}$$

with $\chi=(\omega\tau+\phi)/2$.

To simplify each element in Eq. (A.3), we can represent Eq. (A.3) as:

$$\mathbf{H_{PMD}}(\omega)=\begin{bmatrix}a & b\\ c & d\end{bmatrix} \tag{A.4}$$

where

$$a=e^{j\chi}\cos^2(\theta)+e^{-j\chi}\sin^2(\theta) \tag{A.5}$$

$$b=c=e^{j\chi}\cos(\theta)\sin(\theta)-e^{-j\chi}\cos(\theta)\sin(\theta) \tag{A.6}$$

$$d=e^{j\chi}\sin^2(\theta)+e^{-j\chi}\cos^2(\theta) \tag{A.7}$$

From trigonometric identities,

$$\cos^2(\theta)=\left(\frac{e^{j\theta}+e^{-j\theta}}{2}\right)^2=\frac{e^{j2\theta}+e^{-j2\theta}+2}{4} \tag{A.8}$$

$$\sin^2(\theta)=\left(\frac{e^{j\theta}-e^{-j\theta}}{2j}\right)^2=\frac{e^{j2\theta}+e^{-j2\theta}-2}{-4} \tag{A.9}$$

$$\cos(\theta)\sin(\theta)=\frac{\sin(2\theta)}{2} \tag{A.10}$$

Substituting Eq. (A.8) - (A.10) into Eq. (A.5) - (A.7), and noting from Eq. (A.6) that

$e^{j\chi} - e^{-j\chi} = 2j\sin\chi$, after expansion and regrouping by similar angles, we obtain

$$a = \frac{e^{j(\chi+2\theta)} - e^{-j(\chi+2\theta)} + e^{j(\chi-2\theta)} - e^{-j(\chi-2\theta)} + 2e^{j\chi} + 2e^{-j\chi}}{4} \tag{A.11}$$

$$b = c = \frac{\sin(2\theta)}{2}(2j\sin\chi) \tag{A.12}$$

$$d = \frac{-e^{j(\chi+2\theta)} + e^{-j(\chi+2\theta)} - e^{j(\chi-2\theta)} + e^{-j(\chi-2\theta)} + 2e^{j\chi} + 2e^{-j\chi}}{4} \tag{A.13}$$

Upon regrouping according to trigonometric identities, we obtain

$$a = j\frac{\sin(\chi+2\theta)}{2} + j\frac{\sin(\chi-2\theta)}{2} + \cos(\chi) \tag{A.14}$$

$$b = c = \frac{\sin(2\theta)}{2}(2j\sin\chi) \tag{A.15}$$

$$d = -j\frac{\sin(\chi+2\theta)}{2} - j\frac{\sin(\chi-2\theta)}{2} + \cos(\chi) \tag{A.16}$$

Noting also from trigonometric identities that $\frac{\sin(\chi+2\theta)+\sin(\chi-2\theta)}{2} = \sin(\chi)\cos(2\theta)$ and that $\frac{\cos(\chi-2\theta)-\cos(\chi+2\theta)}{2} = \sin(\chi)\sin(2\theta)$, we substitute into Eq. (A.4) to finally obtain the simplified expression:

$$\mathbf{H_{PMD}}(\omega) = \begin{bmatrix} \cos(\chi) + j\sin(\chi)\cos(2\theta) & j\sin(\chi)\sin(2\theta) \\ j\sin(\chi)\sin(2\theta) & \cos(\chi) - j\sin(\chi)\cos(2\theta) \end{bmatrix} \tag{A.17}$$

which is the expression stated in Eq. (2.3).

A.2 Time domain PMD-impaired signal

The signal received into the equalizer is impaired by $\mathbf{H_{PMD}}(\omega)$ and noise $\mathbf{N}(\omega)$ and given, in frequency domain, as

$$\mathbf{Y}(\omega) = \mathbf{H_{PMD}}(\omega)\mathbf{X}(\omega) + \mathbf{N}(\omega) \tag{A.18}$$

with $\mathbf{Y}(\omega) = [\mathbf{Y_1}(\omega), \mathbf{Y_2}(\omega)]^{\mathrm{T}}$, $\mathbf{X}(\omega) = [\mathbf{X_1}(\omega), \mathbf{X_2}(\omega)]^{\mathrm{T}}$ and $\mathbf{N}(\omega) = [\mathbf{N_1}(\omega), \mathbf{N_2}(\omega)]^{\mathrm{T}}$.

Using the $\mathbf{H_{PMD}}(\omega)$ of Eq. (A.17), Eq. (A.18) becomes

$$\mathbf{Y_1}(\omega) = \mathbf{X_1}(\omega)\cos(\chi) + j\mathbf{X_1}\sin(\chi)\cos(2\theta) + j\mathbf{X_2}(\omega)\sin(\chi)\sin(2\theta) + \mathbf{N_1}(\omega) \tag{A.19}$$

$$\mathbf{Y_2}(\omega) = j\mathbf{X_1}(\omega)\sin(\chi)\sin(2\theta) + \mathbf{X_2}(\omega)\cos(\chi) - j\mathbf{X_2}(\omega)\sin(\chi)\cos(2\theta) + \mathbf{N_2}(\omega) \tag{A.20}$$

The time-domain expression can be obtained by taking the inverse Fourier transform $\mathcal{F}^{-1}[.]$ of Eq. (A.19) and Eq. (A.20), noting that $\mathcal{F}^{-1}[\mathbf{Y}(\omega)] = \mathbf{y}(t)$, $\mathcal{F}^{-1}[\mathbf{X}(\omega)] = \mathbf{x}(t)$, and

$$\mathcal{F}^{-1}[\cos(\chi)] = \mathcal{F}^{-1}\left[\frac{e^{j\frac{\phi}{2}}e^{j\frac{\omega\tau}{2}} + e^{-j\frac{\phi}{2}}e^{-j\frac{\omega\tau}{2}}}{2}\right] = \frac{e^{j\frac{\phi}{2}}\delta(t+\frac{\tau}{2}) + e^{-j\frac{\phi}{2}}\delta(t-\frac{\tau}{2})}{2} \tag{A.21}$$

$$\mathcal{F}^{-1}[j\sin(\chi)] = \mathcal{F}^{-1}\left[j\left(\frac{e^{j\frac{\phi}{2}}e^{j\frac{\omega\tau}{2}} - e^{-j\frac{\phi}{2}}e^{-j\frac{\omega\tau}{2}}}{2j}\right)\right] = \frac{e^{j\frac{\phi}{2}}\delta(t+\frac{\tau}{2}) - e^{-j\frac{\phi}{2}}\delta(t-\frac{\tau}{2})}{2} \tag{A.22}$$

where $\delta(.)$ is the Dirac delta function.

Multiplication in frequency domain corresponds to a convolution in time domain and the convolution of a function with a Dirac delta function results in the the original function at the time index of the Dirac delta function. With this information and noting from trigonometric identities that $\cos^2(\theta) = \frac{1+\cos(2\theta)}{2}$, the resulting time domain expression of the PMD-impaired signal is given below as:

$$\mathbf{y_1}(t) = \mathbf{x_1}\left(t+\frac{\tau}{2}\right)e^{j\frac{\phi}{2}}\cos^2(\theta) + \mathbf{x_1}\left(t-\frac{\tau}{2}\right)e^{-j\frac{\phi}{2}}\sin^2(\theta) + \left(\frac{\mathbf{x_2}\left(t+\frac{\tau}{2}\right)e^{j\frac{\phi}{2}} - \mathbf{x_2}\left(t-\frac{\tau}{2}\right)e^{-j\frac{\phi}{2}}}{2}\right)\sin(2\theta) + \mathbf{n_1}(t) \quad \text{(A.23)}$$

$$\mathbf{y_2}(t) = \mathbf{x_2}\left(t+\frac{\tau}{2}\right)e^{j\frac{\phi}{2}}\sin^2(\theta) + \mathbf{x_2}\left(t-\frac{\tau}{2}\right)e^{-j\frac{\phi}{2}}\cos^2(\theta) + \left(\frac{\mathbf{x_1}\left(t+\frac{\tau}{2}\right)e^{j\frac{\phi}{2}} - \mathbf{x_1}\left(t-\frac{\tau}{2}\right)e^{-j\frac{\phi}{2}}}{2}\right)\sin(2\theta) + \mathbf{n_2}(t) \quad \text{(A.24)}$$

APPENDIX B

Carrier phase estimation (CPE)

The past exists only in our memories, the future only in our plans. The present is our only reality.
— Robert M. Pirsig

The past exists only in our memories, the present is our conscious reality, and the future is our unconscious reality.
— P.A.N.

Contents

B.1 Introduction

In amplitude and phase diversity transmission schemes information is encoded on both the amplitude and phase of the transmitted signal. It is therefore necessary to properly retrieve the amplitude and phase information at the receiver. This will require the use of phase diversity receivers for example the phase diverse coherent receiver and phase retrieval receivers. Some impairments e.g. phase noise from the laser, additive white Gaussian noise (AWGN), laser frequency offset, chromatic dispersion, etc. affect the phase of the transmitted signal and make it impossible to correctly retrieve the phase information without further processing.

Laser phase noise in particular is caused by the spontaneous emission process of the laser. When the transmitter and local oscillator lasers in a coherent transmission system both have Lorentzian line shape, the phase noise is modelled as a Wiener process $\phi(n)$ which is a Gaussian random walk function [108, 80]:

$$\phi(n) = \phi(n-1) + w(n) \tag{B.1}$$

where $w(n)$ is a Gaussian noise sequence of variance σ_w^2 given by Eq. (B.2)

$$\sigma_w^2 = 2\pi\Delta\nu\tau_s \tag{B.2}$$

with $\Delta\nu$ the sum of the 3-dB linewidths of the transmitter and local oscillator lasers, and τ_s the sample duration. The laser linewidth has been shown to be inversely proportional to the output power, and it is therefore desirable to operate lasers at maximum power while attenuating their output as required [108].

Thanks to digital signal processing (DSP) it is possible to efficiently mitigate the effects of laser phase noise and other phase noise impairments in digital domain. Dedicated DSP blocks designed to mitigate the effects of a number of these impairments make use of some a priori knowledge of the impairment characteristics and dependencies. Hence, there are dedicated DSP blocks, for example, to mitigate chromatic dispersion, carrier frequency offset, and laser phase noise.

The DSP block for mitigating laser phase noise is the carrier phase estimation (CPE) block, and there are various carrier phase estimation algorithms [109, 39, 110, 111, 80, 82, 112, 78]. They could either be data-aided (DA), decision-directed (DD) or non-data-aided (NDA).

A well-known blind NDA CPE algorithm is the M^{th} power Viterbi-Viterbi (V-V) algorithm [78] which is suitable only for phase-shift-keying (PSK) modulation formats (e.g. QPSK) since it exploits the M-fold rotational symmetry of an M-PSK constellation [113, 82] with M being the number of all possible symbols in the constellation. A constellation is the complex plane representation of digital information signals mapped to complex symbols. The M^{th} power algorithm is however, known to have a phase ambiguity issue and cycle slips which result in a symbol error ratio (SER) of up to 0.5 even for low phase noise [113, 114]. It performs correct CPE only when the cycle slip (CS) is mitigated by some dedicated CS mitigation DSP block, and avoided by either a data-aided scheme or by the use of differential decoding. However, the use of differential coding results in a 3-dB penalty for the bit errors [78, 114, 39].

Moreover, depending on the representation of the constellation as we shall soon see, with a dedicated CS mitigation DSP block, the CS induced by the power-M operation can be mitigated but does not lead to a BER value of zero, in high SNR situation, if the phase estimate result from the M^{th} power Viterbi-Viterbi algorithm is used without consideration to the representation of the constellation. This point is not clearly addressed

in the literature considering that QPSK and 4-ary quadrature amplitude modulation (4-QAM) are similar. Hence, there are subtle implications of utilizing the M^{th} power Viterbi-Viterbi algorithm on each. We therefore investigate this point in detail highlighting the reason why the CS mitigation DSP block does not lead to zero BER, in high SNR, when used on 4-QAM. Then we propose a simple modification to the CPE process of the M^{th} power Viterbi algorithm which works well with 4-QAM after CS mitigation.

B.2 M^{th} Power Viterbi-Viterbi CPE algorithm

Assuming that all other channel impairments have been compensated by a digital coherent receiver, the received signal $\mathbf{z}(n)$ consists of the transmitted signal $\mathbf{x}(n)$ impaired by only phase noise $\phi(n)$ and additive white Gaussian noise (AWGN) $\mathbf{w}(n)$ and can be represented by Eq. (B.3) [80, 115]:

$$\mathbf{z}(n) = \mathbf{x}(n)e^{-j\phi(\mathbf{n})} + \mathbf{w}(n) \tag{B.3}$$

The transmitted signal $\mathbf{x}(n)$ can either be represented as Eq.(B.4) or Eq.(B.5):

$$\mathbf{x}(n) = \sqrt{P_t}e^{j2m\frac{\pi}{M}} \tag{B.4}$$

$$\mathbf{x}(n) = \sqrt{P_t}e^{j(2m+1)\frac{\pi}{M}} \tag{B.5}$$

with $m = 0, 1, \ldots, M-1$, and P_t is the power of the signal.

The most common representation of the QPSK and 4-QAM constellations is that of Eq.(B.5) which has a rotational angular difference of π/M from Eq.(B.4). The M^{th} power algorithm was originally designed to be applied on constellations represented by Eq.(B.4) and so leads to additional phase ambiguity of π/M when used directly for constellations represented by Eq.(B.5).

The M^{th} power Viterbi-Viterbi carrier phase estimation algorithm [78, 39, 109] raises the impaired input signal to the power M, where M is the number of constellation states (i.e. the cardinality of the constellation). This operation removes the impact of the modulation. The phase of this power M signal is then divided by M to give an estimate of the instantaneous value $\theta(n)$ of the phase offset induced by phase noise in the impaired signal. A reasonable estimate of $\hat{\theta}(n)$ for a particular symbol can be obtained by averaging over a window encompassing the symbols surrounding the particular symbol for which we want to estimate the phase. The length of the window is $2N+1$ where N is the number of symbols before and after the particular symbol whose phase is to be estimated. The larger the window, the larger is the SNR for phase estimation. However, the size of the window should not be too large since the contribution of the phase noise could be significant. The phase estimate is given by Eq. (B.6) below as [78, 115, 113]:

$$\hat{\theta}(n) = \frac{1}{M}\arg\left\{\frac{1}{2N+1}\sum_{l=-N}^{N}\mathbf{z}^M(l+n)\right\} \tag{B.6}$$

For QPSK signals, $M = 4$. If $\hat{\theta}(n) = \phi(n)$, then we can recover an estimate of the transmitted signal as Eq. (B.7)

$$\hat{\mathbf{z}}(n) = \mathbf{z}(n)e^{-j\hat{\theta}(n)} \tag{B.7}$$

However, this only applies to the case when the constellation is represented by Eq.(B.4) and will lead to a phase ambiguity issue for the constellation of Eq.(B.5) which is the most common representation.

B.2.1 Phase ambiguity issue

The method of Eq. (B.6) above does not yield the correct phase offset angle for constellations defined by Eq.(B.5). We can show this by taking for example, complex-valued symbols from an ideal (i.e. impairment-free) QPSK constellation ($M = 4$), as shown in Fig. B.1a. When these complex-valued QPSK symbols are raised to power M, the modulation is removed and all the complex-valued symbols become real-valued with an offset angle of π radians. Dividing this angle of π radians by 4, we obtain an instantaneous phase estimate $\theta(n) = \pi/4$ radians (i.e. 45°), as seen in Fig. B.1b.

Therefore, $\pi/4$ becomes the reference for an ideal QPSK constellation after power M operation. For received symbols that are corrupted by noise in the form of AWGN and laser phase noise e.g. as shown in Fig. B.1c and Fig. B.1e respectively, after the M^{th} power operation (i.e. full V-V operation), we obtain instantaneous phase estimate angles, $\theta(n)$, that span $[-\pi/4, \pi/4]$ radians as shown in Fig. B.1d.

We can clearly see in Fig. B.1c and Fig. B.1e the impact of the phase noise as distinguished from AWGN noise before and after the power M operation, respectively. The phase noise spreads the symbols circularly around the constellation plane, and spreads $\theta(n)$ in the power M space, but always within $[-\pi/4, \pi/4]$ radians as seen in Fig. B.1f.

These end points i.e. $-\pi/4$ and $\pi/4$, become the references for the received symbols. Any symbols that lead to $\theta(n)$ which is different from $\pi/4$ or $-\pi/4$ would have to be evaluated according to either reference to obtain a correct phase estimate, $\hat{\phi}(n)$. It is this evaluation according to the reference that that determines the correct phase estimate $\hat{\phi}(n)$ to be applied to the received (impaired) symbols. However, this evaluation is not done in the implementations of the Viterbi-Viterbi power M algorithms in literature clearly because the algorithm was designed for a particular constellation representation.

The resulting issue is that using the instantaneous phase estimate, $\theta(n)$, as the corrective phase estimate, without reference to the constellation representation, results in a phase shift of the estimated received symbols by an amount that would lead to phase ambiguity issues.

We therefore propose to modify the Viterbi-Viterbi power M algorithm, by computing the correct phase estimate $\hat{\phi}(n)$ taking into consideration the phase references ($-\pi/4$ and $\pi/4$) for the constellation representation of Eq.(B.5).

B.2.2 Proposal for correct phase determination

We proceed following the conventional steps of the power M operation as given by Eq. (B.6). Then for the correct phase estimate calculation, we compute the distance between the absolute value of the received symbol's instantaneous phase estimate, $\theta(n)$, and $\pi/4$ (a simple difference operation). This difference is the instantaneous phase correction offset that, after careful consideration which we soon describe, will be applied to the received symbols.

Given the received (impaired) symbols $\mathbf{z}(n)$, $\theta(n)$, and $\hat{\phi}(n)$, the phase corrected symbols estimate $\hat{\mathbf{z}}(n)$, are given by Eq. (B.8).

$$\hat{\mathbf{z}}(n) = \mathbf{z}(n)e^{-j\hat{\phi}(n)} \tag{B.8}$$

Note that we use a negative phase shift (clockwise rotation) in the exponential of Eq. (B.8). Hence, when $\hat{\phi}(n)$ is negative, the received symbols will be shifted by an overall positive phase offset (anti-clockwise rotation), and when $\hat{\phi}(n)$ is positive, the received symbols will be shifted by an overall negative phase offset (clockwise rotation).

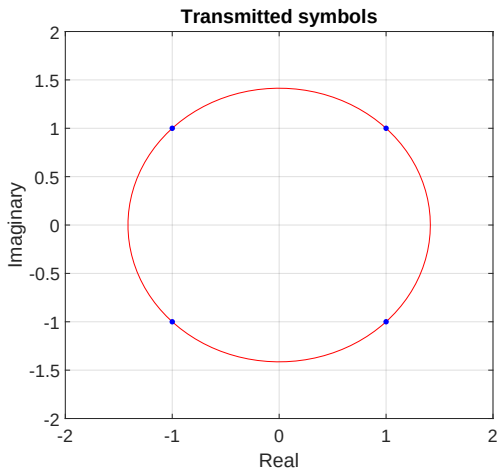

(a)

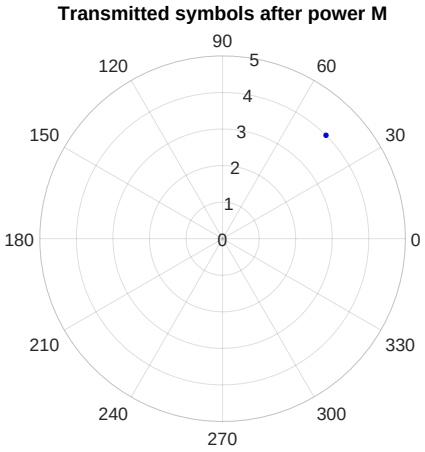

(b)

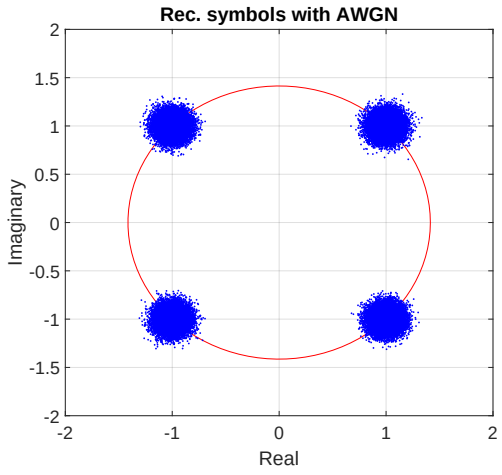

(c)

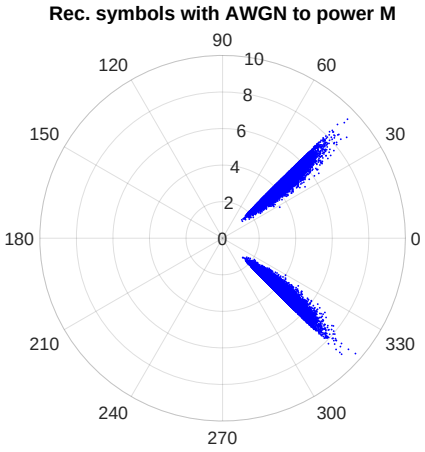

(d)

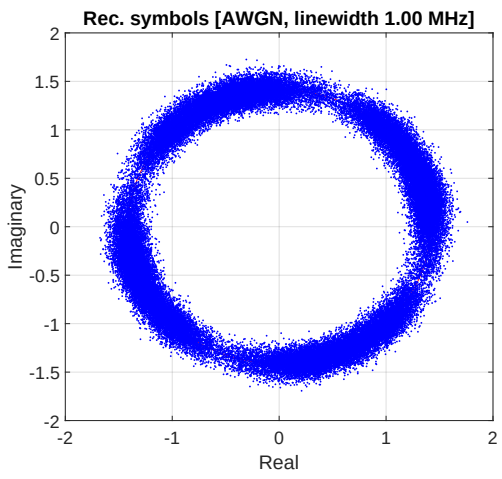

(e)

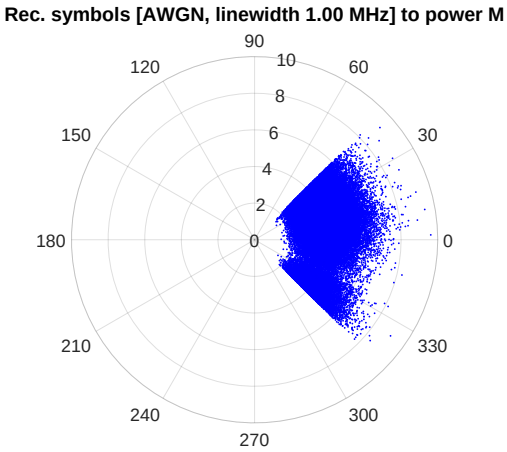

(f)

Figure B.1: Effect of Power M operation (full V-V operation) on QPSK constellation

The correct phase estimate $\hat{\phi}(n)$ is calculated by carefully considering the direction of phase shifts to be applied, and it depends on the sign (either positive or negative) of the instantaneous phase estimate, $\theta(n)$, after the conventional power M operation.

If $\theta(n)$ is negative, we would need a negative (clockwise) overall phase offset applied to the received symbols for the phase correction. This means that the actual phase estimate value, $\hat{\phi}(n)$ which is a phase difference between the absolute value of $\theta(n)$ and $\pi/4$, must be positive. The correct phase estimate to be applied is therefore: $\hat{\phi}(n) = \theta(n) + \pi/4$ radians (proof of this will be shown with a scheme in Fig. B.2)

If $\theta(n)$ is positive, we would need a positive (anti-clockwise) overall phase offset applied to the received symbols for the phase correction. This means that the actual phase estimate value, $\hat{\phi}(n)$ which is a phase difference between the absolute value of $\theta(n)$ and $\pi/4$, must be negative. The correct phase estimate to be applied is therefore: $\hat{\phi}(n) = \theta(n) - \pi/4$ as shown with the scheme in Fig. B.2.

We will use Fig. B.2 to prove the correct phase estimation process. Fig. B.2 presents a QPSK constellation. For the purpose of clarity, we will focus only on the first quadrant corresponding to the alphabet $1 + \mathrm{j}1$. We represent three points, which would correspond to symbols, in this first quadrant as $a(x, y)$, $b(x, y)$ and $c(x, y)$ where x and y are the coordinates of the real and imaginary components for the points. Points a and c are assumed to be noisy, hence displaced from their ideal (i.e. noiseless) location which should be at point b. The coordinates of the points are $a(0.98, 1.1)$, $b(1, 1)$, and $c(1.1, 0.98)$, and their corresponding phase angles, $\angle a$, $\angle b$, and $\angle c$, in degrees, are 48.3019°, 45°, and 41.698° respectively. After conventional power M operation, the instantaneous phase estimates, θ_a, θ_b, and θ_c, in degrees, are -41.6981°, 45°, and 41.6981° respectively. We note that the estimate, θ_b, for the ideal (noiseless) constellation point is 45°. We also recall, as shown in Fig.B.1, that for all points, after power M operation, the phase estimate θ spans $[-\pi/4, \pi/4]$ or [-45°, 45°].

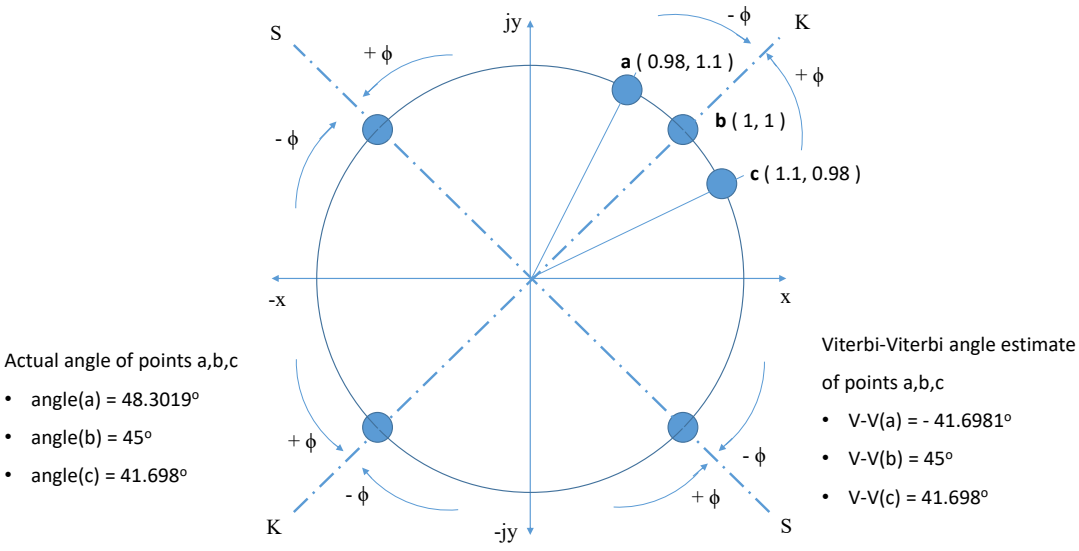

Figure B.2: Analysis of Power M operation

The conventional Viterbi-Viterbi uses the values of θ_a, θ_b, and θ_c as the final phase offsets by which to shift the received symbols. If we use these values directly without considering the constellation representation, it means that even the ideal (noiseless) point

$b(1,1)$ will be shifted by $\hat{\phi}_b = 45°$ when we would rather expect it to remain as is i.e. shifted by a value $\hat{\phi}_b = 0°$. This means that directly using the phase estimates results in an erroneous phase offset correction and introduces a phase ambiguity issue. The correct phase offset to be applied to the received symbols should be proportional to the difference between the phase estimates of the noisy symbols and the ideal symbol after power M operation.

It is also necessary at this point to state that the sign of $\theta(n)$, depends on the spatial distribution of the symbols in each quadrant of the constellation. The position of the ideal (noiseless) symbols determines the boundary for the change of the sign of $\theta(n)$. If two straight lines K-K and S-S are drawn from the origin to the ideal symbols e.g. to $b(1,1)$, then for $M = 4$ as in a QPSK or 4-QAM constellation we would have four dashed lines, one in each quadrant of the complex plane, and each of them will be at an angle of 45°to the real x-axis.

In each quadrant we can distinguish regions of the constellation where the received symbols will have either a positive or negative value of $\theta(n)$ after the power M operation. The sign of $\theta(n)$ determines the overall direction of phase shift to be applied to the received symbols as stated earlier. The curved arrows in Fig. B.2 indicate these directions and show that they are towards the reference boundary line connecting the ideal (noiseless) symbols to the origin. The magnitude of the phase shift to be applied is determined by the calculated phase estimate, $\hat{\phi}(n)$ which is a simple difference operation between the reference value of $\pi/4$ and the absolute value of $\theta(n)$. For negative $\theta(n)$, $\hat{\phi}(n) = \theta(n) + \pi/4$ is positive, and the overall phase offset applied to the received symbol is negative. For positive $\theta(n)$, $\hat{\phi}(n) = \theta(n) - \pi/4$ is negative, and the overall phase offset applied to the received symbol is positive.

Following this rule, the correct phase estimate, $\hat{\phi}_a$, for point $a(0.98, 1.1)$ with $\theta_a = -41.6981°$ should be $\hat{\phi}_a = \theta_a + 45° = 3.3019°$. This means that an overall negative phase shift of $\hat{\phi}_a$ should be applied to point $a(0.98, 1.1)$ for correction.

For point $b(1,1)$ with $\theta_b = 45°$, $\hat{\phi}_b = \theta_b - 45° = 0°$. This means that no phase shift should be applied to point $b(1,1)$ as expected.

For point $c(1.1, 0.98)$ with $\theta_c = 41.6981°$ $\hat{\phi}_c = \theta_c - 45° = -3.3019°$. This means that an overall positive phase shift of $\hat{\phi}_c$ should be applied to point $c(1.1, 0.98)$ for correction.

A general rule, the correct phase estimate to be applied to the received signal that originated from a constellation representation of Eq.(B.5) is therefore,

$$\hat{\phi}(n) = \text{sgn}(\theta(n)) \times [|\theta(n)| - \pi/4] \tag{B.9}$$

where $\text{sgn}(\theta(n))$ is the signum function of the phase estimate $\theta(n)$.

B.2.3 Cycle slips

Cycle slips (CS) are random phase rotations that are inherent as a result of the carrier phase estimation process of the M^{th} power non-linearity of the Viterbi algorithm. For QPSK signals, it results in phase ambiguity (or phase jumps) of integer multiples of $\pi/2$ for the instantaneous phase estimate $\theta(n)$. The onset of a CS begins when the maximum of the absolute value of the phase noise exceeds $\pi/4$. This occurs, in a QPSK constellation, when the phase noise is such that it spreads the symbols into another quadrant. As pointed out in subsection B.2.2, the sign of $\theta(n)$ depends on the spatial distribution of the noisy symbols in each quadrant of the constellation. We also see in Fig. B.2 that the sign of $\theta(n)$ alternates at every half-quadrant. Therefore a phase noise value greater than $\pi/4$ will spread the symbols across another quadrant.

Fig. B.3 is a plot of the evolution of the actual value of phase noise over the total signal samples, in blue, and generated with variance according to Eq. (B.2). The red curve is the evolution of the $\theta(n)$ value of the same phase noise after a 4th order non-linearity (i.e. power-4 operation). We can see that as the phase noise exceeds $\pi/4$, $\theta(n)$ exhibits cycle slip with phase jumps that span a dynamic range of $\pi/2$. Without CS mitigation, the CS will result in bit errors for all the subsequent symbols after CS occurrence.

It is important to note that without CS mitigation the M^{th} power Viterbi algorithm applied directly to a QPSK modulated signal can result in cycle slips, hence a SER of up to 0.5 even for low values of the phase noise. With CS mitigation, the BER value can be decreased to zero in high SNR situation.

However, if the representation of the constellation is not taken into account, the estimate of the phase noise can lead to an SER of 0.5 (hence a BER of 0.25 for QPSK) for any value of phase noise and AWGN different from zero.

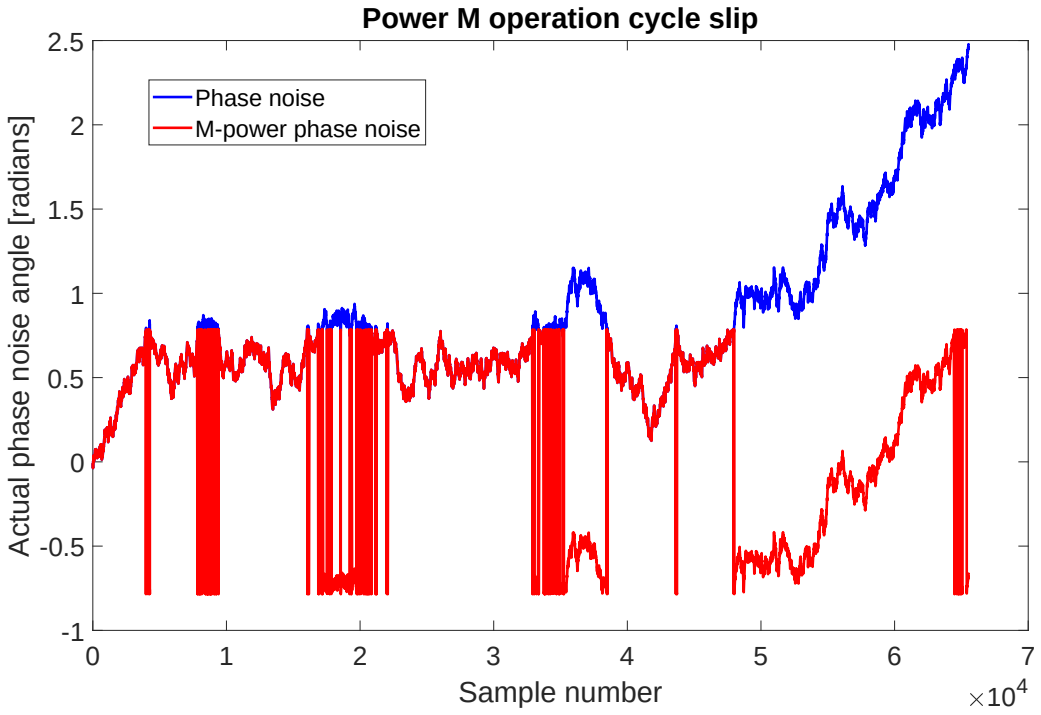

Figure B.3: Cycle slip effect of Power M operation

CS mitigation involves first of all, identification of the points where CS occurs by a difference operation on $\theta(n)$, to give $\theta_{diff}(n)$. The position of the CS will be the position where the absolute value of $\theta_{diff}(n)$ is greater than $\pi/4$. These points are then set to $\pm\pi/2$ depending on the sign of $\theta_{diff}(n)$, and represent a new variable $\theta_{[0,\pm\pi/2]}(n)$. The cumulative sum of $\theta_{[0,\pm\pi/2]}(n)$ is $\theta_{cumul}(n)$. The CS mitigated phase estimate is now $\hat{\phi}_{CS}(n) = \theta(n) - \theta_{cumul}(n)$. The final CS mitigated received signal is Eq.(B.10):

$$\hat{\mathbf{z}}(n) = \mathbf{z}(n)e^{-i\hat{\phi}_{CS}(n)} \tag{B.10}$$

B.3 Results and Discussion

To verify our proposed method with the transmitted constellation representation of Eq.(B.5), we present in Fig. B.4 the constellation of received symbols after carrier phase estimation

(CPE) and CS mitigation using the conventional Viterbi-Viterbi and in Fig. B.5 the constellation of the received symbols after CPE and CS mitigation using the modification we propose. We considered only the effect of phase noise and AWGN. The linewidth simulated is 1 MHz and the phase noise variance is in accordance with Eq. (B.2) for a 32 Gbaud dual polarization QPSK coherent transmission system. The AWGN variance was chosen such that we can start to obtain non-zero BER when the linewidth exceeds 5 MHz. After CPE and CS mitigation, we can see from Fig. B.4 that the phase noise of Fig. B.1e due to a linewidth of 1 MHz has been mitigated for both polarization tributaries, but the received symbols constellation has a phase ambiguity of $\pi/4$ when compared to the constellation of Fig. B.1c. However this is not the case with the proposed modification of the Viterbi algorithm after CPE and CS mitigation as seen in Fig. B.5 where the phase noise has been mitigated and the received constellation has no phase ambiguity. To further verify the phase ambiguity, it is important to see the number of bit errors that result from the use of both algorithms. Fig. B.6 is a plot of the positions of the bit errors of the phase

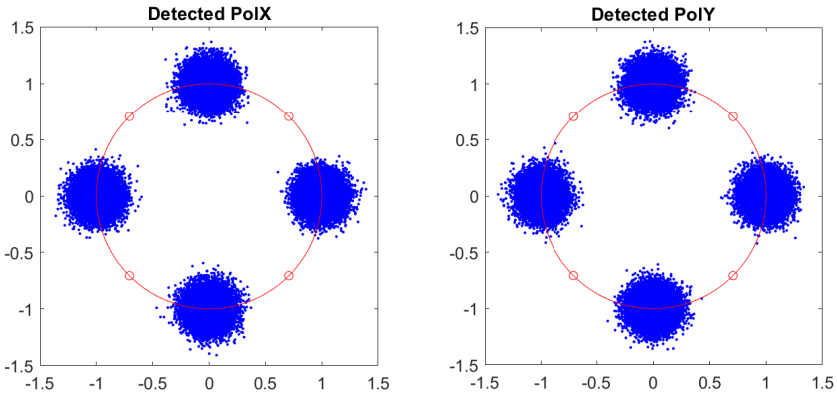

Figure B.4: Recovered constellation after Viterbi CPE with CS mitigation

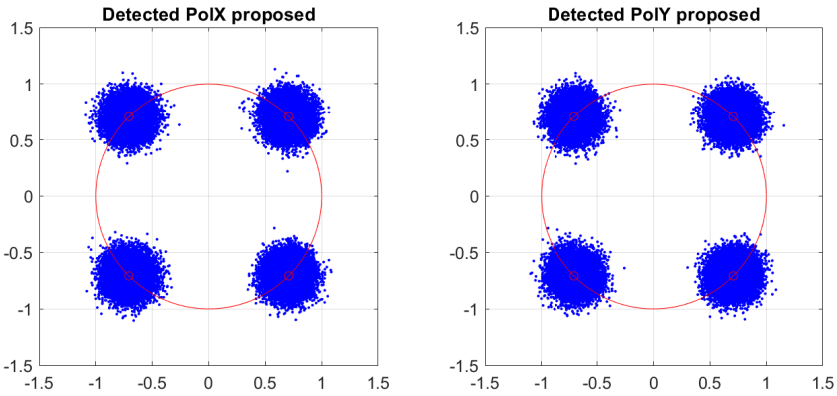

Figure B.5: Recovered constellation after proposed modification to Viterbi CPE with CS mitigation

estimation process after CS mitigation for the conventional Viterbi algorithm and the proposed modified Viterbi. We can see that the conventional Viterbi algorithm produces several bit errors. Although not shown here, the BER is 0.25. This is expected due to the phase ambiguity issue. However, the proposed algorithm has zero errors in high SNR and hence has no phase ambiguity issue. Next we present the phase evolution before CS miti-

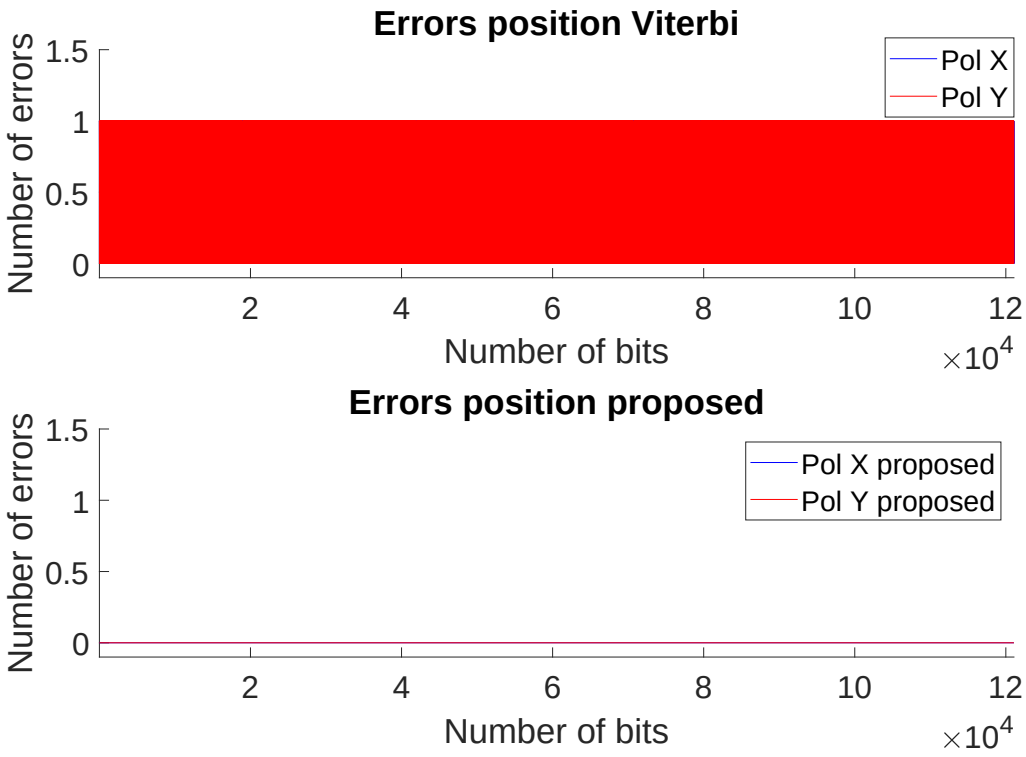

Figure B.6: Bit error comparison for both Viterbi CPE and the proposed Viterbi CPE

gation for both algorithms in Fig. B.7. We can see that both algorithms exhibit cycle slips before CS mitigation. However, the cycle slips do not occur at the same positions. We also present the phase evolution after CS mitigation for both algorithms in Fig. B.8. We can see that there are no cycle slips for both algorithms. However we notice that even though there are no cycle slips, the phase estimates for both algorithms differ by a general offset value. Here the offset value between our proposed algorithm and the conventional Viterbi is $\pi/4$ above and below the phase estimate of our proposed algorithm. This explains the phase ambiguity issue and why the BER value of the conventional Viterbi is 0.25. Here, it is clear that each of the polarization tributaries of the conventional Viterbi scheme has a different phase offset which cannot be detected by looking at only the constellation plot. Therefore is is necessary to compute the correct phase offset $\hat{\phi}(n)$ by carefully considering the representation of the constellation and modifying the instantaneous phase estimates $\theta(n)$ as necessary.

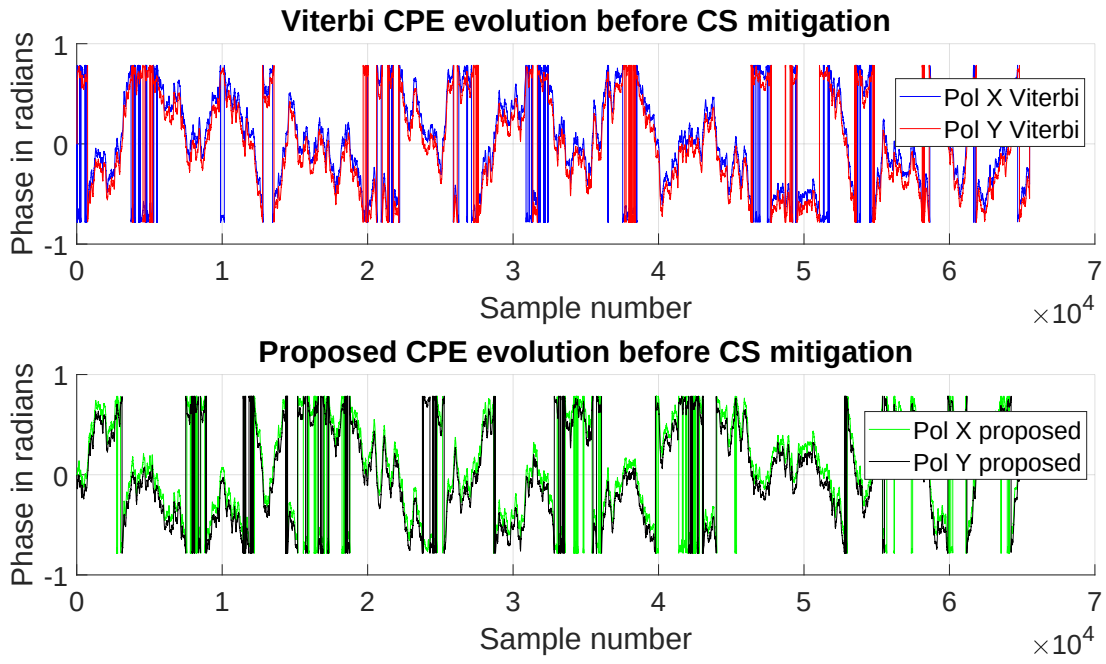

Figure B.7: CPE evolution before CS mitigation

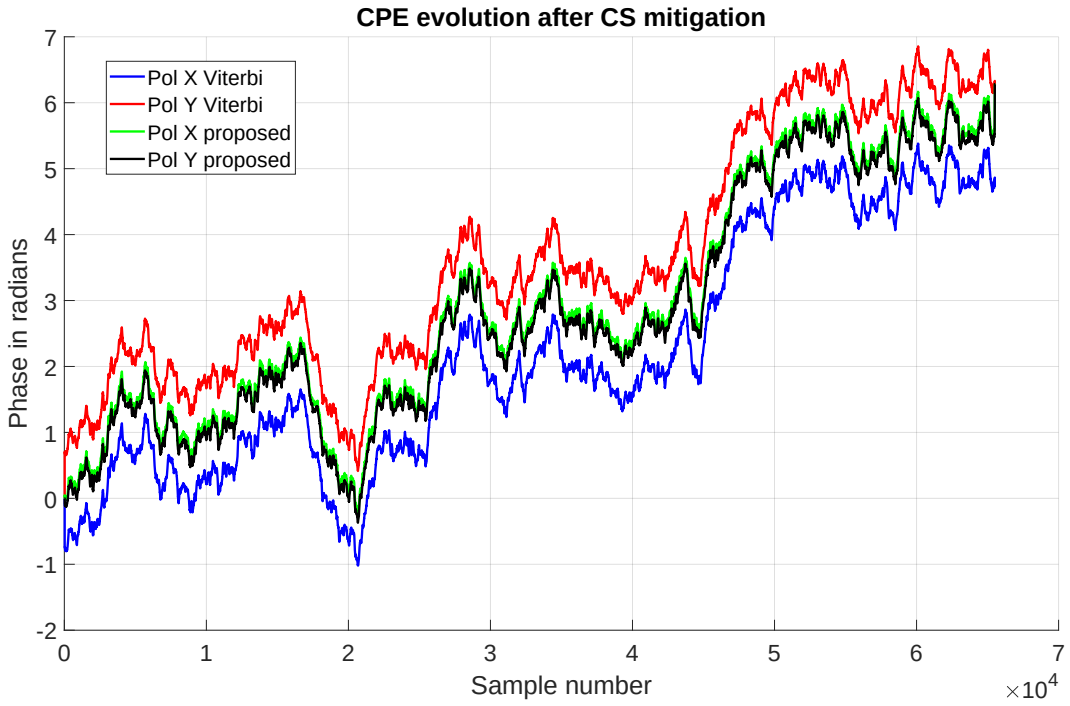

Figure B.8: CPE evolution after CS mitigation

Bibliography

[1] "Submarine Cables | National Oceanic and Atmospheric Administration," https://www.noaa.gov/submarine-cables, Mar. 2024.

[2] M. Hernández, "Fibre optics: The journey through undersea cables," https://www.telefonica.com/en/communication-room/blog/fibre-optics-the-journey-through-undersea-cables/, Apr. 2024.

[3] "Information Warfare in the Depths: An Analysis of Global Undersea Cable Networks," https://www.usni.org/magazines/proceedings/2023/may/information-warfare-depths-analysis-global-undersea-cable-networks, May 2023.

[4] N. Schadlow and B. Helwig, "Protecting undersea cables must be made a national security priority," https://www.defensenews.com/opinion/commentary/2020/07/01/protecting-undersea-cables-must-be-made-a-national-security-priority/, Jul. 2020.

[5] "Statistics," https://www.itu.int:443/en/ITU-D/Statistics/Pages/stat/default.aspx.

[6] "Cisco Annual Internet Report - Cisco Annual Internet Report (2018–2023) White Paper," https://www.cisco.com/c/en/us/solutions/collateral/executive-perspectives/annual-internet-report/white-paper-c11-741490.html.

[7] "The Fourth Industrial Revolution: What it means and how to respond," https://www.weforum.org/agenda/2016/01/the-fourth-industrial-revolution-what-it-means-and-how-to-respond/, Jan. 2016.

[8] Z. Wei, J. Zhang, W. Li, C. St-Arnault, S. Bernal, M. Khalil, R. Gutiérrez-Castrejon, L. R. Chen, and D. V. Plant, "The Role of Power-division Non-orthogonal Multiplexing Access (NOMA) for Enhancing Density and Fairness of Different Coherent Optical Metro-access Networks," in *50th European Conference on Optical Communications (ECOC 2024)*, vol. 2024, 2024, p. M2A.3.

[9] V. Houtsma, R. Borkowski, K. Vijayan, and D. van Veen, "Real-time 50G PON in service ODN monitoring based on receiver side DSP," in *50th European Conference on Optical Communications (ECOC 2024)*, vol. 2024, 2024, p. M2A.1.

[10] R. Matsumoto, T. Inoue, and S. Namiki, "Coexistence of OOK Transceivers in Point-to-Multipoint Access Systems Based on Coherent Subcarrier Multiplexing," in *50th European Conference on Optical Communications (ECOC 2024)*, vol. 2024, 2024, p. M1A.4.

[11] J. Segarra, V. Sales, and J. Prat, "Versatile Metro-Access Network Integrating FTTH, Enterprises, IoT and 5G Services," in *2019 21st International Conference*

on Transparent Optical Networks (ICTON). Angers, France: IEEE, Jul. 2019, pp. 1–6.

[12] ITU, "Recommendation ITU-T G.9804.1 Amd.2: Higher speed passive optical networks - Requirements," https://www.itu.int/rec/T-REC-G.9804.1-202401-I!Amd2/en, 2019.

[13] N. J. Gomes, "Towards mobile fronthaul for 6g networks," in *2023 Optical Fiber Communications Conference and Exhibition (OFC)*, 2023, pp. 1–18.

[14] T. Suzuki, Y. Koyasako, S.-Y. Kim, J.-I. Kani, and T. Yoshida, "Demonstration of industrial network applications by phy softwarization for fully virtualized access networks," in *2023 Optical Fiber Communications Conference and Exhibition (OFC)*, 2023, pp. 1–3.

[15] H. Zhang, Z. Jia, K. Choutagunta, L. A. Campos, and C. Knittle, "Adaptable modulation and baud rates in coherent tfdm pons: Towards versatile high-speed access networks," in *50th European Conference on Optical Communications (ECOC 2024)*, vol. 2024, 2024, p. Tu3D.2.

[16] D. Zhang, D. Liu, X. Wu, and D. Nesset, "Progress of ITU-T higher speed passive optical network (50G-PON) standardization," *Journal of Optical Communications and Networking*, vol. 12, no. 10, p. D99, Oct. 2020.

[17] F. Effenberger, "Q2 Optical Access Networks."

[18] M. Chagnon, "Optical Communications for Short Reach," *Journal of Lightwave Technology*, vol. 37, no. 8, pp. 1779–1797, Apr. 2019.

[19] D. V. Plant, M. Morsy-Osman, and M. Chagnon, "Optical Communication Systems for Datacenter Networks," in *Optical Fiber Communication Conference*. Los Angeles, California: OSA, 2017, p. W3B.1.

[20] J. K. Perin, A. Shastri, and J. M. Kahn, "Coherent Data Center Links," *Journal of Lightwave Technology*, vol. 39, no. 3, pp. 730–741, Feb. 2021.

[21] X. Chen, C. Antonelli, S. Chandrasekhar, G. Raybon, A. Mecozzi, M. Shtaif, and P. Winzer, "Kramers–Kronig Receivers for 100-km Datacenter Interconnects," *Journal of Lightwave Technology*, vol. 36, no. 1, pp. 79–89, Jan. 2018.

[22] M. S. Erkilinc, D. Lavery, K. Shi, B. C. Thomsen, P. Bayvel, R. I. Killey, and S. J. Savory, "Polarization-Insensitive Single-Balanced Photodiode Coherent Receiver for Long-Reach WDM-PONs," *Journal of Lightwave Technology*, vol. 34, no. 8, pp. 2034–2041, Apr. 2016.

[23] L. A. Neto, J. Maes, P. Larsson-Edefors, J. Nakagawa, K. Onohara, and S. J. Trowbridge, "Considerations on the Use of Digital Signal Processing in Future Optical Access Networks," *Journal of Lightwave Technology*, vol. 38, no. 3, pp. 598–607, Feb. 2020.

[24] K. Matsuda and N. Suzuki, "Hardware-Efficient Signal Processing Technologies for Coherent PON Systems," *Journal of Lightwave Technology*, vol. 37, no. 6, pp. 1614–1620, Mar. 2019.

[25] M. Morsy-Osman, M. Sowailem, E. El-Fiky, T. Goodwill, T. Hoang, S. Lessard, and D. V. Plant, "DSP-free 'coherent-lite' transceiver for next generation single wavelength optical intra-datacenter interconnects," *Optics Express*, vol. 26, no. 7, p. 8890, Apr. 2018.

[26] M. S. Faruk, X. Li, D. Nesset, I. N. Cano, A. Rafel, and S. J. Savory, "Coherent Passive Optical Networks: Why, When, and How," *IEEE Communications Magazine*, vol. 59, no. 12, pp. 112–117, Dec. 2021.

[27] S. Das, F. Slyne, A. Kaszubowska, and M. Ruffini, "Virtualized EAST–WEST PON architecture supporting low-latency communication for mobile functional split based on multiaccess edge computing," *Journal of Optical Communications and Networking*, vol. 12, no. 10, p. D109, Oct. 2020.

[28] "ITU - Infrastructure Connectivity Map," https://bbmaps.itu.int/bbmaps/.

[29] "My internet connection | Arcep," https://cartefibre.arcep.fr/index.html ?lng=2.9155336656537543&lat=46&zoom=6.5&mode=normal&legende=true&filter =true&trimestre=2024T2.

[30] "Broadband statistics," https://www.oecd.org/en/topics/sub-issues/broadband-statistics.html.

[31] I. P. Kaminow, T. Li, and A. E. Willner, Eds., *Optical Fiber Telecommunications VI*, 6th ed. Amsterdam ; Boston: Academic Press : Elsevier, 2013.

[32] "Understanding and measuring chromatic dispersion," https://www.fiberopticsonline.com/doc/understanding-and-measuring-chromatic-dispers-0002.

[33] FOWIKI.com, "Understand Fiber Attenuation," Jun. 2015.

[34] G. Keiser, *Fiber Optic Communications*. Springer Nature Singapore, 2021. [Online]. Available: https://books.google.fr/books?id=5_ggEAAAQBAJ

[35] P. Tandon, K. Bennett, M. Tuggle, D. Butler, H. de Pedro, P. Hebgen, C. Sutton, H. B. Matthews, M. Drake, S. Johnson, S. Makovejs, J. Downie, and L. Galdino, "Record Low Loss 0.144 dB/km 2-Core Optical Fiber for Submarine Transmission," *Journal of Lightwave Technology*, vol. 42, no. 12, pp. 4213–4221, Jun. 2024.

[36] "What Is The Diameter Of Fiber Optic Cable? |," Dec. 2022.

[37] "Micro-Coaxial/Twinax Connectors | I-PEX," https://www.i-pex.com/product/micro-coaxial_twinax.

[38] F. Derr, "Coherent optical QPSK intradyne system: Concept and digital receiver realization," *Journal of Lightwave Technology*, vol. 10, no. 9, pp. 1290–1296, Sep. 1992.

[39] S. J. Savory, "Digital Coherent Optical Receivers: Algorithms and Subsystems," *IEEE Journal of Selected Topics in Quantum Electronics*, vol. 16, no. 5, pp. 1164–1179, Sep. 2010.

[40] D. Hood and E. Trojer, *Gigabit-Capable Passive Optical Networks*, 1st ed. Wiley, Mar. 2012.

[41] G. P. Agrawal, *Fiber-optic communication systems.* John Wiley & Sons, 2012.

[42] D. Che, "Coherent optical short-reach communications."

[43] K. Rochford, "Polarization and Polarimetry," in *Encyclopedia of Physical Science and Technology.* Elsevier, 2002, pp. 521–538.

[44] J. Yu and N. Chi, *Digital Signal Processing In High-Speed Optical Fiber Communication Principle and Application.* Singapore: Springer Singapore, 2020.

[45] B. Mukherjee, I. Tomkos, M. Tornatore, P. Winzer, and Y. Zhao, Eds., *Springer Handbook of Optical Networks*, ser. Springer Handbooks. Cham: Springer International Publishing, 2020.

[46] G. P. Agrawal, *Fiber-Optic Communication Systems*, 3rd ed., ser. Wiley Series in Microwave and Optical Engineering. New York: Wiley-Interscience, 2002.

[47] F. Mitschke, *Fiber Optics.* Berlin, Heidelberg: Springer Berlin Heidelberg, 2016.

[48] X. Zhou, "Enabling Technologies for High Spectral-efficiency Coherent Optical Communication Networks."

[49] G. P. Agrawal, *Nonlinear Fiber Optics*, 4th ed., ser. Quantum Electronics–Principles and Applications. Amsterdam ; Boston: Elsevier / Academic Press, 2007.

[50] S. Ten, "An Introduction to the Fundamentals of PMD in Fibers," Jan. 2006.

[51] X. Zhou and C. Xie, *Enabling technologies for high spectral-efficiency coherent optical communication networks.* John Wiley & Sons, 2016.

[52] "G.987 : 10-Gigabit-capable passive optical network (XG-PON) systems: Definitions, abbreviations and acronyms," https://www.itu.int/rec/T-REC-G.987.

[53] P. Winzer and R.-J. Essiambre, "Advanced Optical Modulation Formats," *Proceedings of the IEEE*, vol. 94, no. 5, pp. 952–985, May 2006.

[54] "G.9804.3 : 50-Gigabit-capable passive optical networks (50G-PON): Physical media dependent (PMD) layer specification," https://www.itu.int/rec/T-REC-G.9804.3.

[55] P. Torres-Ferrera, F. Effenberger, M. S. Faruk, S. J. Savory, and R. Gaudino, "Overview of high-speed TDM-PON beyond 50 Gbps per wavelength using digital signal processing [Invited Tutorial]," *Journal of Optical Communications and Networking*, vol. 14, no. 12, pp. 982–996, Dec. 2022.

[56] E. Harstead, R. Bonk, S. Walklin, D. van Veen, V. Houtsma, N. Kaneda, A. Mahadevan, and R. Borkowski, "From 25 Gb/s to 50 Gb/s TDM PON: Transceiver architectures, their performance, standardization aspects, and cost modeling," *Journal of Optical Communications and Networking*, vol. 12, no. 9, p. D17, Sep. 2020.

[57] L. Yi, T. Liao, L. Huang, L. Xue, P. Li, and W. Hu, "Machine Learning for 100 Gb/s/λ Passive Optical Network," *Journal of Lightwave Technology*, vol. 37, no. 6, pp. 1621–1630, Mar. 2019.

[58] G. RizzelliMartella, A. Nespola, S. Straullu, F. Forghieri, and R. Gaudino, "Scaling Laws for Unamplified Coherent Transmission in Next-Generation Short-Reach and Access Networks," *Journal of Lightwave Technology*, vol. 39, no. 18, pp. 5805–5814, Sep. 2021.

[59] M. S. Erkilinc, D. Lavery, K. Shi, B. C. Thomsen, R. I. Killey, S. J. Savory, and P. Bayvel, "Comparison of Low Complexity Coherent Receivers for UDWDM-PONs (λ-to-the-User)," *Journal of Lightwave Technology*, vol. 36, no. 16, pp. 3453–3464, Aug. 2018.

[60] A. Mecozzi, C. Antonelli, and M. Shtaif, "Kramers–Kronig coherent receiver," *Optica*, vol. 3, no. 11, p. 1220, Nov. 2016.

[61] J. K. Perin, A. Shastri, and J. M. Kahn, "Design of Low-Power DSP-Free Coherent Receivers for Data Center Links," *Journal of Lightwave Technology*, vol. 35, no. 21, pp. 4650–4662, Nov. 2017.

[62] N. Vokic, D. Milovancev, F. Karinou, and B. Schrenk, "Coherent EML+TIA Detector for DSP-Free 1 Gb/s/λ Reception Over Extended Budget," *Journal of Lightwave Technology*, vol. 40, no. 14, pp. 4635–4641, Jul. 2022.

[63] J. A. Altabas, O. Gallardo, G. S. Valdecasa, M. Squartecchia, T. K. Johansen, and J. B. Jensen, "DSP-Free Real-Time 25 GBPS Quasicoherent Receiver With Electrical SSB Filtering for C-Band Links up to 40 km SSMF," *Journal of Lightwave Technology*, vol. 38, no. 7, pp. 1785–1788, Apr. 2020.

[64] M. S. Erkilinc, D. Lavery, R. Maher, M. Paskov, B. C. Thomsen, P. Bayvel, R. I. Killey, and S. J. Savory, "Polarization-insensitive single balanced photodiode coherent receiver for passive optical networks," in *2015 European Conference on Optical Communication (ECOC)*. Valencia, Spain: IEEE, Sep. 2015, pp. 1–3.

[65] M. S. Faruk, H. Louchet, M. S. Erkılınç, and S. J. Savory, "DSP algorithms for recovering single-carrier Alamouti coded signals for PON applications," *Optics Express*, vol. 24, no. 21, p. 24083, Oct. 2016.

[66] M. S. Faruk, D. J. Ives, and S. J. Savory, "Technology Requirements for an Alamouti-Coded 100 Gb/s Digital Coherent Receiver Using 3 × 3 Couplers for Passive Optical Networks," *IEEE Photonics Journal*, vol. 10, no. 1, pp. 1–13, Feb. 2018.

[67] L. Wang, Y. Zeng, X. Wang, T. Jiang, Y. Xiang, H. He, Z. Hu, H. Jiang, and M. Tang, "Bi-Directional Self-Homodyne Transmission With MIMO-Free DSP for Next-Generation Data Center Interconnects," *Journal of Lightwave Technology*, vol. 40, no. 18, pp. 6179–6189, Sep. 2022.

[68] J. Zhang, S. Xing, G. Li, and N. Chi, "High-performance and robust burst reception in coherent pon," in *2023 Optical Fiber Communications Conference and Exhibition (OFC)*, 2023, pp. 1–3.

[69] K. Christodoulopoulos, S. Bidkar, T. Pfeiffer, and R. Bonk, "Deterministically scheduled pon for industrial applications," in *2023 Optical Fiber Communications Conference and Exhibition (OFC)*, 2023, pp. 1–3.

[70] J.-i. Kani, S. Kaneko, K. Hara, and T. Yoshida, "Optical access network evolution for future super-broadband services and 6g mobile networks," in *2021 European Conference on Optical Communication (ECOC)*, 2021, pp. 1–4.

[71] T. Tanimura, S. Oda, T. Tanaka, T. Hoshida, Z. Tao, and J. C. Rasmussen, "A simple digital skew compensator for coherent receiver," in *2009 35th European Conference on Optical Communication*, Sep. 2009, pp. 1–2.

[72] H. Nagpal, G. Jullien, and W. Miller, "Memory architecture of a video-rate image convolver," in *ICASSP '82. IEEE International Conference on Acoustics, Speech, and Signal Processing*, vol. 7, May 1982, pp. 1203–1206.

[73] T. Wong and C. Kwong, "Adaptive filtering using Hartley transform and overlap-save method," *IEEE Transactions on Signal Processing*, vol. 39, no. 7, pp. 1708–1711, Jul. 1991.

[74] J. G. Kuk, S. Y. Kim, and N. I. Cho, "An overlap save algorithm for block convolution with reduced complexity," in *2009 IEEE International Conference on Acoustics, Speech and Signal Processing*, Apr. 2009, pp. 605–608.

[75] J. W. Leis, *Digital Signal Processing Using MATLAB for Students and Researchers: Leis/Signal Processing.* Hoboken, NJ, USA: John Wiley & Sons, Inc., Jun. 2011.

[76] S. J. Savory, "Digital filters for coherent optical receivers," *Optics Express*, vol. 16, no. 2, p. 804, 2008.

[77] R. Harris, D. Chabries, and F. Bishop, "A variable step (VS) adaptive filter algorithm," *IEEE Transactions on Acoustics, Speech, and Signal Processing*, vol. 34, no. 2, pp. 309–316, Apr. 1986.

[78] A. J. Viterbi and A. M. Viterbi, "Nonlinear estimation of PSK-modulated carrier phase with application to burst digital transmission," vol. 29, no. 4, pp. 543–551. [Online]. Available: https://ieeexplore.ieee.org/document/1056713

[79] M. Selmi, C. Gosset, M. Noelle, P. Ciblat, and Y. Jaouen, "Block-Wise Digital Signal Processing for PolMux QAM/PSK Optical Coherent Systems," *Journal of Lightwave Technology*, vol. 29, no. 20, pp. 3070–3082, Oct. 2011.

[80] M. G. Taylor, "Phase Estimation Methods for Optical Coherent Detection Using Digital Signal Processing," *Journal of Lightwave Technology*, vol. 27, no. 7, pp. 901–914, Apr. 2009.

[81] T. Pfau, S. Hoffmann, and R. Noe, "Hardware-Efficient Coherent Digital Receiver Concept With Feedforward Carrier Recovery for M-QAM Constellations," *Journal of Lightwave Technology*, vol. 27, no. 8, pp. 989–999, Apr. 2009.

[82] T. Pfau and R. Noé, "Phase-Noise-Tolerant Two-Stage Carrier Recovery Concept for Higher Order QAM Formats," *IEEE Journal of Selected Topics in Quantum Electronics*, vol. 16, no. 5, pp. 1210–1216, Sep. 2010.

[83] D. Godard, "Self-Recovering Equalization and Carrier Tracking in Two-Dimensional Data Communication Systems," *IEEE Transactions on Communications*, vol. 28, no. 11, pp. 1867–1875, Nov. 1980.

[84] E. Pincemin, N. Brochier, M. Selmi, O. Z. Chahabi, P. Ciblat, and Y. Jaouën, "Novel Blind Equalizer for Coherent DP-BPSK Transmission Systems: Theory and Experiment," *IEEE Photonics Technology Letters*, vol. 25, no. 18, pp. 1835–1838, Sep. 2013.

[85] D. Lavery, R. Maher, D. S. Millar, B. C. Thomsen, P. Bayvel, and S. J. Savory, "Digital Coherent Receivers for Long-Reach Optical Access Networks," *Journal of Lightwave Technology*, vol. 31, no. 4, pp. 609–620, Feb. 2013.

[86] S. S. Haykin, *Adaptive Filter Theory*, fifth edition ed. Upper Saddle River, New Jersey: Pearson, 2014.

[87] Kazuro Kikuchi, "Polarization-demultiplexing algorithm in the digital coherent receiver," in *2008 Digest of the IEEE/LEOS Summer Topical Meetings*. Acapulco, Mexico: IEEE, 2008, pp. 101–102.

[88] B. C. Thomsen, R. Maher, D. S. Millar, and S. J. Savory, "Burst Mode Receiver for 112 Gb/s DP-QPSK with parallel DSP," *Optics Express*, vol. 19, no. 26, p. B770, Dec. 2011.

[89] M. S. Faruk, Y. Mori, C. Zhang, and K. Kikuchi, "Proper polarization demultiplexing in coherent optical receiver using constant modulus algorithm with training mode," in *OECC 2010 Technical Digest*, Jul. 2010, pp. 768–769.

[90] J. Zhou, G. Zheng, and J. Wu, "Constant Modulus Algorithm With Reduced Probability of Singularity Enabled by PDL Mitigation," *Journal of Lightwave Technology*, vol. 35, no. 13, pp. 2685–2694, Jul. 2017.

[91] C. Xie and S. Chandrasekhar, "Two-Stage Constant Modulus Algorithm Equalizer for Singularity Free Operation and Optical Performance Monitoring in Optical Coherent Receiver," in *Optical Fiber Communication Conference*. San Diego, California: OSA, 2010, p. OMK3.

[92] C. Papadias and A. Paulraj, "A constant modulus algorithm for multiuser signal separation in presence of delay spread using antenna arrays," *IEEE Signal Processing Letters*, vol. 4, no. 6, pp. 178–181, Jun. 1997.

[93] A. Vgenis, C. S. Petrou, C. B. Papadias, I. Roudas, and L. Raptis, "Nonsingular Constant Modulus Equalizer for PDM-QPSK Coherent Optical Receivers," *IEEE Photonics Technology Letters*, vol. 22, no. 1, pp. 45–47, Jan. 2010.

[94] K. Kikuchi, "Performance analyses of polarization demultiplexing based on constant-modulus algorithm in digital coherent optical receivers," *Optics Express*, vol. 19, no. 10, p. 9868, May 2011.

[95] ——, "Fundamentals of Coherent Optical Fiber Communications," *Journal of Lightwave Technology*, vol. 34, no. 1, pp. 157–179, Jan. 2016.

[96] J. Zhang and Z. Jia, "Coherent Passive Optical Networks for 100G/λ-and-Beyond Fiber Access: Recent Progress and Outlook," *IEEE Network*, vol. 36, no. 2, pp. 116–123, Mar. 2022.

[97] V. Houtsma and D. van Veen, "High Speed Optical Access Networks For This Decade And The Next (Invited)," in *2022 IEEE Photonics Conference (IPC)*, Nov. 2022, pp. 1–2.

[98] Ye Li and Z. Ding, "Global convergence of fractionally spaced Godard (CMA) adaptive equalizers," *IEEE Transactions on Signal Processing*, vol. 44, no. 4, pp. 818–826, Apr. 1996.

[99] J. Xu, Y. Li, X. Hong, J. Qiu, Y. Zuo, H. Guo, and J. Wu, "The performances of singularity-avoidance CMA equalizers in real-time system," *Optics Communications*, vol. 510, p. 127843, May 2022.

[100] J. Bohata, J. Jaros, S. Pisarik, S. Zvanovec, and M. Komanec, "Long-Term Polarization Mode Dispersion Evolution and Accelerated Aging in Old Optical Cables," *IEEE Photonics Technology Letters*, vol. 29, no. 6, pp. 519–522, Mar. 2017.

[101] D. L. Peterson, "Field measurements of state of polarization and PMD from a tier-1 carrier."

[102] D. Waddy, Ping Lu, Liang Chen, and Xiaoyi Bao, "Fast state of polarization changes in aerial fiber under different climatic conditions," *IEEE Photonics Technology Letters*, vol. 13, no. 9, pp. 1035–1037, Sep. 2001.

[103] P. A. Nwakamma, G. Froc, Y. Jaouën, and C. Ware, "Analysis of the Singularity Avoidance Capability of Constant Modulus Algorithms in Coherent Optical Fibre Communication Systems," in *2023 Asia Communications and Photonics Conference/2023 International Photonics and Optoelectronics Meetings (ACP/POEM)*, Nov. 2023, pp. 1–5.

[104] Effenberger, "New applications and technologies of optical access," in *Optical Fiber Communication Conference (OFC) 2024*. San Diego, California: Optica Publishing Group, 2024, p. Th1E.3.

[105] D. Peterson, P. Leo, and K. Rochford, "Field measurements of state of polarization and pmd from a tier-1 carrier," in *Optical Fiber Communication Conference, 2004. OFC 2004*, vol. 2, 2004, pp. 4 pp. vol.2–.

[106] P. A. Nwakamma, G. Froc, Y. Jaouën, and C. Ware, "Advanced adaptive constant modulus algorithms for singularity avoidance over wide polarization mode dispersion range in optical fibre access systems beyond 100 gbps," in *50th European Conference on Optical Communications (ECOC 2024)*, vol. 2024, 2024, p. W2A.53.

[107] P. Oezsuna, A. Arnould, N. Braig-Christophersen, E. Spoiden, R. Emmerich, R. S. Luis, B. J. Puttnam, K. Aikawa, C. Schmidt-Langhorst, C. Schubert, R. Freund, and G. Rademacher, "Experimental demonstration of a correlation-avoidance cma for blind space-division multiplexed mimo equalization," in *50th European Conference on Optical Communications (ECOC 2024)*, vol. 2024, 2024, p. W1C.2.

[108] E. Ip, A. P. T. Lau, D. J. F. Barros, and J. M. Kahn, "Coherent detection in optical fiber systems," 2008.

[109] K. Kikuchi, "Optical Homodyne Receiver Comprising Phase and Polarization Diversities with Digital Signal Processing."

[110] R. Noe, "Phase noise-tolerant synchronous QPSK/BPSK baseband-type intradyne receiver concept with feedforward carrier recovery," *Journal of Lightwave Technology*, vol. 23, no. 2, pp. 802–808, Feb. 2005.

[111] L. Pessoa, H. Salgado, and I. Darwazeh, "Performance Evaluation of Phase Estimation Algorithms in Equalized Coherent Optical Systems," *IEEE Photonics Technology Letters*, vol. 21, no. 17, pp. 1181–1183, Sep. 2009.

[112] T. Pfau, "Carrier Recovery Algorithms and Real-time DSP Implementation for Coherent Receivers," in *Optical Fiber Communication Conference*. San Francisco, California: OSA, 2014, p. W4K.1.

[113] E. Ip and J. M. Kahn, "Feedforward Carrier Recovery for Coherent Optical Communications," *Journal of Lightwave Technology*, vol. 25, no. 9, pp. 2675–2692, Sep. 2007.

[114] ——, "Addendum to "Feedforward Carrier Recovery for Coherent Optical Communications"," *Journal of Lightwave Technology*, vol. 27, no. 13, pp. 2552–2553, Jul. 2009.

[115] M. S. Faruk and S. J. Savory, "Digital Signal Processing for Coherent Transceivers Employing Multilevel Formats," *Journal of Lightwave Technology*, vol. 35, no. 5, pp. 1125–1141, Mar. 2017.

ECOLE
DOCTORALE

Titre : Égalisation adaptative efficace pour l'atténuation des PMD dans les réseaux d'accès optique de nouvelle génération

Mots clés : Réseau d'accès optique, dispersion modale de polarisation, égalisation adaptative, détection cohérente

Résumé : Alors que le monde entre dans la quatrième révolution industrielle, la demande de connectivité va continuer à augmenter. Pour les réseaux optiques, cette augmentation de la demande proviendra principalement du réseau d'accès optique (OAN) qui doit répondre à ces exigences de manière flexible et rentable. Les réseaux optiques passifs (PON) sont actuellement les OAN les plus largement déployés en raison de leur rentabilité grâce à une architecture de séparation passive et à l'utilisation de la technologie de détection directe à modulation d'intensité (IM-DD) qui nécessite une optique relativement peu coûteuse. Plusieurs évolutions du PON IM-DD ont été standardisées pour répondre aux exigences de capacité monocanal jusqu'à 10 Gigabits/seconde (Gbps ou G), 25G et récemment 50G-PON. Cependant, cette augmentation de capacité s'accompagne d'un compromis, sacrifiant le coût, de sorte que la détection cohérente (CohD), une technologie de réseau central DSP coûteuse, est envisagée pour le PON (CPON). L'extension du PON IM-DD pour prendre en charge des capacités monocanal de 100G et au-delà le rapproche en termes de coût du CohD, motivant la contre-stratégie de réduction du coût d'un CPON potentiel qui permettra facilement 100G et au-delà. Cependant, compte tenu de l'architecture PON asymétrique qui nécessite un fonctionnement en mode rafale, les opérations DSP dans le CPON doivent également être conscientes du mode rafale. Cela se traduit par une exigence stricte en matière de latence. Considérant également que la dégradation de la dispersion du mode de polarisation (PMD), dans l'OAN, peut être élevée et avoir un impact sur l'égalisation DSP, une analyse minutieuse des propriétés de convergence de l'égalisation DSP est nécessaire. Dans cette thèse, nous abordons le problème de la latence en nous concentrant sur l'égalisation adaptative. Tout d'abord, nous proposons un égaliseur adaptatif capable de surmonter les limitations induites par l'environnement PMD potentiellement à large portée de l'OAN. Ensuite, nous améliorons l'égaliseur proposé pour qu'il s'autoreconfigure en fonction du niveau PMD. Enfin, dans le cadre de la réduction globale de la complexité du DSP, nous étudions le potentiel de l'algorithme proposé pour atténuer la dispersion chromatique (CD), réduisant ainsi le besoin d'un bloc DSP d'égalisation CD séparé.

Title : Efficient adaptive equalization for PMD mitigation in next-generation optical access networks

Keywords : Optical access network, polarization mode dispersion, adaptive equalization, coherent detection

Abstract : As the world transitions fully into the fourth industrial revolution, the demand for connectivity will continue to increase. For optical networks, this increase in demand will originate mostly from the optical access network (OAN) which must accommodate these demands in a flexible and cost-effective way. Passive optical networks (PONs) are currently the most deployed OAN because of their cost-effectiveness thanks to the passive splitting architecture and use of intensity modulation and direct detection (IM-DD) technology that requires relatively cheap optics. Several evolutions of the IM-DD PON have been standardized to meet single channel capacity requirements of up to 10 Gigabits/second (Gbps or G)-, 25G-, and recently 50G-PON. However, this increase in capacity comes with a tradeoff, sacrificing cost, such that coherent detection (CohD), a costly DSP-enabled core-network technology, is being considered for PON (CPON). Scaling up IM-DD PON to support single channel capacities of 100G and beyond brings it closer in cost to CohD, motivating the counter strategy of scaling down the cost of a potential CPON that will easily permit 100G and beyond. However, considering the asymmetric architecture of PON which requires burst-mode operation, the DSP operations in CPON must also be burst-mode compatible. This translates to a strict requirement on the latency. Considering also that the polarization mode dispersion (PMD) impairment in the OAN can be high and that it impacts the DSP equalization, careful analysis of the convergence properties of equalization DSP is necessary. In this thesis, we address the issue of latency focusing on adaptive equalization. Firstly, we propose an adaptive equalizer that can overcome the limitations induced by the potentially wide-range PMD environment of the OAN. Secondly, we enhance the proposed equalizer to self-reconfigure depending on the PMD level. Finally, in the context of overall DSP complexity reduction, we investigate the potential of the proposed algorithm to mitigate chromatic dispersion (CD) thereby reducing the requirement on a separate CD equalization DSP block.

Institut Polytechnique de Paris
91120 Palaiseau, France